Fundamental studies of the structure-performance correlations and interfaces in hard carbon anodes for Na-ion batteries

Hande Alptekin
Department of Chemical Engineering, Imperial College London
2021

Submitted in partial fulfilment of the requirements for the degree of
Doctor of Philosophy of Imperial College London

DECLARATION OF ORIGINALITY

I hereby declare that this thesis and the work presented herein is my own work except where appropriately referenced or acknowledged.

Hande Alptekin

COPYRIGHT DECLARATION

The copyright of this thesis rests with the author and is made available under a Creative Commons Attribution Non-Commercial No Derivatives license. Researchers are free to copy, distribute or transmit the thesis on the condition that they attribute it, that they do not use it for commercial purposes and that they do not alter, transform or build upon it. For any reuse or redistribution, researchers must make clear to others the licence terms of this work.

Details of publications:

- Hande Alptekin, Heather Au, Anders Jensen, Emilia Olsson, Mustafa Goktas, Thomas F Headen, Philipp Adelhelm, Qiong Cai, Alan J Drew, and Maria Magdalena Titirici. Sodium storage mechanism investigations through structural changes in hard carbons. *ACS Applied Energy Materials*, 2020.
- Heather Au, Hande Alptekin, Anders CS Jensen, Emilia Olsson, Christopher A. O'Keefe, Thomas Smith, Maria Crespo-Ribadeneyra, Thomas F. Headen, Clare P. Grey, Qiong, Alan J. Drew and Maria-Magdalena Titirici. A revised mechanistic model for sodium insertion in hard carbons. *Energy & Environmental Science*, 2020.
- Anders C. S. Jensen, Emilia Olsson, Heather Au, Hande Alptekin, Zhengqiang Yang, Stephen Cottrell, Koji Yokoyama, Qiong Cai, ORCID Maria-Magdalena Titirici and Alan J. Drew. Local mobility in electrochemically inactive sodium in hard carbon anodes after the first cycle. *Journal of Materials Chemistry A*, 2020.
- Joshua M. Bray, Claire L. Doswell, Galina E. Pavlovskaya, Lin Chen, Brij Kishore, Heather Au, Hande Alptekin, Emma Kendrick, Maria-Magdalena Titirici, Thomas Meersmann and Melanie M. Britton. Operando visualisation of battery chemistry in a sodium-ion battery by 23 Na magnetic resonance imaging. *Nature communications*, 2020.
- Emilia Olsson, Jonathon Cottom, Heather Au, Zhenyu Guo, Anders C. S. Jensen, Hande Alptekin, Alan J. Drew, Maria-Magdalena Titirici and Qiong Cai. Elucidating the effect of planar graphitic layers and cylindrical pores on the storage and diffusion of Li, Na, and K in carbon materials. *Advanced Functional Materials*, 2020.

Awards:

- STFC Futures Early Career Award 2019
- Poster prize by the Royal Society of Chemistry at the Carbon for Energy Storage and Environment Protection Conference

ACKNOWLEDGEMENT

I decided to pursue a PhD in a foreign country because I have always wanted to experience higher education in another country and experience and use more modern technologies in my field. Looking back at those thoughts from where I am now, I realize how small I was thinking at that time. In fact, doing a PhD abroad is not just an academic achievement, it has been a life changing experience that has taught me to maintain a strong stance in the hardest of times, embrace the complexity, understand a variety of cultural backgrounds and most importantly it has shown me that we are all different yet we are all same.

Doing a PhD was definitely something completely different to what I have experienced during my master's degree in Turkey. The differences in language, history, school system, standards, and aspirations have made the transition from Turkey to the UK difficult. This is intensified by the self-doubt and anxiety that comes with studying abroad. It took me months to find my own way in order to fit in. Cultural and scientific challenges developed me as an individual and as a scientist. During this time, the support I got from other PhD fellows, scholars, faculty staff, and friends and family was invaluable. I am grateful to the many people who supported me throughout my Ph.D. journey.

Firstly, I would like to thank my supervisor Prof. Magda Titirici for the immeasurable amount of support, patience and guidance. She has been a great role model, and the most wonderful supervisor I could have ever asked for. I feel privileged to have had the opportunity to work with her, be trained by her and to have spent time together for more than four years. I have learnt so many things from her strong but compassionate leadership, her own unique way of managing things and people, inclusively, unpretentiously that I will remember all my life. I am particularly grateful for her encouragement and patience when I was going through some difficult times.

A big thank you must also go out to all the individuals who have helped and assisted me in the collection of results and samples analyses due to my limited access to the particular characterization techniques. Thank you to Dr. Anders Jensen for conducting total neutron scattering and SAXS/WAXS measurements of the materials I worked with, and for his help in interpreting these results. Thanks to Dr. Emilia Olsson who helped me greatly with the computational aspect of this work and providing full support on my papers. Thank you to Dr. Mustafa Goktas for helping with in-situ Electrochemical Dilatometry. Thanks to Dr. Gwilherm

Kerherve for always assisting with XPS calculations and never complaining about the large number of samples. Thank you to Dr. Mahmoud Ardakani and Dr. Cati Ware for their constant help and advice during SEM and TEM sessions.

I would also like to extend my thanks to Heather and Maria for their valuable scientific discussions, for correcting parts of this work, for backing and supporting me in my research, for their true friendship, as well as for fostering a relaxed and trusting atmosphere. I am particularly grateful now for having such amazing neighbors like them. Thank you to all my other colleagues and friends from the Titirici group, both old and new, it has been a privilege to work with them. Thank you to Philipp, Servann, Jingyu and Hui for sharing this learning and growing journey with me for the last four years. Thanks to Fei, Zhen, and Zhenyu for always being willing to share their knowledge and review our findings. I am grateful to have had the opportunity to work in a group that value the importance of diversity and inclusion. It has been an environment where we have all felt included and respected regardless of any 'differences' we may have.

Also, many of my Turkish friends have played an important role in helping me get through this process. Thanks to Ayse Kaya for always being there for me, no matter the distance or time difference between us, and for believing in me before I believed in myself. Thank you to Hale Ozturk for always looking after me, having Sundays walks around Victoria park with a fine warm cup of coffee has made this time a little less stressful. Many thanks to Gozde Cay for preparing delicious hot chocolates at the most necessary times. Thanks to Aysegul Chouseinoglou and her family for their kindness and compassion. Thank you to Ibrahim Umit Akgun for his endless support and encouragement and giving me strength. Thank you very much also to Zehra Sahin, a good friend and a wonderful perfon, I wouldn't have come here without her help. Similarly, to Emine Azakan who made London feel like a second home, she was like a mom abroad with all her love and unconditional hospitality.

Last but definitely not least; I would like to share my deep and sincere gratitude to Annem and Babam for their continuous and unconditional love, help, support and open-mindedness. Thanks to them, I've always encountered beautiful things throughout my life and I really owe everything to my parents. I am also grateful to my brother Ibrahim for always being there for me, his endless strength to follow his dreams has inspired me and taught me to never give up.

ABSTRACT

Na-ion batteries (NIBs) have recently attracted extensive attention from the scientific community, as a cost effective and environmentally friendly alternative to Li-ion batteries (LIBs). Meanwhile, they also share the same working principle with LIBs, which makes the manufacturing of NIBs easy to scale-up to large volumes using the well-established LIBs production knowledge. However, the remaining challenges for NIBs commercialization are the lack of suitable materials for the negative electrode and a realistic focus on exploring electrolytes that bring these NIBs to market. Unfortunately, graphite, which is the most commonly used anode material in LIBs, shows poor electrochemical performance in NIBs. Hard carbon (non-graphizatible carbon), due to its relatively low cost and good electrochemical performance, is the most promising anode material for NIBs. Due to the structural complexity of hard carbons, understanding the correlation between carbon structure and the Na-ion storage mechanism is still a challenge to be overcome for commercialization of hard carbons as anodes in NIBs. There have been reports regarding the Na-ion storage mechanism in hard carbon anodes in NIBs, however discrepancies still exist.

Herein, this thesis addresses two main topics. The first focuses on understanding the structure-performance correlations of Na-ion in hard carbons and improving the performance of hard carbon anodes. For this purpose, a series of hard carbons with tuned structure was synthesized by changing the carbonization temperature to vary systematically the porosity, number of defects, and graphitic structure. The microstructure of hard carbon and sodium storage behavior was demonstrated with X-ray and neutron scattering, Raman spectroscopy, transmission electron microscopy (TEM) and corroborated with density functional theory (DFT) calculations. Additionally, *in-situ* electrochemical dilatometry was also used to examine electrode expansion during cycling; to our knowledge, this is the first time that this procedure has been extended to sodium ion storage system investigations in hard carbons. Combined experimental studies and theoretical calculations reveal that it is the Na-ion storage at defect sites and intercalation in expanded graphene layers that corresponds to the slope capacity, while pore filling is responsible for the low voltage plateau region. It shows that hierarchically structured porous materials with partially large closed (internal) pores could act as active site for electrochemical storage and lead to reversible redox capacity. Therefore, in this thesis, a simple pore forming technique known as soft templating method is applied to synthesize mesoporous carbon with large closed pores to investigate the effect of closed mesopores and the results are compared with the microporous hard carbons. Here, the electrochemical these

findings are of interest to the battery community, as they are important for the design of future electrode materials with high capacity and therefore building better batteries.

In order to develop high performance anode electrodes, a more integrated and holistic approach to the cell components is required. It should be noted that the performance of anode materials is influenced by the application of electrolytes and counter electrode; therefore, all components need to be investigated simultaneously. It is of crucial importance to understand and eventually control electrode interface and electrolyte chemistry, because the choice of electrolyte and the chemistry of the electrode interface has an important role on the energy density, cycle life, storage performance and reversible capacity of active materials. The second focus topic of this thesis is to study the surface chemistry of the anode electrode and electrolyte interface, which is another key consideration for the development of anode materials. The most commonly used Na salts, namely $NaClO_4$ and $NaPF_6$, were compared in EC: DMC and diglyme solvents. The vital role of the salt anion in the process of electrolyte decomposition at the sodium metal were further demonstrated. Comparison of half-cell configuration with sodium metal and full cell with NVPF/C cathode showed that employing metallic sodium anodes has critical consequences for the long-term cycling performance of batteries.

TABLE OF CONTENTS

1 Introduction 15

1.1 Motivation 15

1.1.1 Why do we need energy storage technologies? 15

1.1.2 Critical roles of batteries to tackle climate change 21

1.1.3 Aims and Objectives of this thesis 25

2 Literature Overview 26

2.1 Lithium-ion Batteries 26

2.2 Concerns and alternative technologies for LIBs 28

2.3 Sodium-ion Batteries: Rising Again from the Ashes 30

2.4 Cost comparisons 33

2.5 Technical Information about Batteries 35

2.5.1 Theoretical Specific Capacity, Specific Energy and Specific Power 35

2.5.2 Charge and discharge 35

2.5.3 The gravimetric energy density 35

2.5.4 The rate capability (C rate performance) 36

2.5.5 Initial Coulombic efficiency 36

2.6 Hard carbon anode materials for NIBs 37

2.7 Mechanism of Na-ion storage in hard carbon 42

2.8 Cathode materials for NIBs 46

2.9 Electrolyte/Electrode Interfaces 48

2.9.1 Electrolytes for NIBs 48

2.10 Solid Electrolyte Interphase (SEI) 53

2.11 Hydrothermal carbonization (HTC) for anode materials 56

3 Experimental 57

3.1 Characterization Methods of Hard Carbon 57

3.1.1 Methods for structural characterization 57

3.1.2 Methods for electrochemical characterization 65

3.2 Electrode materials and electrolytes 66

3.2.1 Glucose-Citric acid temperature series 66

3.2.2 Soft Templated carbons 67

3.2.3 $Na_3V_2(PO_4)_2F_3$ /C cathode 67

3.3 Structural and Physical Characterization Method 68

3.4 Electrode Preparation and Cell Assembly 69

3.4.1 Electrode Preparation 69

3.4.2 Cell Assembly 69

3.5 Electrochemical Measurements 70

3.6 Computational Methods 71

4 Investigation of Sodium-ion Storage Mechanism In Hard Carbon Electrode 73
4.1 Introductions ... 73
4.2 Results and Discussion ... 74
4.2.1 Structural characterisations 74
4.2.2 Electrochemical Characterisations 80
4.2.3 *In-situ* Electrochemical Dilatometry 83
4.2.4 *Ex-situ* SEM images 85
4.2.5 Computation calculations 86
4.3 Conclusions ... 89
5 Tuning the Closed Pore Structure of Hard Carbons for na-ion batteries 90
5.1 Introduction ... 90
5.2 Results and discussion ... 90
5.2.1 Hard carbons: texture evolution with temperature 90
5.2.2 Electrochemical performance as a function of hard carbon morphology 94
5.2.3 Performance Comparison of GC and ST hard carbon anode electrodes 96
5.3 Conclusions ... 99
6 Electrode-Electrolyte Interface And Sei Formation: Salt And Solvent Effects 101
6.1 Introduction ... 101
6.2 Results and discussion ... 102
6.2.1 Properties of bulk electrolytes 102
6.2.2 Electrochemical performance 105
6.2.3 SEI as a function of electrolyte 107
6.2.4 Half/Full cell comparison 112
6.3 Conclusions ... 114
7 Conclusions & Future Work 116
8 REFERENCES 119
Appendix I 134
Appendix II 139

LIST OF FIGURES

Figure 1.1 a) Share of global primary energy consumption in exajoules (qbtu =1.05505585 exajoules) b) Shares of global primary energy percentage[5] 15
Figure 1.2 Global Net Carbon Dioxide Emissions and projections by BP, US Energy Information Administration (EIA), Equinor, ExxonMobil, International Energy Agency (IEA), Institute for Energy Economics Japan (IEEJ), Organization of the Petroleum Exporting Countries (OPEC)[7] 16
Figure 1.3 Electricity generation and the drivers of CO_2 emissions[9] 17
Figure 1.4 The recommended sixth carbon budget in UK[12,14] IAS: international aviation and shipping 19
Figure 1.5 Emission abatement on the balance path provided by The Climate Change Committee[16] 20
Figure 1.6 Comparison of the costs for Li-ion batteries (LIB) and Na-ion batteries (NIB).[22] 22
Figure 1.7 Comparison of the a) gravimetric and volumetric energy densities [24] and earth crust abundance of metal anodes.[24] 23
Figure 1.8 (a) Schematic illustration of Na-ion battery and , Solid electrolyte interphase (SEI) formation 24
Figure 2.1Different Li-ion battery technologies' performance:(a) Lithium iron phosphate, (b) Lithium nickel manganese cobalt, and (c) Lithium nickel aluminium cobalt[47] 27
Figure 2.2Countries with the lithium reserves worldwide as of 2020[61] 29
Figure 2.3 a) NIB research growth as calculated by scientific publications (Source: Web of Science, Clarivate Analytics, Accessed Oct 9, 2019)[49] b) Typical discharge profiles for sodium/lithium insertion in half-cell of graphite and hard carbon. Discharge profiles redrawn from the digitalization of previously reported data.[69] 31
Figure 2.4 The cost of a cell per kWh of storage capacity is broken down into battery components and battery materials.[84] 34
Figure 2.5) a) Typical X-ray diffraction patterns (Cu K-alpha source) of hard carbon and graphite, b)) Franklin's representations of non-graphitizing and graphitizing carbons[102] 38
Figure 2.6 Illustration of the ion storage sites of hard carbon 39
Figure 2.7 An overview of the electrochemical performance of hard carbons at low rates (40 mA/g or less). 41

Figure 2.8 Representative schematics proposed for the sodium storage mechanism in hard carbon over years. 43
Figure 2.9 Schematic potential limits for the electrolyte stability, and the energy levels of HOMO and LUMO. 54
Figure 3.1. Classification of gas adsorption isotherms. (I) Microporous materials. (II) Non-porous materials with strong gas interactions (III) Non-porous materials with weak gas interactions (IV) Mesoporous materials. (V) Porous materials with weak interactions with the gas. (VI) Homogeneous surface materials.[206] 60
Figure 3.2 a) A typical SAXS instrument setup including monochromator (M), sample holder (S), and detector plane (D).[212] b) A typical SAXS pattern; intensity versus scattering vector curve in log-log scale 62
Figure 3.3 PDF patterns of pristine hard carbon with a) short and b)long distances 63
Figure 3.4 Basic setup of the Electrochemical Dilatometry[229], E-cell placed in the dilatometer frame *The glass frit is fixed in position, therefore only the thickness change in the working electrode is recorded. 65
Figure 3.5 Schematic representation of voltammogram 66
Figure 3.6 Scheme of coin cell assembly 70
Figure 4.1 SEM images of a) GC1000 b) GC1300 c) GC1500 d) GC1700 e) GC1900 and f) GC1300 electrode (with binder) 74
Figure 4.2 N_2 adsorption a) Isotherms b) Pore size distribution and CO_2 adsorption c) Isotherms d) Pore Size Distribution. 75
Figure 4.3. a) Structure factor (The Guinier-Porod region showing scattering of the nanopores (Q<1 Å-1) and scattering from the atomic structure at higher Q) and b) mean pore size determined from the Guinier-Porod region of the SANS and SAXS data c) interlayer spacing of the graphitic d) planes pair distribution functions (PDF) of the GCs with the PDF normalized to the height of the first peak at 1.5 Å e) size of the basal plane determined using the Scherrer method and the PDF, and f) peak height ratio of the first three peak observed in the PDF (Figure 4.3d) 76
Figure 4.4 TEM images of a) GC1000, b) GC1300, c) GC1500, d) GC1700, e) GC1900, and f) Raman spectra as a function of carbonization temperature. 77
Figure 4.5 a) Schematic of PDF data along a graphene sheet. b) Schematic of nearest neighbour positions in PDF data. 78

Figure 4.6 a) Wide survey XPS spectra and b) core level C1s and O1s spectra for the materials GCHTC (before carbonization) and after carbonization at each temperature 79
Figure 4.7 Cyclic Voltammetry a) GC1000 b) GC1300 c) GC1500 d) GC1700 and e) GC1900 and f) rate performance of the discharge capacities at current densities between 30 and 600 mA/g. 81
Figure 4.8 a) The galvanostatic sodiation (discharge) and desodiation (charge) potential profiles of GC1000, GC1300, GC1500, GC1700 and GC1900. b) Specific capacities of different samples at high voltage sloping region (0.1 – 1.0 V) and low voltage plateau region (around 0.1 V)..... 83
Figure 4.9 a) In-situ electrochemical dilatometry measurements of the electrode thickness change inthe first three cycles for GC1300 b) percentage thickness change of each electrodes during the second sodiation. 84
Figure 4.10 Ex-situ SEM pictures for GC1300 a) before cycling b) c) after first sodiation and d) at the end of first cycle. 85
Figure 4.11 Intercalation energy per sodium atom as a function of number of sodium (x) in Na_XC_{64} with different interlayer distance.. 3.75 corresponds to GC1000, 3.68 to GC1300, 3.66 to GC1500, 3.58 to GC1700, and 3.43 to GC1900. 87
Figure 4.12 Defective graphene models with a) no defect (pristine graphene), b) one oxygen substituted carbon site, with one carbon vacancy site (O_CV_C), c) two oxygen substituted carbon sites, with one carbon vacancy site ($2O_CV_C$), d) three oxygen substituted carbon sites ($3O_C$), e) two oxygen substituted carbon sites ($2O_C$) [240], and f) one oxygen substituted carbon site (O_C). Structures were visualized with VESTA.[262] 88
Figure 5.1 Formation of mesoporous structures via solid surfactant self-assembly and developing of carbon precursor over this surfactant self-assembly during HTC, followed by the complete removal of the template via high temperature pyrolysis. 91
Figure 5.2 SEM images of a) ST1000 b) ST1300 and c) ST1500, TEM images of d) ST1000 e) ST1300 and f) ST1500 showing the evolution of graphitic domains 91
Figure 5.3; a) basal plane size and thickness of basal plane stacks obtained from the 100 and 002 peaks, b) I_D/I_G ratio from Raman spectra and average interlayer spacing between the graphitic basal planes (d002) determined from the 002 peak, c) Pore size diameter of the micropores native to hard carbon and mesopores formed from the templating polymer, d) Relative pore volume changes obtained from gas adsorption and SAXS pattern. 92

Figure 5.4 a) N_2 adsorption/desorption isotherms at 77 K, b) pore size distributions of ST1000-ST1500 obtained from the NLDFT method.....93
Figure 5.5 a) Galvanostatic discharge-charge profiles showing the effect of different morphology on electrochemical performance, b) Cyclic voltammetry of the first cycle and second cycle.....95
Figure 5.6 Rate performance of the discharge capacities of ST1000, ST1300, ST1500 at current densities between 30 and 600 mA/g.....96
Figure 5.7 Comparison of structural properties.....98
Figure 5.8 Comparison of electrochemical performance in a) sloping region and b) plateau region and c) rate performance.....98
Figure 6.1 Illustration of AN and DN concept of Gutmann.....103
Figure 6.2 Raman spectra of CH_2 rocking/C−O stretching vibrations in a) EC:DMC b) Diglyme based electrolytes.....104
Figure 6.3 a)Galvanostatic charge/discharge profiles for ST1000-ST1500 in the first, second and 200th cycles, b) Cyclic Voltammetry of ST1500 in the first cyle c) second, third and fourth cycles cycle.....106
Figure 6.4 XPS survey spectra for samples: a) pristine ST1500 electrode; ST1500 electrodes cycled in b) EC:DMC- $NaPF_6$ and c) Diglyme- $NaPF_6$ and d) EC:DMC- $NaClO_4$.....108
Figure 6.5 C 1s spectra of a) pristine ST1500 electrode, cycled ST1500 electrode in a) $NaPF_6$ EC:DMC b) $NaPF_6$ Diglyme c)$NaClO_4$ EC:DMC, Atomic percentage of e-h) pristine sample, cycled sampled in different electrolyte with no etching (x=0), after 30 seconds of etching (x=30), after 60 seconds of etching (x=60).....109
Figure 6.6 O1s spectra of a) pristine ST1500 electrode, cycled ST1500 electrode in a) $NaPF_6$ EC:DMC b) $NaPF_6$ Diglyme c)$NaClO_4$ EC:DMC Atomic percentage of e-g) pristine sample, cycled sampled in different electrolyte with no etching (x=0), after 30 seconds of etching (x=30), after 60 seconds of etching (x=60).....110
Figure 6.7 a) Na 1s, b) F1s and Cl 2p spectra of pristine ST1500 electrode, cycled ST1500 electrode in different electrolyte (x=0), after 30 seconds of etching (x=30), after 60 seconds of etching (x=60).....111
Figure 6.8 Na metal in electrolytes a) $NaPF_6$ EC:DMC b) NaPF6 Diglyme c) NaClO4 EC:DMC right after Na addition, in d) $NaPF_6$ EC:DMC e) $NaClO_4$ Diglyme f) $NaClO_4$ EC:DMC after 4 days.....111

Figure 6.9 F1 s spectra of the surface of metallic sodium cathode aged a) in $NaPF_6$ EC:DMC b) in $NaPF_6$ Diglyme and c) Cl 2p spectra of ST1500 discharged electrode in $NaClO_4$ EC:DMC 112
Figure 6.10 a)Activation and pre-charging of NVPF/C material. Typical discharge/charge profile of a Na-ion half-cell using NVPF/C as cathode, Na metal as anode and 1 M NaClO4 in EC:DMC as electrolyte, b) Long-term cycling performance of full cell ST1500// NVPF/C (red line),half-cell ST1500 (blue line) and half-cell NVPF/C (black line) 113
Figure 6.11 The atomic fractions calculated from the XPS a-c) C1s spectra and d) O 1s spectra of the hard carbon anode cycled in 1M $NaClO_4$ EC:DMC.....114

1 INTRODUCTION

1.1 Motivation

1.1.1 Why do we need energy storage technologies?

The growth in population and improved standard of living have resulted in the number of people demanding access to affordable and reliable energy will drive energy demand in the decades to come.[1–3]The rise in energy use has also been linked to weather-related effects, with demand for cooling and heating increased due to greater global extremes in temperature. Global primary energy demand has grown rapidly over the past 25 years, reaching 583 quadrillion Btu (British thermal unit) in 2019, more than 200 qBtu higher than 1990 levels.[4] Looking at trends in the energy demand over the last 15 years (Figure 1.1a and b) oil has maintained its dominance in the energy mix (33.1%). Coal remains the second most common fuel, however it lost market share in 2019, accounting for just 27 % of total energy consumption. However, the encouraging news is that coal consumption is declining, with its share of the energy mix dropping to its lowest level since 2003. Meanwhile, renewables and natural gas grew in 2019. The share of both natural gas and renewables rose to 24.2% and 5.0% respectively. Renewables has now surpassed nuclear which constitute only 4.3% of the total energy mix. The energy share of hydroelectricity has been steady at around 6% for several years.[5]

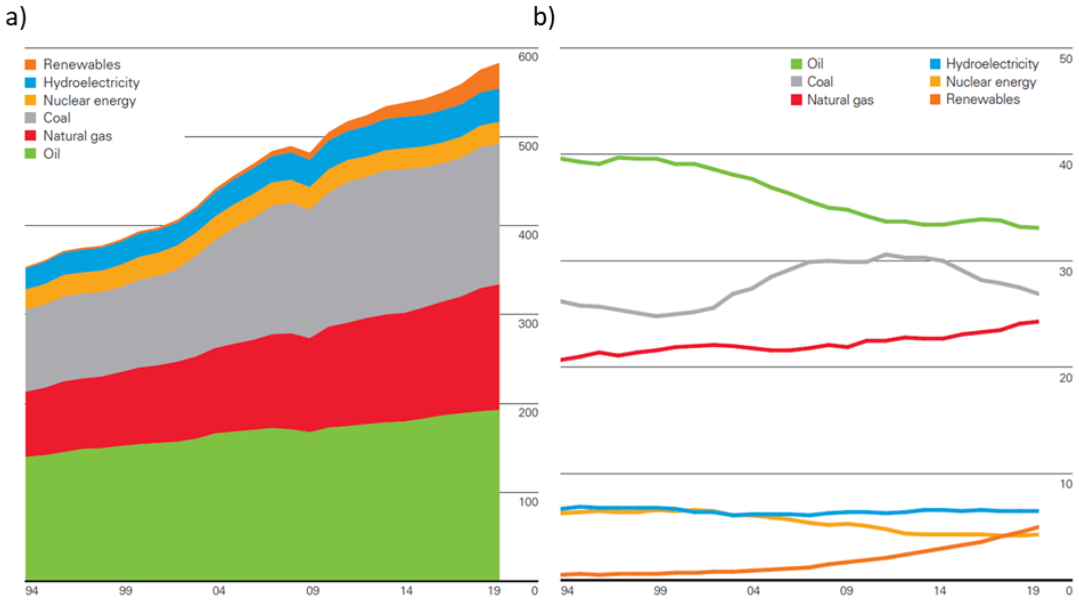


Figure 1.1 a) Share of global primary energy consumption in exajoules (qbtu =1.05505585 exajoules) b) Shares of global primary energy percentage[5]

By regional comparison of the energy consumption, China was leads to primary energy growth, being responsible for more than three quarters of the net global growth. India and Indonesia were the next largest contributors, while the US and Germany announced the largest declines in energy consumption in 2019. Final energy consumption released by The Department for Business, Energy and Industrial Strategy in the UK was 142.0 million tonnes of oil equivalent (mtoe) (142 mtoe = ~5.636 qbtu) in 2019 which was 1% per cent lower than that of in 2018.[6]

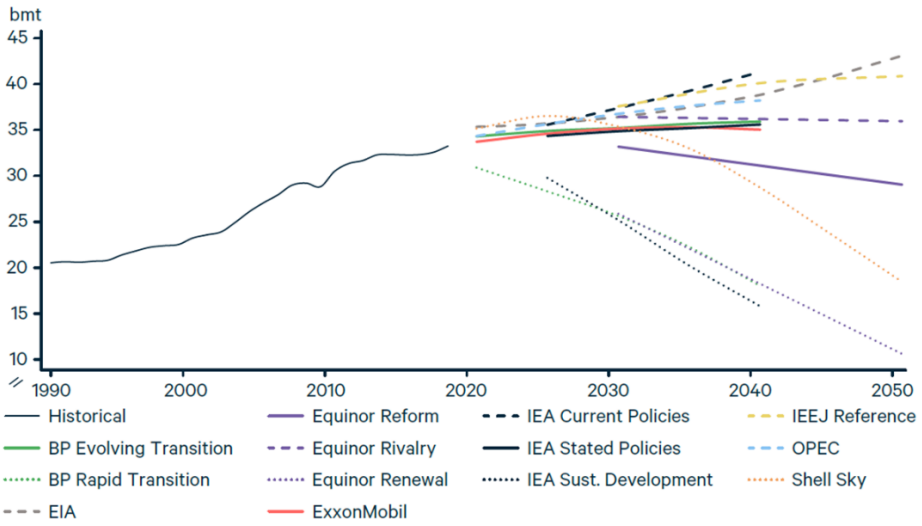


Figure 1.2 Global Net Carbon Dioxide Emissions and projections by BP, US Energy Information Administration (EIA), Equinor, ExxonMobil, International Energy Agency (IEA), Institute for Energy Economics Japan (IEEJ), Organization of the Petroleum Exporting Countries (OPEC)[7]

Human activity from deforestation to overpopulation increases the earth's temperature and changes the environment around us profoundly. A phenomenon called the greenhouse effect is the main cause. Gases in the atmosphere such as water vapour, carbon dioxide (CO2), methane, nitrous oxide, and chlorofluorocarbons in the atmosphere allow the sun's light in while preventing any of the heat from escaping, similar to the glass walls of a greenhouse. The more greenhouse gases (GHG) in the atmosphere the more heat gets trapped and strengthening the greenhouse effect and eventually increasing the earth`s temperature. Human activities like the burning of fossil fuels have increased the amount of CO_2 in the atmosphere by more than a third since the industrial revolution. Global energy related CO_2 emissions including energy use in industry, agriculture, buildings and transport reached a historical high of 33 billion metric tons (bmt) of CO_2 in 2018 due to the growth in population and economic activity (Figure 1.2).[8] It can be seen in Figure 1.3 that electricity generation is largely dependent on the coal, and the share of renewable energy in this sharing has increased over the years. The power sector emitted 13.8 $GtCO_2$ (a gigaton is equivalent to a billion-metric ton) in 2018 accounting for 40 percent of global energy-related emissions. Coal depended power generation has the largest

share of emissions from energy, accounting for 10 $GtCO_2$ or 29% of energy-related CO_2 emissions in 2018. It also accounts for nearly 75% of power sector emissions.[9]

The dramatic rise in GHG levels in the atmosphere has resulted in an unprecedented rate of global warming. Although the earth's climate has fluctuated in the centuries, atmospheric CO_2 levels have not surpassed today's levels in thousands of years. Climate change has an effect on our oceans, weather, food supply, and health. Greenland and Antarctica's ice sheets are melting. Excess water stored in glaciers causes sea levels to rise and flows into the oceans, flooding coastal areas. Higher temperatures often cause weather to become more severe, resulting in not only more violent major storms, flooding, and heavy snowfall, but also longer and more frequent droughts. These changes in weather pose challenges for agriculture as well as for food security, which means that climate change will impact the physical health of people directly. The extreme heat traps and raises the volume of smog in urban areas because small particles of ozone rise exponentially at higher temperatures. Higher levels of smog can cause health issues such as asthma, heart disease, and lung cancer.

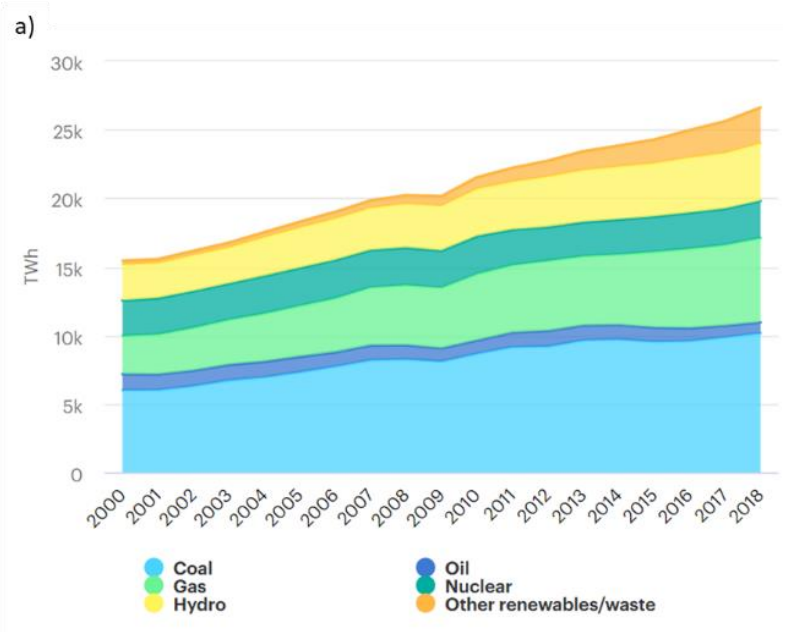


Figure 1.3 Electricity generation and the drivers of CO_2 emissions[9]

Nations globally approved the Paris agreement, the first-ever universal, legally binding global climate change agreement adopted by 196 Parties at the Paris climate conference in December 2015.[10] In the long-term, the Paris Agreement aims to reach a global decrease of green gas GHG emissions as soon as possible and to balance man-made (anthropogenic) emissions to the atmosphere and removals of GHGs from the atmosphere to limit global warming to well below 2°C and pursuing efforts to limit it to 1.5°C before 2100 because this would significantly reduce

risks and the impacts of climate change.[10] The Paris Agreement requires every 5- year cycle of increasingly ambitious climate action to be determined and implemented by all contributing countries. These plans for climate action are called nationally determined contributions (NDCs) and a new set will need to be presented at the upcoming COPS 2021 in Glasgow. In 2019, the UK became the first major economy to set a legally binding net zero emissions target with 'Further Ambition' scenario for reaching net-zero in 2050. The UK is committing to reduce economy-wide greenhouse gas emissions across different sectors by at least 68% by 2030, compared to 1990 levels in the provided NDC.[11] The Climate Change Act introduced carbon budgets to tackle climate change which is an Act approved by Parliament of the United Kingdom in 2008.[11] A carbon budget is a cap on the amount of greenhouse gases emitted in the UK over a five-year period which comprises various sectors such as energy (including transport); industrial processes and product use; agriculture; land-use, land-use change and forestry, and waste. Budgets should be made at least 12 years in advance in order to provide more time to policymakers, businesses and individuals. This five-year budgets reflect the realistic way to achieve the greenhouse gas emission mitigation goal of the United Kingdom in 2050.

Table 1.1 UK`s Carbon budgets and targets

Budget	Carbon budget level	Reduction below 1990 levels	Met?
1st carbon budget (2008 to 2012)	3,018 $MtCO_2e$	25%	Yes
2nd carbon budget (2013 to 2017)	2,782 $MtCO_2e$	31%	Yes
3rd carbon budget (2018 to 2022)	2,544 $MtCO_2e$	37% by 2020	On track
4th carbon budget (2023 to 2027)	1,950 $MtCO_2e$	51% by 2025	Off track
5th carbon budget (2028 to 2032)	1,725 $MtCO_2e$	57% by 2030	Off track
6th carbon budget (2033 to 2037)	965 $MtCO_2e$	78% by 2035	Should be legislated by June 2021.
Net Zero Target		At least 100% by 2050	

Based on the data published in the latest energy and efficiencies projections, [12] the UK met the first carbon budget (2008 to 2012), representing a 25% reduction below 1990 levels as

well as the second carbon budget (2013 to 2017), representing a 31% reduction below 1990 levels. The UK is projected to meet the third carbon budget (2018 to 2022), which corresponds to a 37% reduction below 1990 levels (Table 1.1 and Figure 1.4). In 2019, net territorial emissions in the UK were estimated to be 454.8 million tonnes carbon dioxide equivalent ($MtCO_2e$) and CO_2 made up around 80% of the 2019 total.[13] In December 2020, Climate Change Committee published an advice to Department for Business, Energy & Industrial Strategy UK on the sixth Carbon Budget with a new 'Balanced Pathway' scenario shown in, outlining the year-by-year pathway to require a reduction in UK emissions of 78% by 2035 relative to 1990. Unlike the previous budgets which have not included emissions from international aviation and shipping emissions, the sixth carbon budget does and allows a "headroom" for them by setting lower targets for other sectors.

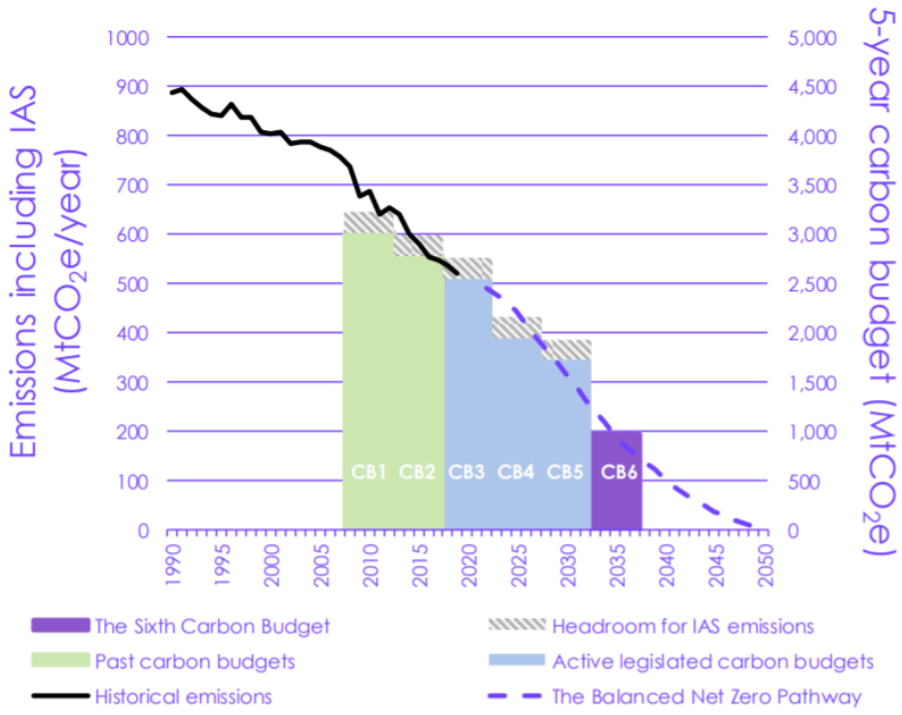


Figure 1.4 The recommended sixth carbon budget in UK[12,14] IAS: international aviation and shipping

In sixth carbon budget advice, the Climate Change Committee state that the existing approach is unsustainable and highlights the need for applying pressure across sectors for more ambitious climate change commitments. This is highly ambitious , placing UK decisively on the path to Net Zero by 2050. To achieve the net zero target, four main steps of emission abatements are advised by the Climate Change Committee as shown in Figure 1.5. The first section represented by purple line shows demand reduction and efficiency which is more important in the short term. This part requires people to be actively involved with low-carbon choices, about how

they travel, how they heat their homes, what they buy and what they eat. This means reducing demand for carbon intensive things like red meat or flights and it also means using efficient energy in our homes and building more efficient housing. The progress in emissions reduction in large part of the purple line rests on reducing our demand for high carbon goods over the next 5-10 year. Second section in Figure 1.5 represented by orange, red and yellow lines are about adopting low carbon technologies such as electric cars, heat pumps, solar photovoltaics and wind turbines. The orange line is electrification section that means adopting electrical devices and moving away from fossil fuels particularly in transport which can be seen that it is the most important part of the UK strategy overall. The UK electricity demand is predicted to increase from current 310 TWh in 2018 to 550-680 TWh by 2050, a huge challenge requiring renewable energy (125 GW wind, 85 GW solar on 1500 km^2 land by 2050), H_2 (10-20GW by 2050) and 70-80% storage capacity will be needed for the electricity generated by renewable sources among which 50GW to be provided by batteries.[15]

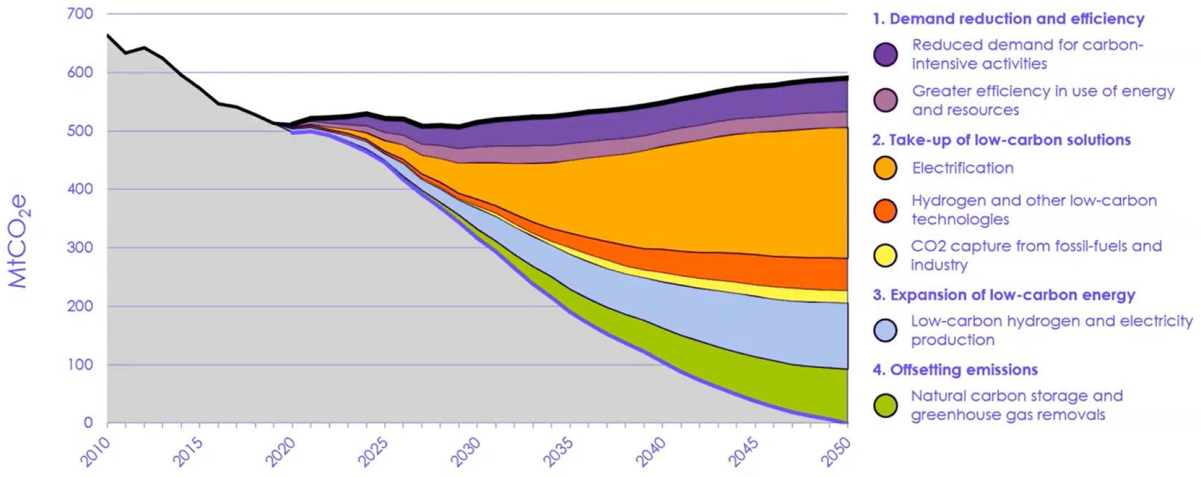


Figure 1.5 Emission abatement on the balance path provided by The Climate Change Committee[16]

Section 3 is the expansion of such low carbon technologies, removing further decarbonisation of the power sector and using low carbon fuels to run all these technologies in the red wages and completing the process fully decarbonised. The green stripe is about the natural stores of carbon that we have built overtime so that we can get rid of the emissions that are already in the atmosphere. It can be possible by planting trees planting new energy crops which we can use then in carbon capture storage and burying under the sea or even direct air capture and conversion back into fuels. Developing a net-zero emission world is possible when the anthropogenic emissions down to the level of removal of GHSs. Therefore, the energy system

must gradually move from fossil fuels towards renewable energy sources to reduce global anthropogenic CO_2 emissions.[17] Renewable and sustainable energy sources can meet the need for CO_2 reduction, but those energies mainly depend on seasonal or weather conditions and are not in a continuous supply. Solar power plants can be given as an example. While these power plants produce more energy during the day, the energy produced in the evening may not be sufficient to meet the instant increasing demand. For better electricity systems, it is a key point to even out the spikes and dips in energy production (spikes in sunny weather, dips in cloudy weather) and enable the energy generated to be used when there is time of peak demand. For this reason, developing additional stationary energy storage systems that enable significant utilisation of renewable resources is extremely important.[18,19]

1.1.2 Critical roles of batteries to tackle climate change

It is broadly recognized that there is an urgent need for action against climate change. Batteries are the key technology for sustainable development and climate change mitigation. They are already everywhere in our phones, laptops and electrical vehicles. However growth in the markets for electric vehicles and stationary electricity storage will make them particularly important to decarbonize road transportation and support the transition to a renewable power system therefore playing a critical role in achieving the Paris Agreement and keeping global emissions on track to stay below the 2°C. Affordable and flexible electricity storage technologies are set to accelerate transitions to clean energy around the world, as batteries can prevent 400 $MtCO_2$ emissions in transport sector and play an important role to enable renewables as a reliable source of energy, which will prevent 2200 $MtCO_2$ emissions together roughly 30% of required emission reductions in these sectors until 2030.[20] Today, the combined annual demand for batteries and other energy storage technologies stands at approximately 200 GWh with over three-quarters of these capacity additions dedicated to supplying electromobility applications . In 2013, almost 90% of all battery manufacturing supplied to consumer electronics. However, in 2017, electric vehicles became the largest consumers of batteries, and in 2019 share of electric vehicles had increased to two-thirds. As the level of implementation and the range of applicability of batteries and other storage technologies expands dramatically, it is expected that nearly 10 000 GWh of batteries and other storage will be required to meet demand across all sectors by 2040.[21]

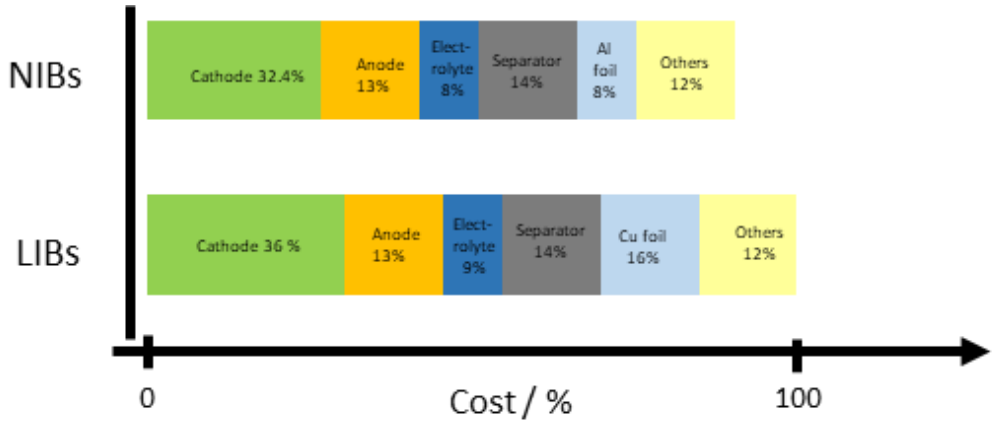


Figure 1.6 Comparison of the costs for Li-ion batteries (LIB) and Na-ion batteries (NIB).[22]

The 2019 Nobel Prize in chemistry has been awarded to John B. Goodenough, M. Stanley Whittingham and Akira Yoshino for their pioneering work in the development of lithium-ion batteries (LIBs). As one of the greatest inventions in history, LIBs have improved our lifestyles and helped power the lives of millions of people each day with small scale applications such as mobile phones, digital cameras, laptops to large scale sectors such as Electric Vehicles, and Energy Storage Systems.[23] Currently, all key technologies in the market rely on the application of the most advanced batteries available LIBs since there is no other technology or dominant design that can outperform current Li-ion technology across these areas. The limited geographical availability of raw materials like cobalt or lithium resources (such as Li_2CO_3) have led to continuously increasing prices and need to find an cheap and sustainable alternative to LIBs has become quite important to counterbalance the increased demand power sources in future energy storage applications.[22] It should be also considered that different battery applications have different performance criteria of for example, smartphones, power tools, electric cars and utility-scale stationary batteries have different requirements and tolerances for energy and power density, durability, material costs, sensitivity and stability. Grid-scale storage and energy access provision, neither of which require the levels of performance needed for electromobility.

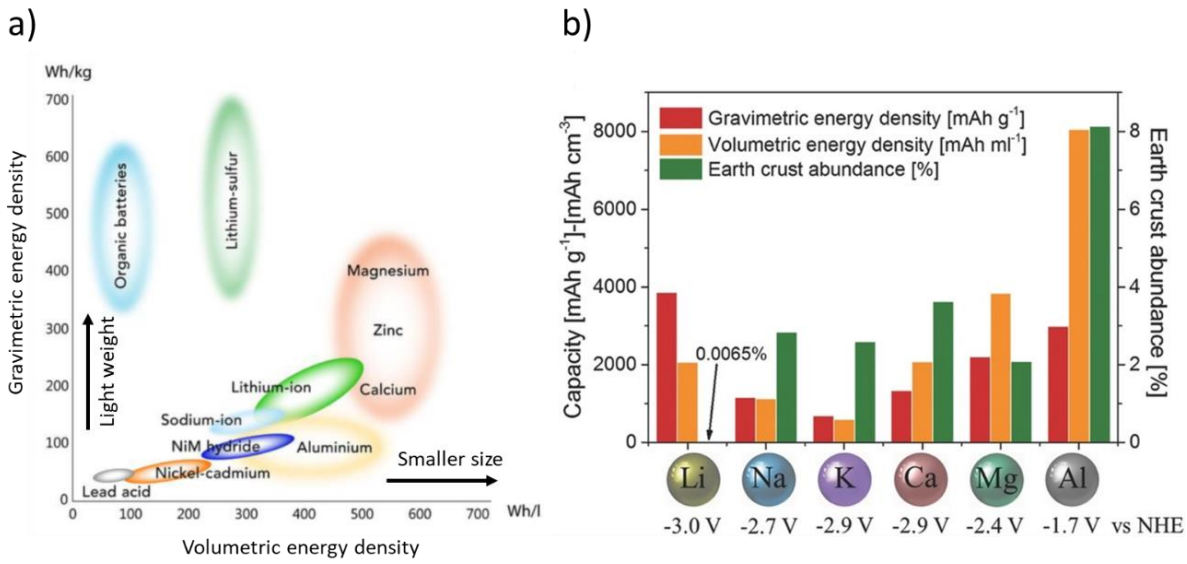


Figure 1.7 Comparison of the a) gravimetric and volumetric energy densities [24] and earth crust abundance of metal anodes.[25]

Alternative candidates with the potential to meet the high-performance battery technology requirements include sodium ion, sodium metal, magnesium, calcium, aluminium. metal–air, and metal–sulfur batteries which could represent an improvement compared with Li-ion in terms of cost, density and lifecycle, as well as further benefits owing to the more widely available materials found in these types of battery than those used in LIBs (Figure 1.7b). Sodium-ion batteries (NIBs) have received significant attention as a potential eco-friendly and lower cost alternative to LIBs, owing to the abundance (and thus cheapness) of sodium.[1,26] Lithium and sodium ion batteries are conceptually identical and operate under the same principle: alkali ions are shuttled back and forth in the electrolyte between the two host electrode materials, the cathode and anode. In term of cost comparison, by the replacement of expensive copper foils, used as the current collector for LIB anodes, with inexpensive aluminium since sodium (unlike lithium) does not alloy with aluminium at the anode 8% cost reduction can be achieved.[22] A slight cost reduction is also expected to be achieved by replacing Li salts with Na salts in the electrolyte.[27,28] Therefore, Na-ion batteries are estimated to cost about 10% less than commercial Li-ion batteries, assuming they are equivalent in energy density (Figure 1.6).[22] The power and rate capability of NIBs has been outstanding and, even in some cases, superior to LIBs, makes NIBs alternative chemistries for stationary energy storage applications in which low cost and life cycle is a crucial requirement.[29] However, the higher atomic mass (23 g mol^{-1} and 7 g mol^{-1} for sodium and lithium, respectively) and a higher redox potential (−2.71 V for sodium compared with −3.04 V for lithium, both versus the standard hydrogen electrode) of sodium compared to lithium leads to low-voltage batteries

resulting in the lower theoretical energy density for the NIBs (Figure 1.7a). This indicates that the cost reduction achieved by using NIBs may not be significant in terms of the cost per energy. In order to make a significant difference in cost per energy unit, it is important to develop electrode materials with high energy densities for NIBs.

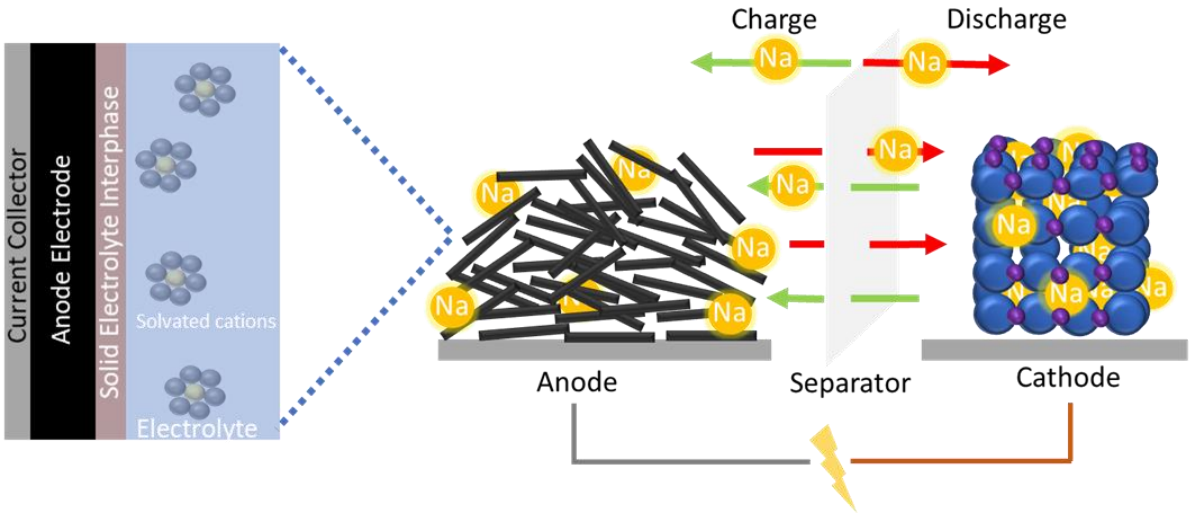


Figure 1.8 (a) Schematic illustration of Na-ion battery and , Solid electrolyte interphase (SEI) formation

Non-graphitizable carbons, hard carbons have been considered as the most promising anode materials for NIBs, because it has cheap and abundant precursors and can be produced easily.[30–32] Comprehension of the insertion mechanism of Na^+ ion into disordered hard carbon is crucial since it will be a guide to tailor structure of hard carbon accordingly and therefore to reach high energy densities. Even though there is an increasing interest in that material, the mechanistic understanding of Na-ion storage in complex structure like hard carbons and investigation of the structure-electrochemical performance correlation is still under debate.[33–37]Addition to hard carbon morphology, the solid electrolyte interphase (SEI), the interface formed on the negative electrode plays important role on coulombic efficiency on the first cycle and hence the practical energy density of the full cell (Figure 1.8).[38,39] SEI is a protective layer formed on the surface of anode upon electrolyte decomposition during the first charge/discharge process. The concept of SEI was first introduced by Peled.[40] According to Peled's study, the ideal interface formation is expected to have high ionic conductivity and absolute electric insulation, in order to provide rapid transport of the ions and isolate the unwanted side reactions caused by electrons, respectively. The physical and chemical properties of the interface can be affected by the solvation structure between the cation and solvent of the electrolyte, whilst anions have an important role in determining the thickness and ionic conductivity of the interface.[39] The SEI chemistry and development mechanism has

been extensively studied in Li-ion systems, but only a few findings have been published in the NIBs field. Although NIBs are similar to LIBs on the basis of the working principle, these systems have different characteristic behaviours at bulk, surface, and interface [41]Since the interaction of lithium ions with negatively charged species or lone pair electrons is stronger than that of sodium ions, the solubility of the electrolyte decomposition products differs, it would be misleading to use lithium systems as a guide to understand sodium systems. The formation of the SEI layer is much more different as well as difficult in NIBs because of the higher solubility of the decomposition products in Na^+ based electrolyte solution, as the deprivation of a protective layer cause corrosion (i.e., chemical oxidation) of the Na metal and sodium- inserted carbon. Systematic studies of chemical-physical properties of the electrolyte/electrode interface and understanding their effect on electrochemical performance, is fundamental to further design and development of the anode materials and therefore NIBs with high energy density.

1.1.3 Aims and Objectives of this thesis

The aim of this work is to contribute to understanding of how to design long cycle life and high energy density and high-power density NIBs. While NIBs are thought to be the most promising alternative to LIBs in terms of durability and cost, further research and development is needed, mainly in terms of electrochemical efficiency, particularly in terms of energy density. Because of their high storage capacity, low working potential, and cyclic stability in NIBs, hard carbon anode materials have gotten a lot of attention. The hard carbon electrode morphology is so crucial to the battery's electrochemical efficiency, designing methodologies to change the electrode structure and interface chemistry and link them to battery performance is also critical. Following research objectives would facilitate the achievement of this aim:

a) to study the correlation between hard carbon structure and electrochemical performance to enable an in-depth mechanistic understanding of Na-ion storage in hard carbon using *in-situ* electrochemical characterization methods.
b) to establish systematic research on the electrode interface interactions by investigating electrolyte decomposition products on the electrode surface with *ex-situ* methods and understanding the effect of the different electrolyte systems on the cell performance.

2 LITERATURE OVERVIEW

Batteries are electrochemical energy storage devices that are able to store electrical energy in a chemical form and convert that energy into electricity when needed. There are two fundamental types of chemical storage batteries; primary batteries which can only provide energy once, as the chemical reactions in the battery are irreversible, and secondary or rechargeable batteries that release energy by a reversible chemical reaction and can be recharged again and again. The first electrochemical battery called as the voltaic pile was invented by Alessandro Volta in 1799.[42] It consisted of alternating disks of zinc and copper separated by paper soaked in salt water. The Voltaic pile made it possible for other scientists to experiment with electric currents, for example English scientists William Nicholson and Anthony Carlisle were able to decompose water into hydrogen and oxygen using a voltaic pile, consequently discovering electrolysis and creating the field of electrochemistry.

The first rechargeable battery, the lead acid battery, was invented in 1859 by Gaston Planté.[43] Planté's configuration consists of two electrodes divided by a rubber strip: an anode of lead and a cathode of lead dioxide. The electrons lost by the anode through oxidation were conducted to the cathode by an electrolyte of sulfuric acid. An electrolyte was used to conduct the electrons released by the anode during oxidation to the cathode. Externally, electrons and their associated charge could be passed to a device such as a light bulb. However, the problem with the limited the life of the battery because the lead dioxide cathode had little active material available for the chemical reaction. This problem prompted scientists to seek alternative rechargeable battery solutions. In 1899, Waldemar Jungner developed Ni-Fe and Ni-Cd batteries in which KOH was used as an electrolyte.[44] Ni-Cd batteries had better high-rate and low-temperature performance than lead-acid batteries [45]and are still used today.

2.1 Lithium-ion Batteries

Lithium-ion technology is made up of a number of different chemistries, the primary reaction of which is the transport and intercalation of lithium ions into the cathode and anode, respectively. The chemical composition of the cathode, which is usually a lithium metal oxide, and the anode, which is typically graphite, determine the electrochemical properties of Li-ion batteries.[46] This technology has a high efficiency (over 90%), even some commercial products have a rated round trip efficiency of over 95% , a high energy density (90–190 Wh/kg)[47], and a long lifetime (up to 10000 cycles depending on the Li-ion chemistry). LIBs have been used in electronics, and in recent years despite the fact that it is still relatively expensive , they have

emerged as the primary power source for electric vehicles and grid-connected applications.[48,49] There are several Li-ion technologies available today, for example; NMC (lithiated nickel manganese cobalt oxide), NCA (lithiated nickel cobalt aluminium oxide), LCO (lithiated cobalt oxide), and LFP are some of the most popular cathode materials (lithiated iron phosphate). Among the above technologies considered, NMC-based technology provides the best results (Figure 2.1). Its excellent performance, among other reasons, has helped to develop NMC as the primary Li-ion technology for stationary storage and EVs.

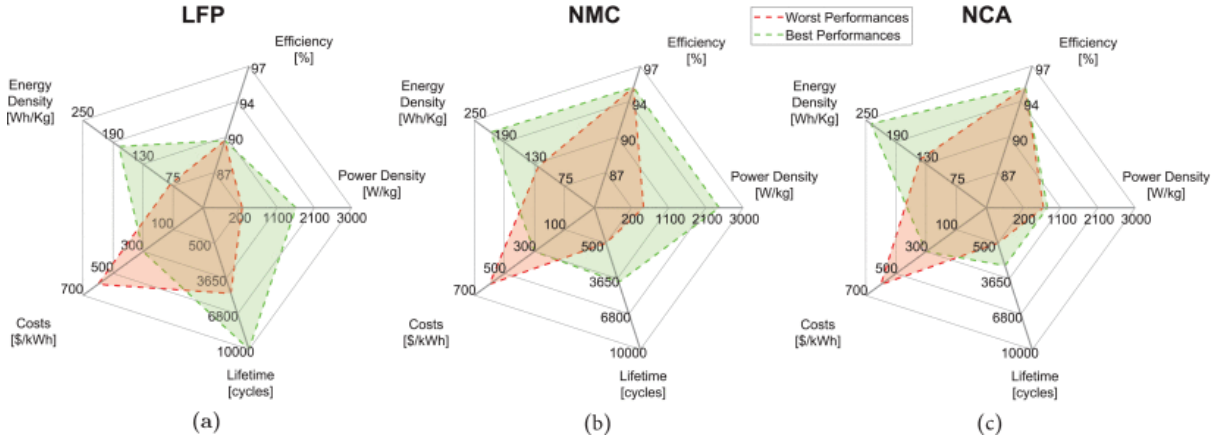


Figure 2.1Different Li-ion battery technologies' performance:(a) Lithium iron phosphate, (b) Lithium nickel manganese cobalt, and (c) Lithium nickel aluminium cobalt[48]

The lithium ion battery's history starts after the oil crises of the 1970s. The related price hikes and oil shortages in the United States sparked interest in renewable fuels and energy efficiency science. Whittingham suggested the concept of rechargeable lithium batteries while working for the oil firm Exxon in the 1970s, and developed a prototype using a lithium-metal anode and a titanium disulfide cathode which had molecular space for lithium ions.[50] The principle worked, but Whittingham's version of the battery was brittle and vulnerable to bursting after prolonged use. The discovery, made by researchers at Oxford University in the United Kingdom in the late 1970s, that lithium ions can be intercalated into the crystal lattice of trivalent cobalt or nickel oxides to give the compounds $LiCoO_2$ and $LiNiO_2$, respectively, gave rise to the lithium-ion battery. In an organic electrolyte, these oxide electrodes were used as positives against metallic lithium negatives, yielding a 4V cell.[51] In addition to the production of positive (cathode) electrode materials, research was also conducted on negative (anode) electrodes made of Li-metal and Li-alloy.[52–55] Such anodes were used in the first commercial batteries. However, the formation of anode dendrites raised safety concerns. After 1982, when Yazami and Touzain published their work in which Li was intercalated into graphite using a solid electrolyte of polyethylene oxide and $LiClO_4$, the negative electrode problem was

solved[56]. This discovery was followed by the Armand group, who discovered that it would be possible to use two intercalation electrodes - one positive and one negative - with lithium ions switching back and forth between the two electrodes. This battery contains no metallic lithium and is therefore much safer to recharge than the previous, lithium-metal cell configuration. Because of the transport of ions from one electrode to another during the charge–discharge process, this battery was called the rocking-chair battery (later the lithium-ion battery).[52] The rocking-chair battery concept was thus proposed the same year that Goodenough proposed the $LiCoO_2$ positive electrode, and with Yoshino's design pioneered the use of carbon-rich anode materials in the 1980s, significantly improved safety and allowed commercial production of the batteries. Commercialization was accomplished in 1991 when the Sony and Asahi Kasei teams led by Nishi commercialised the $LiCoO_2$/hard-carbon battery. Sony[57] and Sanyo[58] were the first to commercialise the rocking-chair design in the Japanese battery industry. For several decades, LIBs have been the most developed type of ionic batteries due to their high theoretical specific capacity and energy density and superior performance.[59] John B. Goodenough, M. Stanley Whittingham, and Akira Yoshino who have pioneering contribution to Li-ion batteries an innovation that has become ubiquitous in the wireless devices that pervade everyday life: phone, tablet, laptop, and probably even your car, were awarded the Nobel Prize in Chemistry in 2019. Because of their light weight and small scale, lithium-ion batteries are now being used to fuel homes, aircraft, and even the electric grid, which supplies power to whole cities. LIBs have recently made an appearance in the automotive industry. Because of their remarkable energy densities, LIBs improved the efficiency of EVs and increased performance significantly.

2.2 Concerns and alternative technologies for LIBs

Transportation and energy production are two industries that urgently need to minimise pollution, and advances in electric vehicles and stationary storage are rapidly transforming both markets. Lithium is an important component in energy storage, and demand has risen steeply in recent years. However, the world lithium´s reserves issue is limited[60] and the difficulty of extraction and unevenly distributed resources of the battery components put LIBs at a disadvantage.[61] As a result of ongoing exploration, known lithium supplies is now approximately 80 million tonnes. Lithium deposits in the United States total 6.8 million tonnes, derived from continental brines, geothermal brines, hectorite, oilfield brines, and pegmatites. [62] The lithium resources all around the world are listed in Figure 2.2. Lithium demand was 34.6 kt in 2015. This is distributed through EVs (14%), stationary energy storage systems

(around 1%), conventional battery markets (25%), and non-battery applications (60%). The significant increase in Li consumption to 49 kt in 2019 was attributed to a surge in demand for battery applications over the last few years, with Li consumption share reaching more than 60%.[62]

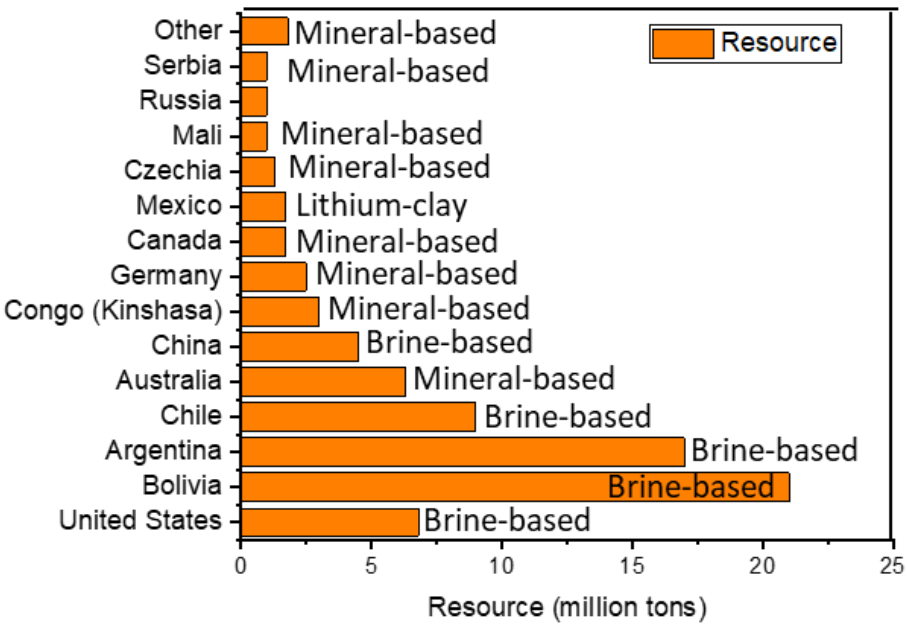


Figure 2.2Countries with the lithium reserves worldwide as of 2020[62]

This trend is expected to continue in the coming years. Tesla planning to build 3 terawatt-hours of battery capacity to sustain its vehicles by 2030. That is a more than 50-fold increase over the current available supply. Tesla CEO Elon Musk recently announced that he expects the industry would be able to produce 30 million battery-powered electric vehicles by 2027 considering that other manufacturers also continue to build EV models.[46] In 2019, approximately 2 million EVs were sold globally, which was about 740,000 units at the end of the 2014. A typical electric vehicle (EV) battery cell contains just a few grammes of lithium. That equates to about a half teaspoon of sugar. A typical EV can have up to 5,000 battery cells. From there, a single EV contains approximately 10 kilogrammes of lithium. A tonne of lithium metal is enough to produce approximately 90 electric vehicles. The production of a million cars necessitates the use of approximately 60,000 tonnes of lithium carbonate equivalent. As Musk stated, 30 million vehicles equate to approximately 1.8 million tonnes of lithium carbonate equivalent, or 5 times the size of the total lithium mining industry in 2019. Lithium is extracted mainly from hard rock mines, such as those in Australia, or deep brine lakes under the surface of dry lake beds, primarily in Chile and Argentina. According to an analysis conducted by the raw materials experts for the lithium and geothermal energy company Vulcan Energy

Resources, hard rock mining in which the mineral is mined from open pit mines and then roasted using fossil fuels causes environmental damage, requires a significant amount of water, and emits 15 tonnes of CO_2 per tonne of lithium. The other conventional option is to extract the lithium from underground wells which demand even more water to extract the lithium. It is important to note that a tonne of lithium metal requires approximately 5.3 tonnes of lithium carbonate. Moreover, LIBs usually use cobalt and nickel as part of the cathode material which are both rare and expensive, and use of those metals is an issue for scaling up more batteries to satisfy our energy demand in the future.[63] Amnesty International[64] has recorded significant human rights abuses associated with the mining of minerals used in lithium-ion batteries, especially in the Democratic Republic of the Congo. According to investigation proceeded in 2016, children and adults employed in hand-dug cobalt mines in southern Democratic Republic of the Congo face significant health risks and are neither covered by the government nor valued by the companies that benefit from their labour. According to Amnesty International's report, these mines are connected to the supply chains of many of the world's leading electronics brands and electric vehicle manufacturers. Aluminium as a current collector would react with the lithium and cause the failure of the battery, LIBs must use a copper current collector for the anode. Copper is more expensive than aluminium which also increases the cost of the battery. In summary, based on the current trajectory LIBs will face resource constraints if current trends continue. The European Union has already classified cobalt and graphite, the other essential components of LIBs, as critical raw materials.[46] LIB demand would eventually exceed supply limits, resulting in price increases. These large-scale installations (electric cars, stationary storage systems) have already put tremendous strain on the LIBs supply chain; the production of alternative energy storage chemistries is becoming an imperative to alleviate the pressure. To solve the overreliance on finite resources, it is therefore important and urgent to engage in research efforts on alternatives to LIBs, substitute technologies which should base on abundant and low-cost resources.[65,66]

2.3 Sodium-ion Batteries: Rising Again from the Ashes

An investigation of the literature reveals that NIBs have been observed alongside lithium cells in all of the main laboratories since the early 1970s.[67,68] After most researchers changed their attention to LIBs after 1991, NIB research was put on hold for a while. Nevertheless, NIBs research was not totally abandoned, and the search for a candidate anode material continued during that time. Research on sodium ion batteries has then reaccelerated following the insertion of Na ion in hard carbon, where a high storage capacity of around 300 mAh /g was

achieved, which is comparable to that of LIBs using graphite as an anode (Figure 2.3b).[69] Since 2010, researchers have begun to revisit this previously discarded NIB technology and explore its possibilities as a supplementary technology to LIBs, in response to increasing concern about the sustainability of Li sources and their inconsistent distribution. (Figure 2.3a).

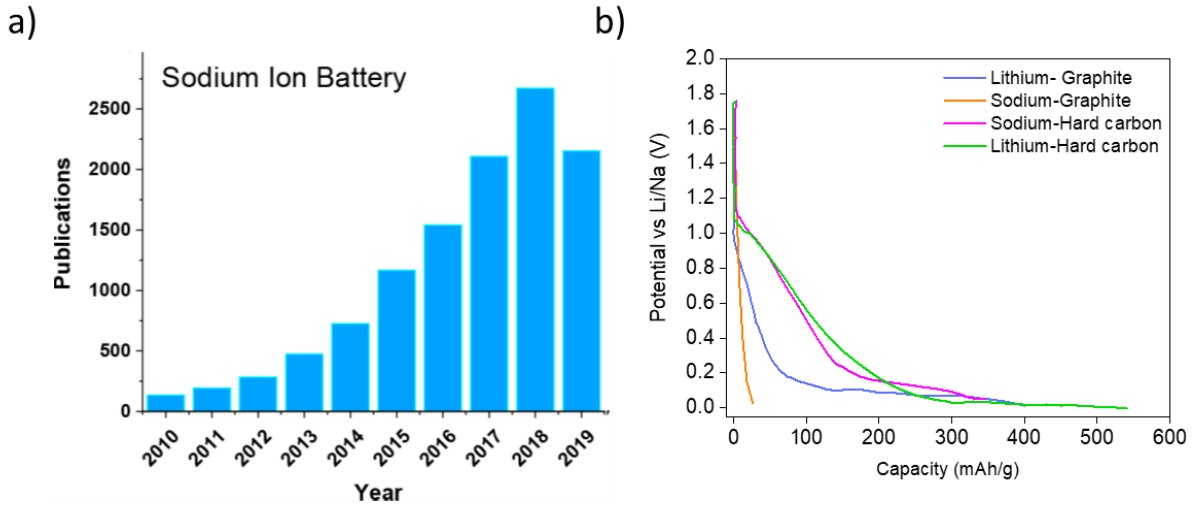


Figure 2.3 a) NIBs research growth as calculated by scientific publications (Source: Web of Science, Clarivate Analytics, Accessed Oct 9, 2019)[50] *b) Typical discharge profiles for sodium/lithium insertion in half-cell of graphite and hard carbon. Discharge profiles redrawn from the digitalization of previously reported data.*[70]

It is therefore advisable to use low cost NIBs with large reserves that can be used as large-scale energy storage systems where energy density is not a major concern. These additional systems are expected to be a relief a congested value chain of LIBs manufacturing, as well as to alleviate price spikes. Sodium supplies are widely dispersed in the Earth's crust (Na: 23 000 ppm vs Li: 17 ppm) and almost indefinitely distributed in the ocean; this not only lowers the expense, allowing economic competition, but also allows them less vulnerable to resource and supply threats. The working concept and material properties of NIBs are identical to those of LIBs. However, substitution of sodium-ions for lithium ions creates some differences. The primary distinction between the two ions is the sodium ion's larger ionic radius of 102 pm compared to 76 pm of the lithium ions.[71] Sodium has a significantly higher reduction potential than lithium, with -2.714 V and -3.045 V vs. SHE (standard hydrogen electrode) for sodium and lithium, respectively.[72] These are small variations, but they have a major effect on battery chemistry. For example, unlike lithium, sodium does not form any alloys with aluminium allowing for cheaper and lighter anode current collectors. The copper anode current collector used in LIBs can be replaced by lighter and less expensive aluminium foil while using a manufacturing process close to that of LIBs; this reduces production costs. [29,73–77] Moreover, because of Na-ion`s large ionic radius, it has a low solvation energy in polar solvents (roughly 30% less than

Li in organic solvents), resulting in lower interfacial transfer resistance and lower salt concentration for Na^+-based electrolytes with comparable ionic conductivity as Li-based electrolytes. Because of the sodium's higher reduction potential and slightly lower cell voltage, energy densities result in lower than lithium-based chemistries.[78]However, since commercial cells do not use metallic sodium or lithium, a battery's actual voltage is determined by the combination of negative and positive electrode materials. High voltage sodium-ion batteries can be created by combining suitable materials, and despite sodium's higher reduction capacity, there are NIB chemistries that have higher operating voltage than some common lithium-ion batteries. [79,80]

In 2011, Faradion Limited is a startup company established in the United Kingdom and was the first to commercialise NIBs. A nonaqueous electrolyte SIB technology focused on active materials consisting of a layered nickelate cathode and a hard carbon anode is being developed and commercialised by the group.[81]Then, the first sodium-ion battery in an 18650 configuration was established in 2015 by researchers in France's RS2E network on electrochemical energy storage (18 mm diameter, 65 mm height).[81,82] French-based Tiamat was founded in 2017 which is a spinoff company from RS2E. The company has started to develop cylindrical NIB cells with a polyanionic compound cathode, $Na_3V_2(PO_4)_2F_3$ (NVPF), and hard carbon (HC) anode. Tiamat has generated over 10,000 NIB cells delivering 122 Wh/kg at 1C rate. The cells have a high power rate capacity (90% at 1C) and a long cycling life (>4,000 cycles); however, the underlying downside is rooted in the use of harmful vanadium, which scientists are attempting to mitigate by replacement with less toxic and more accessible 3d metals.[83] Finally, HiNa, based in China, was established in 2017 as a spinoff from the Chinese Academy of Sciences' Institute of Physics (IoP-CAS). They are manufacturing both 10 Ah pouch and 18650 cylindrical cells with a patented $Na_{0.9}[Cu_{0.22}Fe_{0.30}Mn_{0.48}]O_2$ cathode and an anthracite-based HC anode and with a gravimetric energy density reaching 135 Wh/ kg, with 90% capacity retention by varying the discharge rate and a cycle life of over 3000 cycles.[84] More about apparent advantages that make NIBs suitable for commercialization, it is also scientifically true that the inherent properties of sodium cause NIBs to be inferior to LIBs in some ways, which must be resolved further by integrating studies in the field. For example, NIBs cannot associate with LIBs in terms of gravimetric and volumetric energy density when a comparable material system is used since Na has a higher atomic mass and a greater ionic size. Even when the same electrode material used in the cell, the Na storage mechanism can vary from that of lithium. As a result, a better

understanding of the sodium storage system would allow for the design of advanced electrode materials. Innovation in materials is critical to reimbursing for the lower specific energy density and making NIBs efficient compared to LIBs in terms of cost per kilowatt hour. The different charge carriers (Na^+ vs Li^+) interact with the host electrode structure in very different ways during the charge discharge process, resulting in major differences in phase behaviour (crystal structure, coordination, volume change), diffusion kinetics, and electrode/electrolyte interface (solvation-desolvation, charge transfer, composition, compactness, and thickness). Thus, the thought of replacing Li with Na to reduce cost would be mistaken, just as the transition from LIBs to NIBs was not as simple as replacing the alkali metal. Understanding and improving performance from the material to the interface to the cell level would be crucial in providing fundamental solutions to the commercialization of NIBs.

2.4 Cost comparisons

Before LIBs and NIBs are compared in terms of battery cost, it is important to emphasise that NIBs are not a competitive alternative to LIBs, but rather a complementary product. NIBs will not replace LIBs, but they will diversify the battery market based on demand for different applications, alleviating the burden of depending on LIBs' critical materials. The advantages of the NIB on a material basis become apparent as the contribution of the battery materials to the final cell costs (Figure 1.6) is considered. Important cost advantages are achieved per single cell for the NIB cathode active material due to the use of less costly raw materials, as well as for the anode current collectors due to the avoidance of copper (aluminium is significantly cheaper than copper). The carbonates that constitute a brine supply of Li and Na are priced at US$ 6600 per Mt for Li_2CO_3 and US$ 60 per Mt for Na_2CO_3.This cost calculations basen on only material`s prices was used to argue that the cost of NIBs would be much lower than that of LIBs, however, significant drop in the price of LIBs in 2019 shows that this is a misleading approach. Tesla's batteries, for example, cost 127 $/kWh in 2019.[85]These are the costs per single cell and do not take storage capacity into account. Comparison of the cell price (cost/kWh) and material (cost/kWh) shown in Figure 2.4, makes it becomes clear that how important the cell energy density is. The average price of a lithium-ion battery cell in 2018 was 127 $/kWh, with a pack price of 176 $/kWh. Since lithium is more costly than sodium, the intuitive notion that the price of NIBs will be cheaper than that of LIBs is false. A new cost analysis of NIB and LIB technologies showed that replacing Na with Li lowers prices by 10–30% at the materials stage, which decreases to 4.3 percent when processing costs are factored

in.[86]Because of the different energy densities given by these different chemistries, different storage capacities have a significant effect on cost.

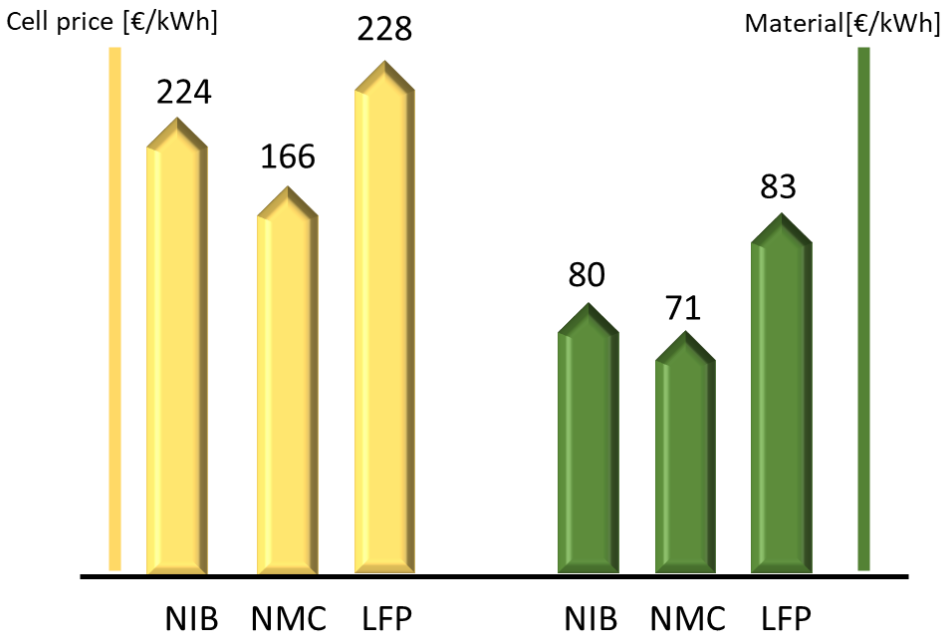


Figure 2.4 The cost of a cell per kWh of storage capacity is broken down into battery components and battery materials.[85]

Peters et al.[85] recently published a comprehensive economic evaluation of 18650-type NIB cells with a layered oxide cathode and a hard carbon anode. The findings from existing datasheets for pre-commercial battery cells were compared to those of LIB cells with lithium-nickel-manganese-cobalt-oxide cathodes (NMC) and lithium-iron-phosphate cathodes (LFP). The LFP battery has the highest price per kWh of storage capacity (229.3 /kWh), followed by the SIB, which has a price per kWh of 223.4 /kWh. Because of its high energy density, the NMC-type LIB is the most economical (168.5 /kWh). Despite historically high raw material costs, the final price per Wh of storage space of the NMC-type LIB is lower than that of the LFP-type LIB and NIB, demonstrating the value of energy density. Therefore, in stationary applications, the NIB may be a promising replacement for LFP cells, if it also competes with LFP cells for safety and cycle life. As a result, performance metrics are important for the NIB technology to maintain a reasonable cost per Wh and, eventually, find a market position. It should be remembered that highly promising findings have been obtained in a relatively short period of time as opposed to the Li-ion technology after 30 years of research. It is anticipated that the optimisation of the device manufacturing/assembly from the point of view of applied research would yield more technical advancement, future study efforts shall be directed at

fundamental analysis, the finding of materials and the comprehension of the thermodynamic and kinetic processes governing the chemical characteristics.

2.5 Technical Information about Batteries

There are several important parameters that helps to understand main characteristics of secondary batteries. The following battery characteristics including the specific capacity, energy density (gravimetric and volumetric), rate capability, and the initial Coulombic efficiency (ICE), must be taken into consideration when characterise a battery.

2.5.1 Theoretical Specific Capacity, Specific Energy and Specific Power

Specific capacity means the capacity stored per unit mass of electrochemically active material, and the unit is known as milliampere-hour per gram (mAh/g).[87] The specific theoretical capacity (Q_t) can be calculated from the equation as follows.

$$Q_t = \frac{x\ 1000\ F}{3600\ M}\ mAh/g$$

where F is the Faraday constant (96485 C/mol), M is the molecular weight of the active material (M) of the electrode and x represents the number of moles of electrons.

2.5.2 Charge and discharge

An assembled battery has always an open cell circuit potential, but it exhibits different cell potentials when the battery is in operation. Battery potential rises and falls during the charge and discharge process, respectively.[88] The reason of the low potential of the discharge process is the internal impedance of the battery, which is caused by polarization losses at the electrodes, ohmic resistance in the current-collectors, electrolyte and active materials.[88,89]the specific capacity during galvanostatic charge/discharge is calculated by

$$Q = \frac{I\Delta t}{3.6\ m}\ mAh/g$$

where I (mA) is the charge/discharge current, Δt (h) is the charge/discharge time and m (g) is the mass of the active material.

2.5.3 The gravimetric energy density

The gravimetric energy density is defines as the battery capacity per unit weight. The unit of energy is watt-hours (Wh= V x Ah) or J (1 Wh = 3600 J) equals to one watt of power consumed for one hour. The gravimetric energy density is generally described in watt-hour per kilogram (Wh/kg). The integration of the voltage and the specific capacity gives the gravimetric energy

density of a full cell. The theoretical gravimetric energy density of the cell can be calculated from the following equation;[90]

$$\Delta G^o = \sum \Delta G_{f^o_{products}} - \sum \Delta G_{f^o_{reactants}}$$

the Gibbs free energy of the reaction under standard condition (ΔG^o) can be calculated from the sum of the formation energy of the reactants and products. The maximum electrical work from this reaction equals to ΔG^o, as shown in the Nernst equation:

$$\Delta G^o = -nEF$$

where n refers to the the number of transferred electrons of one mole of reactant and E is the thermodynamic equilibrium voltage and F is the Faraday constant. Therefore, the theoretical gravimetric energy density can be calculated as:

$$\epsilon_M = \frac{\Delta G^o}{\sum M}$$

Where $\sum M$ is the sum of the formula mole weights of the all reactants. In practical situations, the energy density is determined as

$$\epsilon_{cell} = \frac{I}{3.6\, m} \int_{t_1}^{t_2} U(t)dt$$

Where U is the working voltage window, and m is the total mass of active materials in both anodes and cathodes in grams, and Δt (s) is the charge/discharge time. The volumetric energy density could be calculated in the same way but replacing the mass with the volume.

2.5.4 The rate capability (C rate performance)

The rate capability is a measure of the reversible capacity of an electrode at different current densities. A 1C rate means that the current will discharge the entire battery in 1 hour. For example, for a battery with a capacity of 100 Ah, C associates to a discharge current of 100 A for 1 hour. A rate of 2C would be 200 A and would require 30 min of discharge, and a 0.5 C rate would be 50 A and would require two hours of discharge.

2.5.5 Initial Coulombic efficiency

Coulombic efficiency is a parameter to monitor the extent of side reactions in a battery. CE also known as Faradaic efficiency, describes the electron charging efficiency and the ratio of the total charge removed from the battery to the total charge input over a full cycle. To maintain a high enough Coulombic efficiency during the charge/discharge time, good interface and structural reliability is needed, and it is revealed that 99.96 % Coulombic efficiency is required

for commercial batteries when cycling to over 500 cycles.[90] The coulombic efficiency η (%)is calculated by equation below[91]:

$$\eta = \frac{Q_d}{Q_c} x100$$

where $Q_d$and Q are the discharge and charge times, respectively. If η is lower than 100%, then there is some charge lost to processes other than the reversible sodiation/desodiation reaction.

2.6 Hard carbon anode materials for NIBs

Proposed anode compounds for NIBs can be classified in four categories: carbonaceous materials, oxides based on conversion reaction, p-block elements (metals, alloys and phosphorous) and organic compounds. In this section, the most recent progress in negative electrode materials research for NIBs will be reviewed and this thesis will mainly be focused on carbonaceous materials. The conceptual similarity of NIBs and LIBs lead one to expect that both battery systems have similar cell reaction mechanisms.[92–97] However, since Na has a greater radius than Li, it has an adverse effect on bulk transportation and storage in the electrochemical process. The most common anode for commercial LIBs is graphite, which has a layered structure with a long-range order, and Li can easily electrochemically intercalate between the graphite layers. The use of graphite as anode in LIBs shows a theoretical capacity of 372 mAh/g and a long cycle existence.[30] On the contrary graphite thus exhibits poor electrochemical sodium storage for NIBs which is only 35 mAh/g. [98] The interlayer distance of graphite (~0.34 nm) is too small to accommodate the large Na ion in the conventional electrolytes, as shown by recent theoretical calculations for insertion of Na a minimum interlayer distance of ~0.37 nm is thought to be necessary. The use of graphite as anode in LIBs shows the ability to form the stage 1 graphite intercalation compound (GIC) LiC_6.[30] On the contrary, stage 1 Na-GIC formation has never been observed and they reported to be thermodynamically unfavourable (and only higher stage compounds, NaC_{48}, NaC_{64}, NaC_{80}, have been reported) ,thus graphite exhibits poor electrochemical sodium storage for NIBs.[98–100] The typically given reason for that is the size of Na ions being larger than Li ions, therefore have intercalating difficulty in graphite. Nevertheless, alkali metals with larger ionic radius than Na, such as potassium (K), caesium (Cs), and rubidium (Rb) can intercalate into graphite as they are found to be chemically more stable than Na and can show an ability to form GICs. Moriwake et al. indicated that changes in chemical bonds between alkaline metal (AM) atoms and C atoms are the main explanation for these changes. GIC AMC_6 (where AM = Li, Na, K, Rb, and Cs) calculated formation energies in which an ionic connection is decreased by a

decrease in ionic size from Cs to Na, resulting from a weakening of ionic bonding, to the point where ion formation energies of NaC_6 are found to be less negative (less stable). An exception to this pattern is the much smaller Li-on, since it contains a covalent component in its bonds with C atoms, which results in a negative energy for formation. These slight staging variations in the various alkaline metals illustrate why graphite. Intercalation of graphite with lithium and other metals with larger ionic size, but sodium's inability to do so may be explained by standard voltage reduction potential versus $2H^+/H_2$. The standard reduction potentials for Li^+/Li, K^+/K and Na^+/Na are -3.0, -2.92 V and -2.7 V, respectively. In an electrochemical profile of lithium/graphite, a long plateau appears in the region from 0.2 V to 0.1 V due to intercalation of lithium ions in the graphite whilst the same process for sodium ions is likely to occur roughly between -0.1 V to -0.2 V below the sodium plating potential. Thus, a long plateau region cannot be observed in an electrochemical profile of sodium/graphite as sodium metal is expected to start plating onto the graphite surface before intercalation occurs.[101] As a result, the limitation of graphite as a NIB anode material has hence led to alternative anode materials for NIBs being pursued.[30,102]

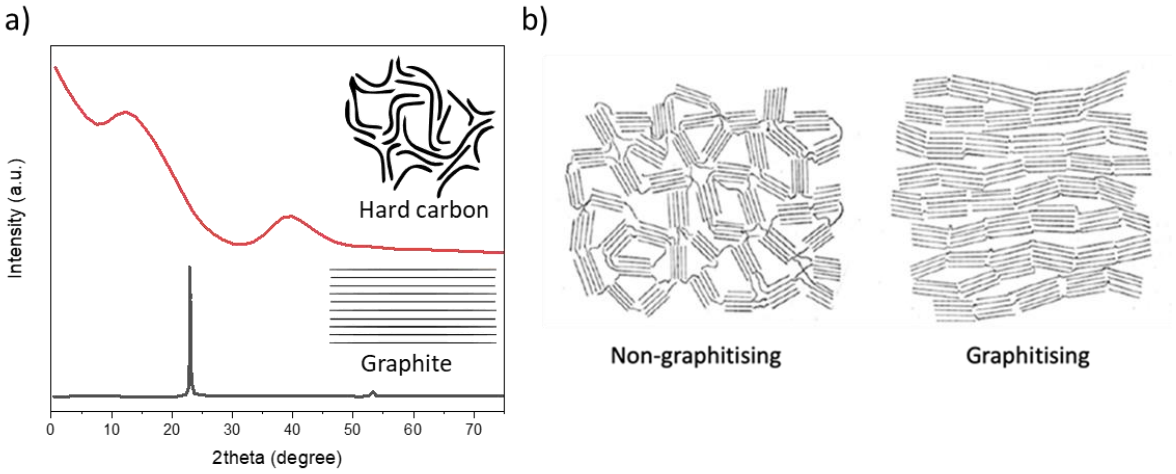


Figure 2.5) a) Typical X-ray diffraction patterns (Cu K-alpha source) of hard carbon and graphite, b)) Franklin's representations of non-graphitizing and graphitizing carbons[103]

Hard carbon is also known as non-graphitic or disordered carbon which contains randomly oriented, short turbostratic graphitic nanodomains with larger interlayer distances than graphite (>0.34 nm), curved and defective graphene nanosheets, and closed pores between these disordered layers; crucially, it lacks the long-range in-plane order seen in graphite.[103,104] The term "hard carbon" refers to their mechanical strength, their ability to graphitize, is determined by the plasticity of their layered structure.[27,33,103] This plasticity is prevented in the fine structure of hard carbon, which induces mechanical hardness and inability of graphitization,

even at temperatures above 3000ºC (non-graphitizable carbon). In the 1930's, the first amorphous carbon model was recognised by X-ray diffraction (XRD) of carbon black and reported by Warren.[105] The second model also was described by XRD measurements and revealed that the amorphous carbon structure could not rearrange into ordered graphite structure, even at high annealing temperatures were named non-graphitizable carbons or hard carbons. Hard carbons present a significantly high degree of mechanical hardness due to the presence of strong sp^3 crosslinking bonds, which will not allow movement and reorientation of the carbon atoms to form the ordered layer structure of graphite.[106,107]Typical X-ray diffraction patterns of hard carbon and graphite can be seen in Figure 2.5a. In a significant paper entitled "The analysis of diffuse x-ray carbohydrates," published at Acta Crystallographica in 1950, Rosalind Franklin explains the first structure of the graphitizable and non-graphitizable carbon (Figure 2.5b).[108] There are still several questions about hard carbon's internal structure which especially address the impact of structure on electrochemical behaviour. An intense research effort has been made to produce hard carbon from raw biomass and biomass waste such as glucose,[69] sugar,[109] cotton,[97] pomelo peels,[110] sugar,[109] apple wastes,[111] corn cob,[112] mangosteen shells,[113]peanut shell[114] and okara[114]. Depending on the initial precursor and carbonization procedures the ultimate carbon material properties such as particle size, amount of defects both at basal plane and edge sites, pores size and interlayer distances can be vastly different.[115–117] In 2000s, Stevens and Dahn reported most commonly accepted structural model for hard carbon, the "falling card" model suggests the appearance of small graphene sheets, defective amorphous areas, and nanopores in the hard carbon structures.[69]

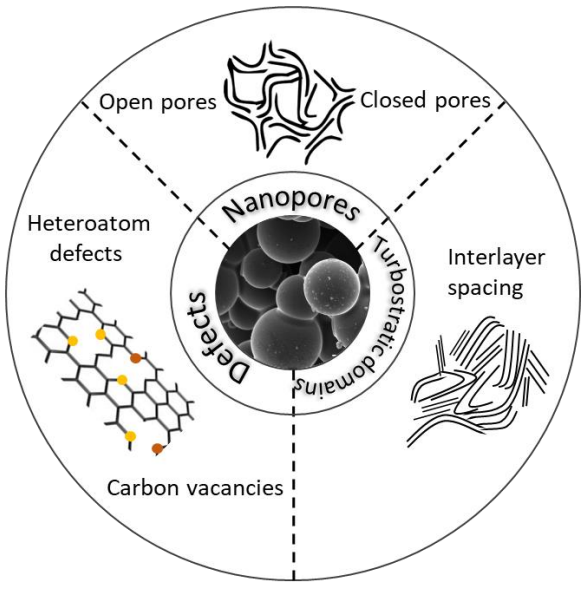


Figure 2.6 Illustration of the ion storage sites of hard carbon

The small graphene sheets in hard carbon (also known as graphitic domains) are arranged in a short range and have a limited lateral dimension of two to six layers of stacking. Studies have shown that parallel layers of graphitic domains are curved, bent or turbostratic rather than horizontal, as in the model 'falling cards' model. The (002) interlayer spacings of hard carbon are 3.6–4.0, which are greater than the 3.35 for graphite. Nanopores, which are either open or closed in the hard carbon structure, are another vital but complicated elements of hard carbon. The open pores lead to large, specific surface areas, resulting in an overly poor initial coulombic efficiency, whilst closed pores are preferable to active sites for the accommodation of alkali metal ions. Besides these sites, hard carbon structure also has vacancies and defective sites at basal plane and edges. In the hard carbon, the majority of the carbon atoms are in the form of six-member carbon rings, while there are also several pentagonal or heptagonal defective sites. The defect content can differ with the properties of the precursors. Since ions can be stored in hard carbon materials through adsorption on the surface and defects, pore filling, and intercalation between graphene layers with wide interlayer spacing, structural differences influence the ion storage capacity within the hard carbon material. Hard carbons demonstrated very high capacities up to 350 mA h/g. However, it is important to mention that it would be inaccurate to draw conclusions only based on capacity performance as electrode material, loading masses and cell preparation protocols vary from paper to paper. There should be universal metric to make a precise comparison. Precursor can mainly be classified into three sections: carbohydrates, raw biomass and phenolic resin. Stevens and Dahn reported a glucose-derived hard carbon with a reversible capacity about 300 mA h/g,[69]which was soon followed by Thomas and Billaud with similar findings using cellulose (Figure 2.7).[118] Komaba's work in 2011 showed reasonably good performance of 240 mAh/g with coulombic quality, and cyclability using a hard carbon from Carbotron (Kureha) which had been formed from oxidised pitch for use in commercial LIBs.[119] Ponrouch et al. demonstrated quite good reversible capacity of 326 mA h/ g at 37.2 mA/g by using sugar precursor, despite the fact that the first cycle coulombic efficiency was just 60%.[109]

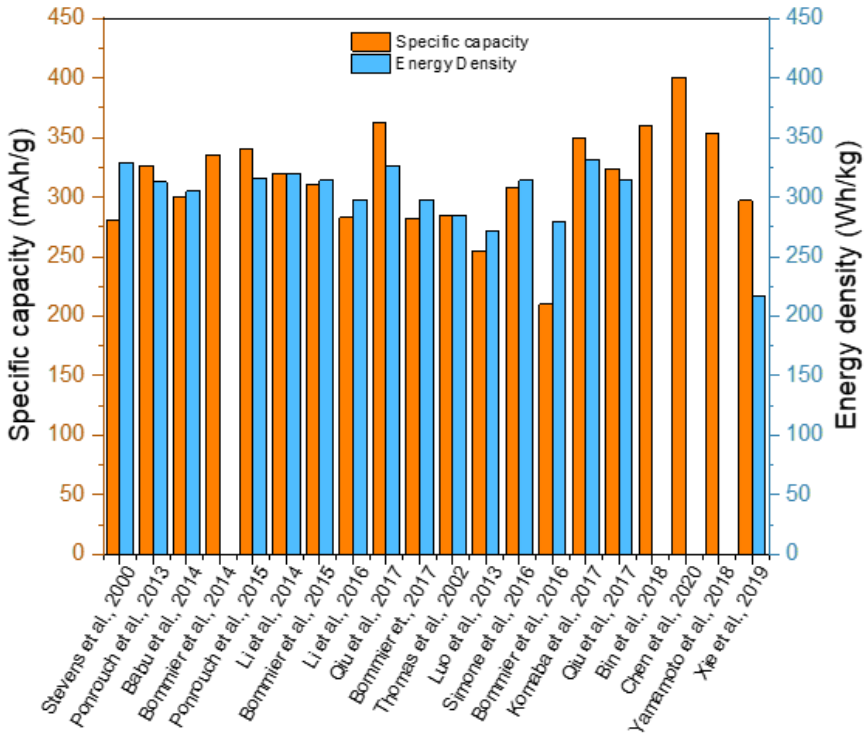


Figure 2.7 An overview of the electrochemical performance of hard carbons at low rates (40 mA/g or less).

After that, several groups looked into sugar precursors in order to make hard carbons with a better Coulombic efficiency and stable reversible capacity.[120–123] Bommier et al. managed to achieve a reversible capacity of 335 mA h/g and a reasonably consistent long-term cycling at 300 mA/g (500 cycles). [35]Additional enhancements were represented by the same group with changing the surface area, for example by adding graphene oxide to sugar as a dehydration agent that results in a low surface area of 5 m^2/g (obtained from the N_2 gas measurements), they enhanced the Coulombic efficiency beyond 80% while retaining the other performance metrics.[124] Ponrouch and Palacin were able to further enhance the performance of sugar derived hard carbon by applying a post-carbonization carbon coating to reduce the specific surface area and maintaining high capacity of 325 mA h/g at 37.5 mA/g, researchers also were able to achieve a significant increase in coulombic efficiency (55 to 80%).[125] Hard carbon-anode materials made from a variety of precursors of biomass such as sucrose, glucose, cellulose, maltose and glycogen were investigated by Komaba and coworker. In their study, hard carbon has been synthesised via heat treatment in two stages: preheating and carbonization. Precursors had been prepared by pre-heating at various temperatures and carbonised at 1300 °C. in Ar flow. It is evident that the hard carbon derived from cellulose provided best performance and the specific capacity was further increased by a pre-heating temperature of 275 °C. It was found that a high-temperature pre-heating treatment would result

in dehydration, formation of covalent cross-linkage of cellulose molecules, and interrupts graphitization during the high-temperature carbonization process and increases the number of sodium storage sites by increasing the number of pores and interlayer spacing.[126] A variety of sucrose derived hard carbon materials containing low-defect and low-porosity have been studied, with electrode morphology being linked to electrochemical efficiency at various heating rates. Lower heating rates resulted in more ordered systems and smaller specific surface areas, yielding high specific capacities of 361 mAh/g and Coulombic efficiency of 86.1%. In the same work, the lowest defect concentration and undetectable porosity is discovered to be the reasons of the highest specific capacity and Coulombic efficiency. In addition to biomass, several reports on hard carbons provided by polymers like polyacrylonitrile (PAN) have recently been published.[115,127] These PAN and PANI derived carbons provide smaller capacities and Coulombic efficiencies than those of the better performing biomass and resin-based hard carbons. Although biomass has an advantage in terms of high performance, sustainability and abundance, the total cost appears higher than graphite.[126] As a result, there is still a long way to go before biomass-derived hard carbons are understood and used in industrial scale high-performance NIBs.

2.7 Mechanism of Na-ion storage in hard carbon

Developing new materials signifies a crucial research field for the improvement of rechargeable batteries; underpinning this, understanding the sodium storage mechanisms in the host structure is the most important mission for advancement of high-performance hard carbon anode materials for NIBs.[27,37,107,115,128] For hard carbons, the characteristic charge-discharge profiles generally show a sloping region between 1.0 and 0.1 V, and a plateau below 0.1 V. In the literature, these two regions have been ascribed to different sodium storage mechanisms. Although several research groups have contributed to exceptional research advancements in the fields of hard carbon anode materials for NIBs, the sodium storage mechanisms in carbon anode materials remains elusive. It is difficult to provide a precise and full image of the charging storage mechanisms because the published literature does not always clearly state the critical structural features of the electrode and their relation to the electrochemical performance. For example, it is important to understand whether electrolyte has access to the relevant pores or otherwise if sodium ion access requires desolvation, conversion and additional mass diffusion. Another factor leading to apparent contradictions may be the inhomogeneity of hard carbons with different crystallite sizes, pore structures, heteroatoms, etc.

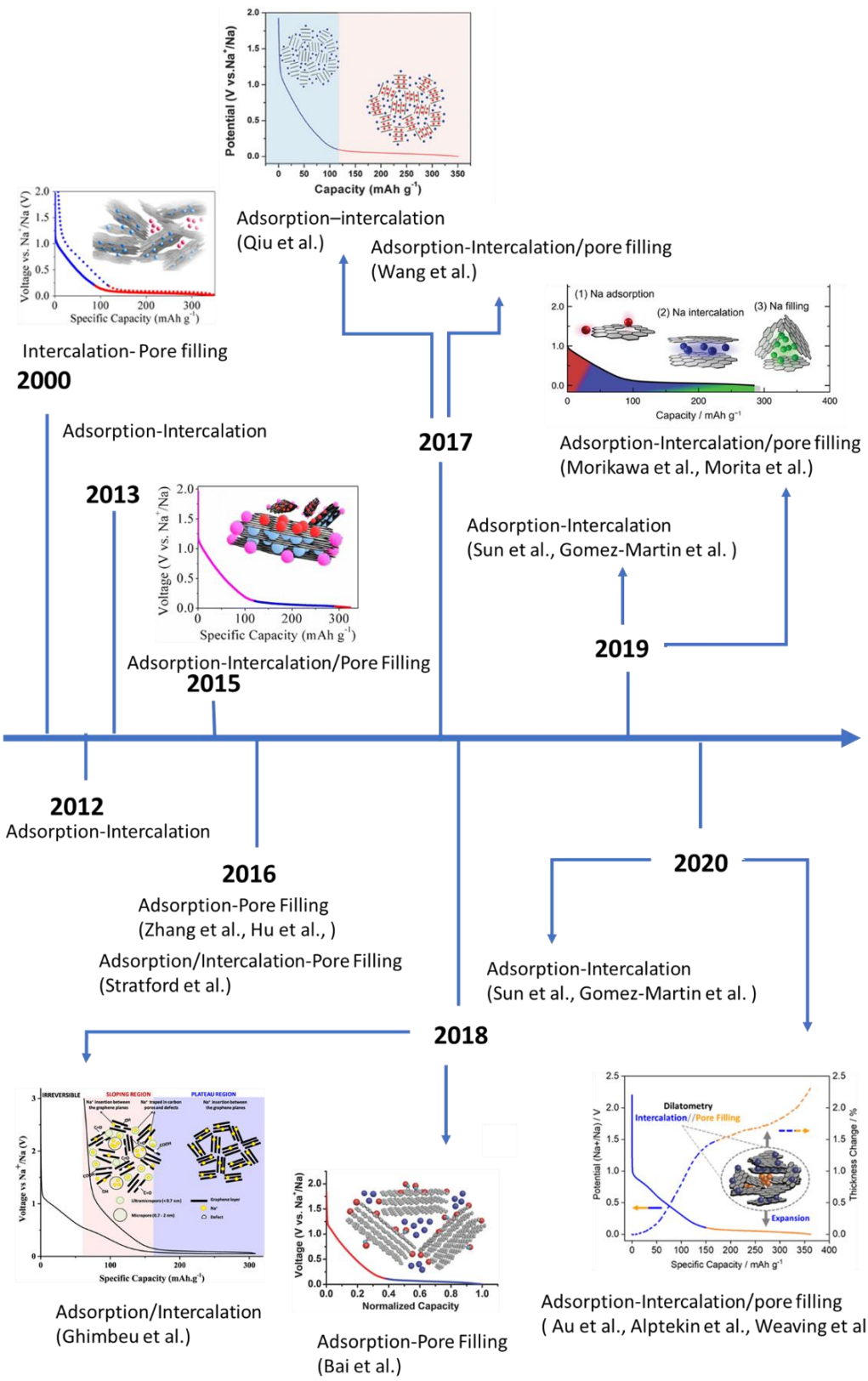


Figure 2.8 Representative schematics proposed for the sodium storage mechanism in hard carbon over years.

The sodium storage mechanisms in hard carbons can be divided into three groups:

i) Sodium ion absorption at the electrode surface, which may be related to defect sites on the surface as well as the presence of heteroatoms or functional groups.

ii) Sodium ion intercalation into graphitic layers.

iii) Sodium ion filling inside the nanopores.

In 2000, Stevens and Dahn[69] first reported the 'intercalation-filling' model for sodium ion storage mechanism which is similar storage mechanism proposed for lithium. By using *in-situ* WAXS experiments, Dahn *et al.*[129] observed a shift in (002) peak position to lower angles suggest that the layers are being moved apart when interlayer insertion occurs. The decrease in the peak intensity upon sodiation, corresponds to the presence of scattering species between the layers which is attributed to intercalation of sodium-ions into the graphene layers of the turbostratic nanodomains. Based on *in situ* SAXS measurements,[31] when cell discharged along the low voltage plateau, the intensity of the scattering from the nanopores and the contrast between the pores and the carbon matrix decreases while electron density in the pores increases. Therefore, authors attributed the low-potential plateau region to sodium-ion insertion into the nanopores between randomly stacked layers through an adsorption process. In 2011, Komaba *et al.*[130] further proved 'intercalation-filling' mechanism through the use of Raman spectroscopy, *ex-situ* PXRD and e*x-situ* SAXS analysis in commercial hard carbon. Authours discovered that when the battery discharged along the sloping field, the interlayer spacing widened. Besides that, the SAXS signal from the micropore seems to have reduced when discharged to 0 V. A decrease in the intensity of scattering from the pores indicated that sodium ions inserted into the nanopores within this voltage range. As previously mentioned, the findings support the “intercalation-filling” mechanism. In 2016, Grey *et al*.[34] used *operando* ^{23}Na solid-state NMR and pair distribution function analysis to investigate sodium storage mechanisms in hard carbon electrodes. The ^{23}Na NMR signal remained ionic within the high-voltage sloping area and became more metallic as the discharge process continues at low voltage plateau region. It was hypothesised that ionic interactions take place mostly near defect sites, and that metallic interactions take the form of Na clusters that form in the pore structures. The pair distribution function measurements for the sodiated electrodes agree with this analysis of the NMR results. It reveals the additional structure development during a low voltage area, which involves a correlation with the creation of approximately 10 Å Na cluster during the low voltage plateu region. Therefore, authors attributed high potential to Na-ion intercalation between graphene sheets with large interlayer spacing and Na plating in pores at

low potential. Recently, Au et al., studied structural changes – charge storage relations in hard carbons. From their *ex situ* ^{23}Na solid state NMR study, also concluded that the low voltage plateau is associated with the formation of sodium clusters. To further explain the logic of the nanopore filling mechanism, Xu et al.[131] used a vacuum evaporation approach to embed sulphur in hard carbon, eliminating the inner nanovoids. *Ex-situ* Raman spectra revealed no change in the place of G-band peak in either ether or ester electrolytes, the G-band shifting is expected if sodium intercalation occurs in hard carbons. Furthermore, XRD observations explicitly showed that no (002) peak change was observed at various charge-discharge states of the HC anodes, indicating that no intercalation occurred regardless of the electrolyte. As a result, authors findings rule out the existence of an intercalation process and supports adsorption-pore filling mechanism. In 2012, Cao *et al.*[132] proposed a different opinion on the sodium storage mechanism in carbon nanofibres (CNFs) derived from polyacrylonitrile (PAN). In their work, the high-voltage sloping region is attributed to the charge transfer on the surface of small graphitic clusters and the low-voltage plateau region is attributed to Na-ion insertion in the interlayer of nanodomains. By using theoretical simulation, they also proposed that Na-ion can only insert into carbon layers when the interlayer spacing is greater than 0.37 nm. Ghimbeu et al.,[133] reported that there is no porosity for sodium to fill in cellulose-derived carbon, so the plateau capacity is due to Na-ion intercalation between the graphitic domains. It should however be noted that the pore volume obtained from the BET addresses only the open pores (gas accessible) and the closed pores are usually considered important for the pore filling mechanism. Tarascon *et al.*[115] studied the mechanism of hard carbon by using polyacrylonitrile (PAN)-derived carbon nanofibers (CNF) under various carbonization temperatures. These carbons were characterized using in- situ XRD and there was no apparent (002) peak shift observed during the sodiation, indicating that the Na ions did not intercalate into the graphitic layers. However, it could not be deduced clearly due to the data's low resolution. Furthermore, authors report that sodium metal plating occurs at about 0.015 V (vs. Na^+/Na), and therefore the plateau capacity could not be due to either intercalation or sodium plating. The role of heteroatoms, such as O and N, in the advancement of the high voltage sloping area was clarified. Morikawa et al.[134] recently explored sodium storage mechanism of a series of nanostructured hard carbons using by combining *ex situ* SAXS/WAXS measurements. The findings from WAXS pattern of the sodiated electrode demonstrated that a (002) peak move to a lower angle compared to pristine electrode, indicating that the expansion in the interlayer spacing. The SAXS data shows that after the sodiation process, the scattering

intensity decreases, suggesting that the nanopores were filled with sodium. Finally, the authors proposed that the plateau potential is influenced by both intercalation and nanopore filling mechanisms. According to their mechanism, the slope region was attributed to sodium ion adsorption on disordered graphitic sheets and the plateau region to the sodium ion filling into pores. Great progress has been made in the sodium storage process of hard carbon as a result of continuous study over the last few years, but it remains inconclusive and needs to be further studied.

2.8 Cathode materials for NIBs

In the synthesis of SIB cathode materials, the synthesis methods evolved over the decades for the LIB can be smoothly implemented. Therefore, there is a wider range of material options for the cathodes compared to anodic materials. They can be categorised in three major classes as layered metal oxides, polyanion compounds and Prussian blue analogs (PBA).[135,136] The majority of layered metal oxides crystal structures are known as either P2-type or O3-type. The letters P and O here represent the prismatic and octahedral sites of the alkaline ions and the numbers 2 and 3 are the number of layers or stacks inside the repeated layered metal oxides structure. They exhibit complex phase change reactions during cycling.[137] The dynamic phase transitions lead to structural breakdown and capacity decay through the substantial contraction/expansion of the crystal structure and changing interlayer distances. Metal doping/substitution, as well as structural engineering, are useful approaches to minimise irreversible phase transitions and improve sodium storage properties with improved ion/electron transport.[138,139] Kalluri et al., have been prepared $Na_{2/3}Fe_{1/2}Mn_{1/2}O_2$ nanofibers with ordered stacking of nanocrystallines via an electrospinning method and demonstrated improved charge conductivity and good cyclability obtained due to the well-guided diffusion pathways within the structure.[140] The other type of widely investigated cathode materials is polyanionic compounds which contains sulfate $(SO_4)^{2-}$, phosphate $(PO_4)^{3-}$, and prylophosphate $(P_2O_7)^{4-}$ polyanionic groups exhibits robust structure and small volume expansion during electrochemical cycling.[141–143] The stable polyanion framework enables long cycle life for polyanionic compounds. However, they suffer from low conductivity which is holding them back from satisfactory electrochemical performance. In order to eliminate the effect of low conductivity, structural engineering and compositional control are required. For example, Fang et al.,[144] used hierarchical and highly conductive carbon framework to wrap and interconnect $Na_3V_2(PO_4)_3$ nanoparticles. The carbon matrix is comprised of graphene like layers and integrated nanofibers that connects the $Na_3V_2(PO_4)_3$ particles through an electronic wiring

pathway, enhancing their capacity and rate capability. Furthermore, the integrated carbon structure acts as a strong and adaptable buffer to handle volume changes caused by repetitive Na ion insertion/extraction during charge and discharge cycles. Prussian blue (PB) and its analogs (PBAs, Na2M[M`$(CN)_6$]: M: a N coordinated transition metal, M`: a C-coordinated transition metal ion , M = Fe, Co, Mn, Ni, Cu, etc.) are a large family of transition-metal cyanides. Due to their open framework structure, rich redox-active sites, and structural strength, they are considered to be promising cathode candidates for NIBs. Particularly, their large ionic channels and interstices in the lattice can enable to accommodate and reversibly intercalate larger amount of alkali cations. [135,145] While many metals can occupy the M′ site in PBAs, Fe is the most widely used. Also, different PBAs with various M metals were investigated, with a particular emphasis on those containing Fe and Mn. Fe containing PBAs often have low capacities and low operating voltages, resulting in inadequate energy densities; whilst Mn-based PBAs have higher working voltages, and they typically have low cycling stability due to Mn^{3+} Jahn–Teller's distortion. Furthermore, PBAs still face many challenges for commercial applications. A possible toxicity from cyanide release is a safety issue for Prussian blue products. Comprehensive toxicity studies have shown that Prussian blue itself is nontoxic and human friendly; nevertheless, when they exposed to high temperatures or strongly acidic conditions, it decomposes to form free cyanide CN, which is highly toxic and contaminative. As a result, considerable consideration must be given to the disposal of chemical waste. Because liquid chemistry typically is the basis of PBAs, their lattices contain several coordinated water and/or interstitial waters (above 15 per cent) that are likely to cause lattice distortion and even structural failure during Na^+ extraction/insertion processes, resulting in low specific capacity, low energy efficiency, and degradation of electrochemical performance. To tackle this limitation, Goodenough[135] published a simple method for removing interstitial water from the $Na_2MnFe(CN)_6$ lattice by drying the as-prepared sample in air/vacuum at 100 °C for 30 h, and discovered a vastly improved Na^+ insertion ability and cycling efficiency. PBAs with a high Na content, few vacancies and low water content are expected to have high capacity and robust structures with few vacancies. Therefore, achieving ideal PBAs with above mentioned criteria continues to be a key goal for commercial implementation.

2.9 Electrolyte/Electrode Interfaces

2.9.1 Electrolytes for NIBs

In batteries, the electrolyte plays a key role in transporting the positive ions between the cathode and anode. They are crucial for the proper functioning of any battery technology and focus in battery research is to determine the most appropriate formulation to minimize interface reactions, improve battery performance and build safer battery systems.[78,92] Essential requirements for the electrolyte include high chemical stability (no unwanted chemical reactions during electrochemical operation), good ionic conductivity, electrochemical stability (widest possible electrochemical stability window), thermal stability, low toxicity, sustainable chemistry (abundant elements) and low total cost.[92] All these features are intrinsically dependent on the nature of the salt and the solvent. Certain properties of NIB's electrolytes mostly come from the salts used, others from the solvents used, and once again it should be emphasised that the knowledge acquired from more than 30 years of LIB electrolyte production can and should be widely adapted to NIBs.

2.9.1.1 Sodium Salts

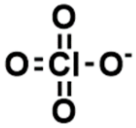
The essential part of an electrolyte is sodium salt, which has profound impact on electrochemical performance. Therefore, salt properties should be taken into consideration and ideal sodium salts should be able to fully dissolve and dissociate in the electrolyte, so that the sodium cation can move without encountering energy and kinetic barriers.[146] Electrochemical stability is also an important assessment criterion for sodium salts in terms of stable and protective interphases on electrode. The weakly coordinating anions (WCAs) are found to be stable to oxidation due to their suitably large gap between HOMO and LUMO energies. Anions in sodium salts consist of a stable central atom weakly bonded with electronegative outer ligands, which are conducive to the formation of delocalized negative charges for Na+-ion transport.[147]The advantages and downsides of the electrolyte are evidently determined by the anion properties. Thus, structural optimization of the anionic group plays an important role in the development of sodium salts. Lutz et al. reported that the nature of the solid electrolyte interphase (SEI) on metallic sodium anode depends heavily on the structure of the salt anion, and the choice of a conductive salt anion has profound influence on achieving stable cycling.[148] For NIB electrolytes, the same prospective anions are observed that have been used for several years in the field of LIB electrolytes; ClO_4–, BF_4^-, PF_6^-, $CF_3SO_3^-$ (Tf), and $[N(CF_3SO_2)_2]^-$ (TFSI). The most commonly used salts and their structural representations, physical and chemical properties are shown in the Table 2.1. $NaClO_4$ is the salt most

commonly employed salt in NIBs (in approximately 70% of the published NIB papers[118,148–152]). Eshetu et al.,[39] conducted a stability analysis on different sodium salts that demonstrated that $NaClO_4$ performance`s exceeds all of the other salts in terms of thermal stability. Although, it was widely used salt for Na-based batteries before, the use of this salt is no longer recommended due to its potentially explosive nature. Furthermore, another especially important problem about $NaClO_4$ is that despite its lower hygroscopicity, drying of the $NaClO_4$ salt is extremely difficult. When the water content of the electrolytes is compared in the literature, even after drying the powder at 80°C under vacuum overnight, electrolytes containing $NaClO_4$ salts usually show higher water contents (>40 ppm) than $NaPF_6$ based ones (<10 ppm).[153] The second most studied salt is certainly $NaPF_6$, as it enables comparisons with many LIB studies.

Although it is highly sensitive to water and easily produces highly corrosive HF, it still appears to be the most promising alternative for commercial systems. The resulting HF interacts with alkaline elements of SEI, weakening the solid surface layer by promoting high levels of harmful gases in the battery system.[154,155] It is thus generally regarded as the primary reason behind a fragile SEI. While $NaPF_6$ is much more electrochemically stable than $LiPF_6$, a recent study found that $NaPF_6$ can be more resistant to electrochemical reduction than its Li counterpart due to the high redox potential of Na^+ and its kinetic limitations. NaTFSI and NaFSI are emerging as strong Na-salt of alternative candidates due to their non-toxicity, higher thermal stabilities than both $NaPF_6$ and $NaBF_4$, and the corresponding higher conductivities than NaTf. Although they may not be suitable as single salts for NIBs electrolytes because they are extremely corrosive against aluminium (Al) which is commonly used as an anode current collector in NIBs to minimise battery mass and improve the energy density. Bhide et al.[149] showed the influence of the various salt concentrations on ionic conductivity using $NaPF_6$, $NaClO_4$, NaTf, and NaTFSI salts in EC:DMC solvent mixture. The dependence on electrolyte concentration was significantly more obvious for both NaTf and $NaClO_4$ than for $NaPF_6$. The maximum conductivities obtained is 6.8 mS cm^{-1} for 0.6 M $NaPF_6$, 5.0 mS cm^{-1} for 1 M $NaClO_4$, and the value obtained from 0.8 M NaTf is rather low. In addition to traditional salts, some new salts have also been synthesised; sodium-difluoro(oxalato)borate (NaDFOB),[156] sodium-4,5-dicyano-2- (trifluoromethyl) imidazolate (NaTDI),[157]and sodium-4,5-dicyano-2-(pentafluoroethyl)imidazolate (NaPDI).[157] The NaDFOB demonstrated greater conductivity, with more relocated charges and weaker interactions between the anion and the Na+ ion and shows good compatibility with different solvents. Similar benefits can be seen in specific salts

containing F atoms and heterocyclic ring structures, such as NaTDI and NaPDI. Even above 300 °C, both of these salts exhibited excellent thermal stability and formed a stable passivation layer which is preventing further corrosion reactions. Their large ESW of up to 4.5 V versus Na^+/Na and strong compatibility with ester solvents implies their potential for applications in NIBs.

Table 2.1 Structures and properties of most commonly used Na-salts for NIB electrolytes. [92]

Salt	Anion Structure	Mw (g mol-1)	T(oC)	σ(mScm-1)
$NaClO_4$		122.4	468	6.4
$NaPF_6$		167.9	300	7.98
$NaBF_4$		109.8	384	-

2.9.1.2 Solvents

A solvent is a substance which can dissolve another substance, the solute. For NIBs one or several organic solvents are used to dissolve a sodium salt to create an electrolyte. For better-quality cell performances, the solvents need to fulfil some prerequisites; for example, the ion-ion interaction is inversely proportional to dielectric constant (ε) of the solvent and a high ε solvent facilitates salt dissociation and increases the conductivity: as a result, a suitable solvent should be polar, have a dielectric constant greater than 15, restrict ion pairing, be electrochemically stable over a broad potential range, and be chemically stable. It is also necessary for the solvent to exhibit low viscosity for improved ionic mobility and to remain inert to the charged surfaces of the electrodes during electrochemical cycling to provide stability and promote the formation of high-quality passivation films. Last but not least, the solvent of choice should be safe, nontoxic, and economical.[158] The Gutmann acceptor (AN) and donor number (DN)[159] is a measure of the electron accepting and donating properties of

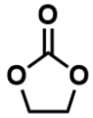
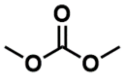
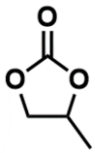
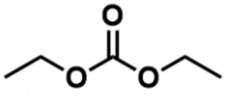
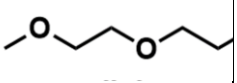
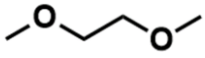
a solvent and therefore the ability to coordinate with cations. The higher DN, the higher basicity of the solvent, resulting in easy solvation of cations and the higher AN of the solvent associates with the higher basicity, resulting in easy solvation of anions.[159] The Lewis acidity/basicity concept (electron acceptor/donor ability) of a solvent is very important as it also has impact on the electrochemical stability window (ESW). The ESW of electrolyte is determined by the lowest unoccupied molecular orbital (LUMO) and the highest occupied molecular orbital (HOMO) of the electrolyte components. The prominent role of HOMO and LUMO in chemical reactions was studied first time by Shingu et al.[160]Then, further investigations revealed that the gap in between HOMO and LUMO is important for stability index, a large gap indicates low chemical reactivity therefore high stability, whereas small gap implies high chemical reactivity. [161,162] HOMO and LUMO terms will be explained in detail in part 2.10.

2.9.1.3 Carbonate Ester-Based Electrolytes

The most commonly applied carbonate solvents are focused primarily on two kinds of carbonate esters: cyclic carbonates (propylene carbonate (PC) , ethylene carbonate (EC)) and linear carbonates (eg, ethyl methyl carbonate (EMC), dimethyl carbonate (DMC), and diethyl carbonate (DEC)), shown in Table 2.2. Because of its advantageous properties, EC is one of the most appealing and important solvent used in NIBs. For instance, due to its the high dielectric constant (89.78) it can dissolve a sufficient amount of salt. Also, owing to its strong interaction with anions of salts in electrolytes,[150,163] As demonstrated in LIBs, EC can ALSO effectively assist the formation of a rigid protective layer on the surfaces of various electrodes, in NIBs systems, despite the fact that it is not able to behave as a single solvent at ambient temperature due to its high melting point (36°C).[164] Due to its high dielectric constant (64.92) and large liquid range, PC, is another attractive solvent for NIBs.[150] PC is also found to be appropriate for hard carbon in contrast to its unappealing existence, in LIBs, where PC solvent cointercalation causes structural degradation of graphite anodes. Despite this, hard carbon anodes tested in pure PC-based electrolytes show significant capacity fading and poor Coulombic efficiencies, which has been attributed to the continuously developing of SEI.[146,150] in addition to the cyclic carbonate solvents described above linear DMC, DEC, and EMC, are commonly used as binary solvent with EC or PC. Binary solvent systems have a synergistic impact that has resulted in significant changes in ion conductivity, viscosity, electrochemical stability window, and even SIB safety. In 2011, Komaba et. al.[130] tested the hard-carbon electrodes in the binary solvent electrolyte based on EC and linear carbonate esters (EC:DMC (1:1), EC: DEC (1:1) and EC:EMC(1:1) solvent mixtures containing 1M $NaClO_4$).

In this study, EC: DEC solvent showed steady capacity retention over 100 cycles with a high first cycle coulombic efficiency of 78%, whilst the cycle performance of EC:DMC and EC:EMC solvents were deteriorated due to the severe decomposition of DMC and EMC. However, the inclusion of DMC in the electrolyte also shows positive results as it decreases the viscosity and improve the conductivity, as confirmed by Ponrouch et al. who tested the HC electrodes in the binary EC:PC with the addition of DMC.[165]

Table 2.2 Chemical structures and properties of organic solvents used in sodium-ion battery

Solvent	Structure	dielectric constant (ε), 25°C	Viscosity (η), 25°C	AN (DN)	HOMO Value (eV)	LUMO Value (eV)
Ethylene Carbonate (EC)		89.78	1.9	(16.4)	-0.2585	-0.0177
Dimethyl carbonate (DMC)		3.11	0.59	-	-0.2488	-0.0091
Propylene carbonate (PC)		64.92	2.53	18.3	-0.2547	-0.0149
Diethyl carbonate (DEC)		2.805	0.75	(16.0)	-0.2426	-0.0036
2-Methoxyethyl ether (Diglyme)		7.4	1.06	9.9 (19.2)	-0.2133	0.0337
Dimethoxy ethane (monoglyme)		7.18	7.18	10.9 (18.6)	-0.2132	0.0422

2.9.1.3.1 Ether-Based Electrolytes

Glyme-based electrolytes have attracted interest in the field of NIBs due to their ability to enable Na^+-solvent co-intercalation in graphite electrodes and create stable SEI,.[166] Graphite anodes, the most commonly used anode material for LIBs, generally show electrochemical sluggishness for Na^+ion storage because intercalation of Na^+ion into a graphite anode is impractical due to unfavourable thermodynamic parameters. However, as Na^+ ions and ether-based solvent molecules combine to form Na^+ solvated species, they will co-intercalate into a graphite layer, providing impressive capacity, stability, and astonishing reversibility that its Li^+ equivalent never exhibited. This intercalation mechanism is thermodynamically favourable, and the van der Waals interaction between diglyme and graphene strengthens the interlayer binding force, thus stabilising graphite's mechanical integrity. As a result, electrochemical performance of graphite in NIBs is remarkably high, with more than 90% capacity retention and 99.87% Coulombic efficiency after 1000 cycles.[166,167] Furthermore, ether-based electrolytes are difficult to decompose, which leads to minimum SEI film forming on the graphite surface. A recent comparative research by Zhang et al.,[168] demonstrates the effect of carbonate and ether-based electrolytes on the SEI layer formed on the reduced graphine oxide (rGO). The findings showed a much greater reversible capacity and durability in the diglyme-based electrolyte with sodium trifluoromethanesulfonate (NaOTF) than cells cycled in 1 M NaOTF EC/DEC electrolyte. The inferior performance of ester-based solvent was attributed to the high reduction potential where esters started to decompose which ultimately resulted in thicker and unstable SEI.

2.10 Solid Electrolyte Interphase (SEI)

The SEI is a thin protective solid passivation layer, formed at the negative electrode/ electrolyte interface when the Fermi level of the anode material is higher than the lowest unoccupied molecular orbital (LUMO) of the electrolyte. The term "protective" layer refers to the fact that the SEI layer is intended to protect the anode electrode from any chemical reactions that may occur with the electrolyte, as well as to prevent the accumulation of electrochemically active particles and to preserve a uniform chemical composition at the electrodes.[169]This SEI layer, on the other hand, intensifies the internal resistance and consumes some of the positive ions from the cathode or electrolyte, resulting in both power and capacity loss. An efficient SEI should be electronically insulating to prevent any further electrolyte reduction while allowing transport of the charge carrying cations and insoluble and inert in the cell environment. (Li^+, Na^+).[40]Goodenough's model[170] clarified how the SEI operates in LIBs from the perspective

of the energy band. The anode is the reducing agent, the cathode is the oxidant and for a battery chemistry to work, the electrolyte must have a proper energy stable range (E_g), in between LUMO and highest occupied molecular orbital (HOMO) of the electrolyte is the "window" of the electrolyte. E_g should be wide enough to protect the electrochemical potentials of the anode and cathode to prevent the electrolyte decompositions. Thermodynamic stability requires locating the electrode electrochemical potentials μ_A and μ_C (Fermi levels) within the window of the electrolyte. Thus, the anode and cathode must be chosen so that anode μ_A is placed below the LUMO and the cathode μ_C above the HOMO; if not, the electrolyte will reduced on the anode or oxidised on the cathode, resulting in the formation of a SEI film.[136,170,171]

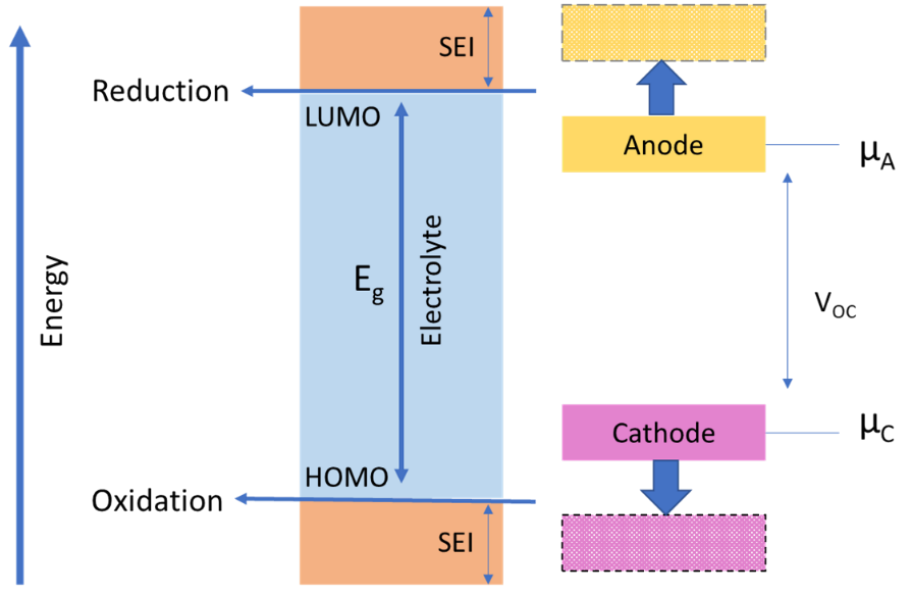


Figure 2.9 Schematic potential limits for the electrolyte stability, and the energy levels of HOMO and LUMO.

This layer consists of organic and inorganic insoluble electrolyte decomposition products that adhere to the anode electrode surface[172] and the understanding of the SEI is complicated and there is no absolute parameter in order to normalize or generalize the composition of the SEI. Its properties, quality, efficiency, ionic conduction, stability, and thickness [173] are dictated by a combination of factors such as the composition of the electrolyte, the analytical conditions or sample preparation procedures.[166] In addition, the formation of unstable SEI film also leads to the low initial coulombic efficiency and it is critical to tailor electrode structure accordingly, optimize the electrode/electrolyte inteface, develop a stable SEI film. For example, it has been shown that fluoride rich SEI contributes to the inhibition of continuous reactions between Na metal and electrolyte. A thick SEI film, on the other hand, can significantly impede the

insertion/desertion of sodium ions during the cycle period, slowing the ion transport speed.[174] Recently, some studies of SEI formation in NIBs have been reported [109,119,150,165,175], yet it is not sufficient to determine with certainty the useful patterns on how to form a stable SEI. Following such previous experience with LIBs, the SEI composition for NIBs has also been studied by numerous techniques (XPS, Time-of-Flight Secondary Ion Mass Spectrometry (TOF-SIMS), Differential Scanning Calorimetry (DSC), High-Resolution Transmission Electron Microscopy (HRTEM), Fourier transform infrared (FTIR)[176]). Yang et al.,[169] used XPS to investigate the various elements of SEI in ester- and ether-based electrolytes, with ether-based electrolytes having more organic components in the SEI, resulting in high stability and thinner SEI in ether electrolytes. On the contrary, according to Bai et al.,[177] as compared to thinner SEI formed in ester electrolyte, a thicker and more robust ether-based SEI film contributes to enhanced cycling stability. They suggested that thin SEI is not beneficial for the cell chemistry as it is found to be not robust enough to support volume adjustments during cycles which resulting in low cycling stability. Therefore, the authors pre-cycled the hard carbon electrode in EC:DEC mixture electrolyte to form a thick and robust ester based SEI, and then moved the pre-cycled electrode to DEGDME based electrolyte. The SEI incorporates the benefits of both electrolytes effectively ensuring outstanding rate performance and long term stability with no significant capacity loss after 1000 cycles. Furthermore, Additives are also realized to be an important component of electrolyte formulation as they are capable of forming compact, uniform, and stable SEIs, thus significantly contributing to the cell cycle life, rate capability, and durability. Komaba et al.,[174] for example, investigated the electrochemical properties of Na/HC cells in a $NaClO_4$-based electrolyte by using fluoroethylene carbonate (FEC), trans-difluoroetyhene carbonate (DFEC), and vinylene carbonate (VC) as an additives. It was discovered that adding 2% FEC by volume to the electrolyte greatly improved the electrochemical reaction, whereas DFEC and VC had little effect. This shows that a reasonable volume of FEC additive improves the formation of a high-quality passivation film on the electrode material's surface, as well as in the prevention of side reactions between Na metal and PC based electrolyte. However, when the DFEC additive is applied, no beneficial effects are observed in the performance. It is worth noting that VC is widely regarded as a suitable additive for modifying the interface in LIBs through the formation of the SEI film; however, the addition of VC additive to PC solvent does not play the same function in NIBs anode. The effect of FEC on sodium cells using the Sb-based negative electrode material was also explored by Darwiche et al.[178] The efficiency of the electrolyte with additional FEC was excellent for

the retention of the capacity (100%), although after 100 cycles only 2% of the original capacity was retained of the FEC-free electrolyte. It can also be noted that the experiments were carried out using a Na metal counter electrode in a half-cell configuration, which has demonstrated a significant effect on efficiency.[39,179,180]

2.11 Hydrothermal carbonization (HTC) for anode materials

During the past few decades the hydrothermal carbonization (HTC) process has attracted much attention due to its environmentally friendly (no need for organic solvents or costly catalysts), low-cost and mild reaction conditions (typically between 40-100 bar, and temperatures ranging between 200-400°C) and CO_2 efficiency.[181,182] HTC is an effective technology for transforming biomass precursors into spherical carbon via dehydration, polymerization and finally carbonization reactions.[183]After further carbonization these carbon spheres have shown interesting electric properties and were used as an anode material for energy storage technologies exhibiting excellent cyclic performance, and capacity.[184,185] It was found that hydrothermal carbons enable uniform charge distribution across particle surfaces and a better packing density in the electrode; because of the low surface area-to-volume ratio it also reduces the degree of the SEI developed in the first cycle.[186,187] Numerous studies have compared hydrothermally treated precursors to directly pyrolyzed biomass and discovered that HTC treated hard carbons have excellent lithium- or sodium storage properties.[76,188,189] Zheng et al. discovered that the increased microporosity introduced by HTC played an important role in the enhanced electrochemical performances as compared to direct pyrolysis of holly leaves and sweet potato.[190,191] Wanget al. reported that in hydrothermally treated peanut skin, the presence of micropores and mesopores has contributed to the increased initial capacity, as a high fraction of mesopore enables faster ion diffusion.[192] Recently, Au *et al.* prepared a series of hard carbons was prepared by hydrothermal carbonisation of glucose and the microstructure of these materials was tuned by varying the pyrolysis temperature between 1000 and 1900 °C to investigate the effect of structural changes on electrochemical performance. The increasing carbonization temperatures decreased interlayer spacings between graphic layers and increased the transition from microporosity into mesoporosity, which reduced the surface area and overall pore volume. The material carbonised at 1500 °C exhibited the highest capacity which was attributed to a balance between structural factors such as interlayer spacings and pore structure. According to Xie and co-workers, not only can the conventional carbon spheres be used as NIB anode material, the precipitate from the HTC autoclave containing carbon dots also exhibits excellent sodium storage performance upon drying and carbonization.[193]HTC process

provides new insights for the design and development of carbon anodes; therefore it has a great importance for future commercialization of NIBs.

3 EXPERIMENTAL

3.1 Characterization Methods of Hard Carbon

3.1.1 Methods for structural characterization

3.1.1.1 Scanning electron microscopy

Scanning electron microscopy (SEM) is a powerful tool for material characterization at a high magnification that scans a focused electron beam over a sample surface to produce an image that is usually on the order of a few μm. SEM measurements reveal information regarding overall structural morphology.[194] It consists of an electron optical column, a vacuum system, electronics, and software. The electrons are generated at the top of the column by the electron source and can penetrate to a depth of a few microns, depending on the accelerating voltage and the density of the sample. As electrons interact with the sample, backscattered (BSE) and secondary electrons (SE) are produced, as well as characteristic X-rays, which are then collected by a detector. The most commonly imaged signals in SEM are SE and BSE. BSEs are reflected back after elastic interactions between the beam and the sample. The BSE signal is used mainly for its strong atomic number contrast. The SE signals, because of the inelastic interactions between the electron beam and the sample, they have very low energies. This gives SE images high spatial resolution and strong topographic contrast, and the SE signals vary with the topography of the sample surface much like an aerial photograph: edges are bright, recesses are dark. In addition to imaging, qualitative and quantitative elemental analysis information can be also obtained using an energy dispersive X-ray spectrometer (EDX) by the analysis of characteristic X-rays. [194,195] Generally, hard carbon powder samples can attach to an aluminium pin stub with double-sided carbon tape. Prior to the analysis, samples are dried to remove any volatile components. For a good quality image of the surface, coating with a thin layer of metal nanoparticles, usually Au or Cr may be required to disperse electrostatic charge accumulation.

3.1.1.2 Transmission electron microscopy

Transmission electron microscopy (TEM) is a technique to look at the atomic features of the carbon structure within the order of a few nm. TEM has three essential systems: the first is an electron gun, which produces the electron beam, and the condenser system, which focuses the beam onto the object; the second is the image-producing system, consisting of the objective

lens, movable specimen stage, and intermediate and projector lenses, which focus the electrons passing through the specimen to form a real, highly magnified image; and the third is the image-recording system, which converts the electron image into some form perceptible to the human eye.[196] The interactions between the electrons and the atoms can be used to investigate features of the lattice such as interlayer spacing, graphene layer stacking and provide a general concept of the structural ordering of hard carbons. Most commonly, images are generated in a bright field image. Thicker areas of the sample appear darker as they scatter or absorb electrons, while the thinner areas transmit electrons and appear brighter. In simple terms the bright field image appears as a shadow of the specimen. In the bright field image, unscattered electron beam is selected and the scattered electrons are excluded from forming the image. The TEM specimen must be very thin so that electrons are able to pass through it. Carbon powder samples are usually prepared by dissolving a small amount of powder in a particular solvent and casting one drop of the solution on a TEM grid before leaving the grid to evaporate the solvent for hours before analysis.

3.1.1.3 Raman spectroscopy

Due to the sensitivity to the local changes in the carbon structure and its high resolution, Raman is a non-destructive and powerful tool for understanding the structural changes taking place on carbon electrodes and investigating the ordering of the carbon-based electrode materials in batteries. A wide variety of carbon structures and different physical properties are directly linked to the ratio of sp^3 and sp^2 bonds.[27,197,198] The Raman spectra of hard carbons are mainly dominated by sp^2 contributions. The degree of disorder in the carbon structure is characterised by the intensity ratio between the G band appearing at ~1580 cm^{-1}, and the D band at ~1350 cm^{-1}, I_D/I_G. The G band is related the relative motion of sp^2 atoms in both rings and chains while the D band is related to the breathing modes of sp^2 carbon atoms in six-membered-rings.[199] Therefore, even for amorphous carbon structures dominated by sp^3 content, the visible Raman spectra are formed due to sp^2 influences. Ferrari [200]stated that in a structure that comprises only six-fold rings, the introduction of sp^3 sites into the structure causes the loss of sp^2 rings and softens the vibrational density. As the strength of the D peak is related with the number of benzene rings in hard carbons, reducing the number of ordered rings causes a decrease in intensity of D peak. It can be said that unlike graphene, in highly amorphous carbons the growth of a D peak shows growth of ordering. Since the G peak is only related with bond stretching of sp^2 pairs, the intensity of the G peak stays constant, and I_D/I_G increasing with increasing structural ordering.[199] For graphite containing carbons the G' band typically

appears at about 2700 cm^{-1}. The G' band is the second order of the D band and so also known as the 2D band. The shape, intensity, and position of the 2D band changes according to the number of graphene layers.[201,202] Raman spectroscopy is a useful technique for the investigation of the structural properties of hard carbon materials for electrochemical applications. *Ex-situ* and *in-situ* Raman are applied to NIBs to elucidate the sodium storage mechanism by revealing the change in structural domains related to sodiation-desodiation and highlighting the role of graphitic and amorphous carbon domains. [203,204]

3.1.1.4 X-ray Photoelectron Spectroscopy

XPS is a technique used to investigate the surface chemistry of solid materials. In XPS measurements, the incident X-ray is shone onto a material surface, which causes the ejection of electrons from atoms at the sample surface. The ejected electron is then captured and analysed for kinetic energy. The kinetic energy of a photoemitted electron is dependent on the binding energy of the electron and is characteristic of the element that electron originated from. Based on the kinetic energy of the captured electron, the binding energy of the electron can be determined. By analysis of the binding energies, it is possible to determine which elements are present on the surface of the sample, elemental composition and the type of bonding structure of the element. XPS is a surface sensitive technique and X-rays manage to probe only a few nm into the surface of the sample. Since the oxygen content on the surface of the carbon material can vary significantly depending on environmental factors, analysis of the carbon materials can be misleading at times. For the specimen preparation for analysis, small amounts of sample are needed. One should be very careful during sample preparation to avoid any contamination which can affect quantification results. In addition, air sensitive samples need to be prepared in inert environment such as glovebox and require inert atmosphere transfer vessel to prevent unwanted surface oxidation reactions from occurring during the sample loading process. This procedure is especially important for the analysis of battery materials that contain lithium, sodium, magnesium or air sensitive catalyst.[205]

3.1.1.5 Gas Adsorption analysis

The textural properties of hard carbons are an influential factor on the electrochemical performance. Gas adsorption measurements are used to determine the overall external porosity, and surface area of the hard carbon materials. Nitrogen (N_2) is typically used to analyse textural properties of hard carbons but complete porosity of the materials with very small pores (smaller than 0.7 nm) cannot be measured by N_2 and for this purpose CO_2 adsorption are considered to be the most suitable.[206] Different gas molecules show different adsorption behaviours, and

some pores may be inaccessible for N_2 but "open" for CO_2.The higher saturation pressure and smaller size of the CO_2 molecule allows it to reach small micropores. The N_2 adsorption measurements are often done at 77 K and the N_2 molecules are moving very slowly at that temperature which limits the access of gas molecules in small pores kinetically. The CO_2 adsorption measurement is conducted at 273 K, and the CO_2 molecules are able to insert in the narrow pores at 273 K. To understand the Na storage mechanism, the influence of small pores is often left unassessed. However, the micropores are crucial to understand the associated storage mechanism. Hence, the porosity of hard carbon should be evaluated by both N_2 and CO_2 gas adsorption. The amount of adsorbed gas molecules on the material's surface with the pressure they were adsorbed is correlated to the porosity and surface area values. The density functional theory (DFT) model and Brunnauer-Emmett-Teller (BET) model are widely used for obtaining porosity, especially for understanding pore size distribution and analysing the surface area of the materials, respectively. Pores are classified and defined by IUPAC by their sizes: micropores are smaller than 2 nm in diameter, mesopores are between 2 nm and 50 nm and macropores are larger than 50 nm in diameter.

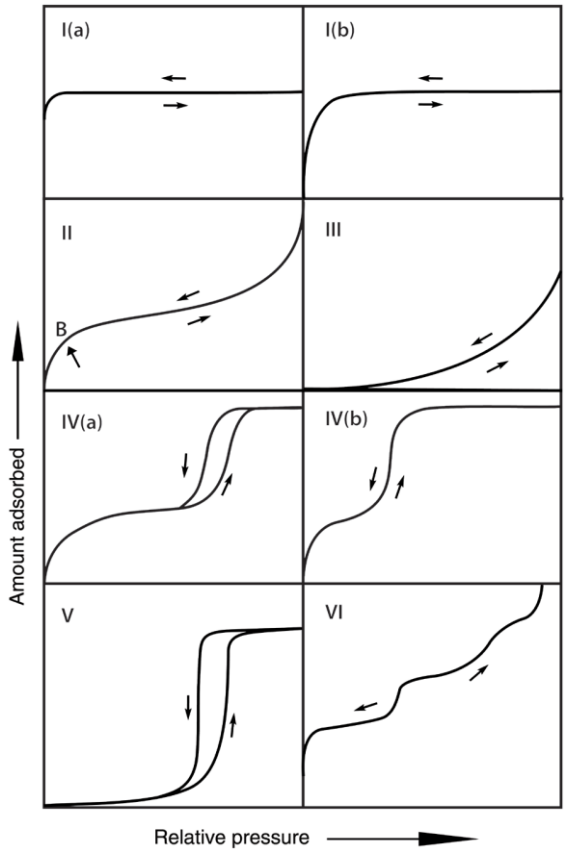


Figure 3.1. Classification of gas adsorption isotherms. (I) Microporous materials. (II) Non-porous materials with strong gas interactions (III) Non-porous materials with weak gas interactions (IV) Mesoporous materials. (V) Porous materials with weak interactions with the gas. (VI) Homogeneous surface materials.[207]

Characteristic shapes of isotherms show the types of specific pore structures that exist in a material. Classifications of gas adsorption isotherms and hysteresis loops are shown in *Figure 3.1*.[208] Typical carbon materials usually show three main isotherms. Type I isotherms show large volumes of gas absorptions at very low pressures and are related to microporous materials. A type III shape, which is specific to nonporous or macroporous materials, implies weaker interaction between adsorbed molecules than adsorbent surface-adsorbate interactions. Typical mesoporous materials show the type IV isotherm that have a hysteresis between the adsorption and desorption curves at higher pressures and the gas separates from the material at a lower pressure than it entered.

3.1.1.6 Small and Wide-angle X-Ray Spectroscopy

A synchrotron is an extremely powerful X-ray source. The X-rays are produced by high energy electrons as they circulate around the synchrotron. In more detail, the synchrotron radiation source is a circular particle accelerator where electrons are accelerated to extremely high energy by magnetic field and then changed direction periodically. The resulting X-rays are emitted as dozens of thin beams, each directed toward a beamline next to the accelerator. The high intensity X-rays existing at a synchrotron provide two main advantages over lab-based instruments. Firstly, the greater X-ray intensity provides a greater separation between the sample and the detector during measurements, which allows access to a much wider range of length scales. Secondly, the high intensity of the X-rays at a synchrotron allows structural investigation of non-crystalline materials such as amorphous carbons in much faster measurement intervals.

Small Angle X-ray Scattering (SAXS) is a technique mainly applied for the structural investigation of partially ordered materials that are either difficult or impossible to crystallise. SAXS provides information about larger scale bulk microstructure within a sample, usually in the size range from approximately ~1nm up to around 300nm. Wide Angle X-ray Scattering (WAXS) is a technique used for the investigation of partially ordered materials as well. WAXS, analogous to powder diffraction, gives information about crystallisation and can be measured simultaneously with SAXS. Small angle scattering covers the angular range up to 1° while WAXS typically covers 5 - 60°.

Recently, hard carbon studies for NIBs include numerous studies involving SAXS analysis.[74,209–211] Due to the amorphous nature of the hard carbons, X-rays will be scattered in many directions that cause wide range 2 theta peaks and a raised background at low angle in XRD measurements. In order to examine low angle scattering suitably, a specially designed

geometry is required that must be extended toward low angles. In SAXS technique three types of slits are used to define the geometric X-ray beam, this geometry would allow the beam spread across the 2D detector in one direction.[212] A vacuum tube is fixed on the monochromator to reduce the air absorption and intensity loss from the scattering. [213] A typical SAXS instrument setup is shown below Figure 3.2. The typical SAXS pattern obtained for hard carbon after integration of the 2D detector image is represented in Figure 3.2 as a function of the scattering vector (Q), together with a schematic representation of the microstructure of a hard carbon at various scales. As can be seen in Figure 3.2, the larger the size of the morphological features such as pores and particles [117,214,215] are related to the smaller Q values, whilst the microstructural and molecular scale observations can be made at intermediate[117,214,216] and high Q ranges, respectively.

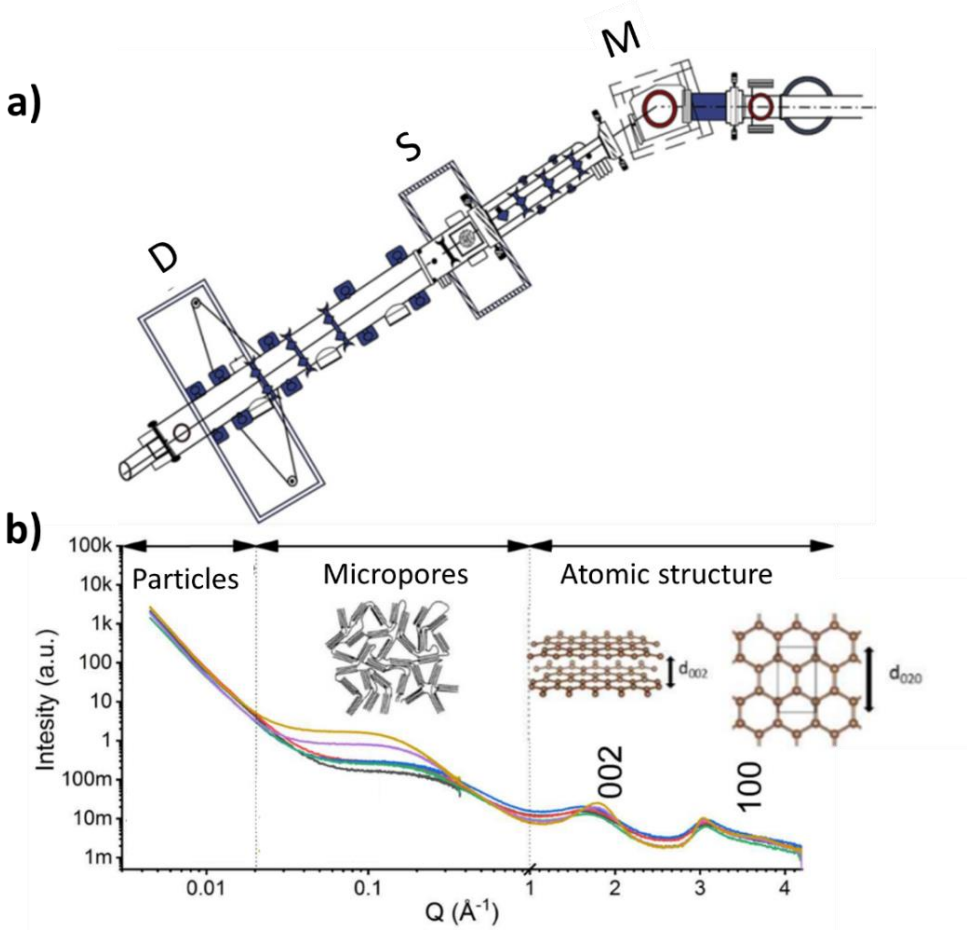


Figure 3.2 a) A typical SAXS instrument setup including monochromator (M), sample holder (S), and detector plane (D).[213] *b) A typical SAXS pattern; intensity versus scattering vector curve in log-log scale*

SAXS allows the measurement of total porosity (open porosity and internal-closed porosity) [27,104,217]this feature makes it powerful complementary analysis to gas adsorption techniques.

As gas adsorption only probes the pores approximately equal to or larger than 0.4 nm,[218] it is used for "open pores" analysis (in interaction with the external environment) rather than "closed pores" (internal pores, inaccessible to gas molecules but accessible to Na^+ ions). The closed pores are significant to understand, as they have a strong effect on the sodium storage performance in hard carbons at low potentials.[219,220]

3.1.1.7 Total Neutron Scattering/ Pair distribution function

Total scattering is the measurement of the complete diffraction pattern, including both the Bragg and diffuse components. It is a technique to reveal structural information (bond coordination, defect concentration etc.) about short and mid-range order of crystallographically challenged materials like amorphous carbons. From the Bragg peaks in an X-ray diffractogram the long-range order of the atoms can be deduced. The short-range order, i.e. the local atomic structure, is present in the broad, less well- defined features in the diffractogram. This local structure is described quantitatively by the atomic pair distribution function (PDF). The pair distribution function technique is also known as total scattering analysis which describes the probability of finding two atoms separated by a certain distance in the material under investigation. The PDF, denoted as G(r), is the Fourier transform of the normalized reduced total scattering structure function, uses the total scattering data acquired at high Q-values.

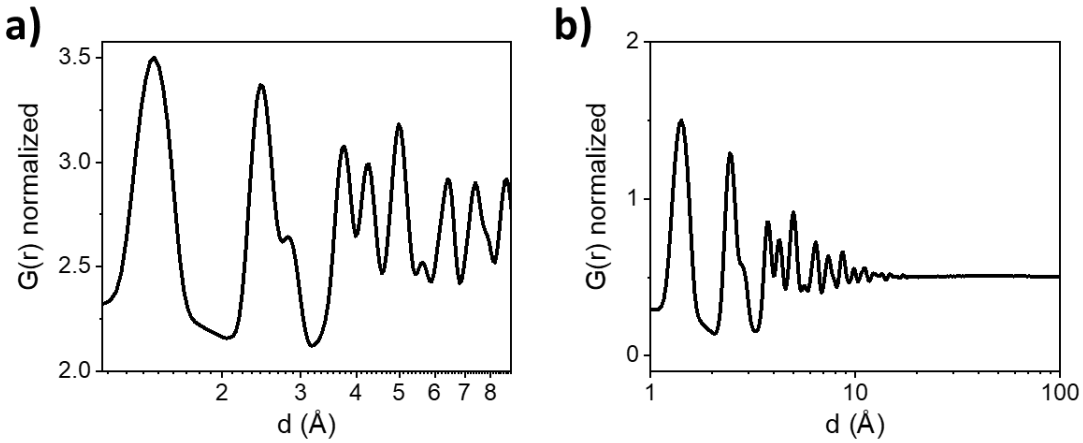


Figure 3.3 PDF patterns of pristine hard carbon with a) short and b)long distances

There are three key points to keep in mind when analysing the PDF results of amorphous carbon materials. The first one is the peak observed at 3.35 Å, which is used to distinguish amorphous carbon from graphite (Figure 3.3). The presence of this shoulder peak at 3.35 Å represents the interlayer spacing of graphite and ABAB stacking. [221]Therefore, the graphitic structure consisting of ABAB stacking is evidenced by this peak, while this peak does not appear in amorphous carbon analysis. The second point is the overall peak intensity. PDF plots with

higher peak intensities suggest a structure that has lower defect/vacancy concentration than plots with lower peak intensities. This comparison can only be used between two materials that are analysed under the same conditions. Last point is the measurement of the lateral order in the AB direction in the G(r) plot. A material with a short-range layout like amorphous carbon, will show reduced peak intensities at higher distances (Figure 3.3b), while long range order materials like graphite exhibits consistent peak intensities at the same high distances which indicates a longer coherence length.

3.1.1.8 Electrochemical Dilatometry

During ion insertion into the anode or the cathode materials, the structure undergoes a volume change due to the crystal expansion. When a battery undergoes a colossal volume changes during ion insertion and extraction processes, this leads to pulverization of the active materials of electrodes as well as losing electrical contact with the collector. Considering practical battery applications, monitoring and controlling change of the electrodes during electrochemical cycling is very beneficial for designing batteries with minimum overall volume changes. In situ electrochemical dilatometry (ECD) is a very useful method to monitor the dynamics of electrodes during cycling (Figure 3.4). This technique has been performed on graphite half cells,[222,223] Si composite half and full cells,[222] SiO half cells[224] as well as hard carbon half cells.[225] In-situ AFM and XRD has also been used to follow expansion and contraction of electrodes during electrochemical cycling.[226–229] Since XRD provides information on crystalline phases to calculate the volume changes of the active material, these techniques have some drawbacks on understanding behaviour of poorly crystalline materials such as hard carbons. ECD has advantage over these two techniques, for instance: unlike graphite with its almost flat graphene layers, hard carbons with disordered structure generally have larger particle size that makes it unsuitable for also AFM measurements. ECD has also been very useful to follow charge storage mechanisms in electrodes. Ion insertion processes can be observed with the change of electrode thickness at different cell voltages. Comparing hard carbon and graphite electrode expansion during sodiation shows that the volume change in hard carbons is much smaller. This small volume change is due to the hard carbon's wider interlayer spacing and large pores and is also an indication of electrode stability during cycling.

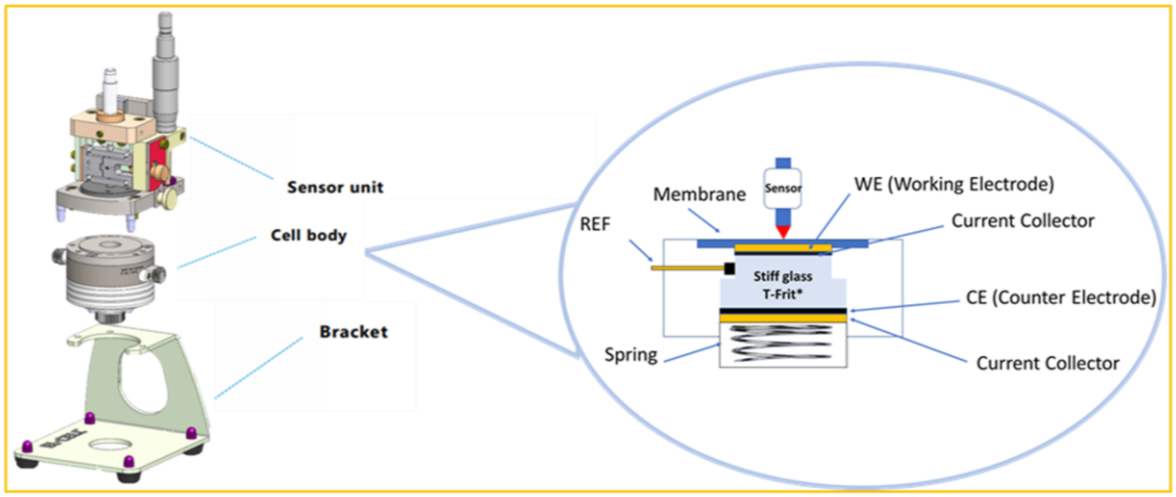


Figure 3.4 Basic setup of the Electrochemical Dilatometry[230]*, E-cell placed in the dilatometer frame *The glass frit is fixed in position, therefore only the thickness change in the working electrode is recorded.*

3.1.2 Methods for electrochemical characterization

3.1.2.1 Potentiostatic Cycling

Cyclic voltammetry (CV) is an electrochemical measurement technique, which can be used to investigate the electrochemical behaviour of an electrode within a certain potential range.[231] In this technique, the potential of the working electrode is varied between two limits in steps (at a specific scan rate) as a function of time, while the current responses are recorded. Information related to the system`s thermodynamics of redox reactions, kinetics of electron-transfer reactions and charge separation can be obtained by cyclic voltammetry measurement.[232] During this technique, the current is plotted versus the potential and the resulting curve shape which is defined by the kinetics of the physical and chemical reactions taking place within the potential range plays important role as a fingerprint for the electrochemical properties of a redox system (Figure 3.5).[231] For example, distinctive peaks in a voltammogram curve indicate kinetically slow faradic reactions occurring within the electrode material.

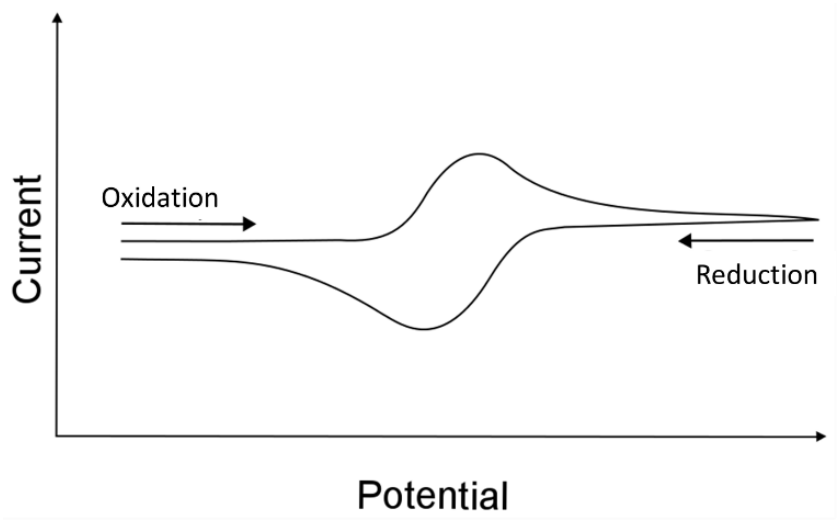


Figure 3.5 Schematic representation of voltammogram

3.1.2.2 Galvanostatic Cycling with Potential Limitation

This test is performed with a constant current source where the maximum potential is reached, then followed by application of an equal magnitude discharge current to a minimum potential. The potential is measured as a function of time. Total capacity can be measured by galvanostatic cycling between two fixed potentials and it is usually indicated in terms of mAh/g. For a battery, the experimental specific capacity, $C_{ex,sp}$ can be calculated from the galvanostatic test using the following Equation 3-1 given below.

$$C_{ex,sp} = \frac{I\,\Delta t}{3600m} \qquad \text{Equation 3-1}$$

where I (A) is the applied current, Δt (s) is the discharge time and m (g) is the active material weight. Obtained $C_{ex,sp}$ value is usually used to decide whether an anode material is good or not compared theoretical capacity . The gravimetric energy density, Esp battery, is calculated using $C_{ex,sp}$ in Equation 3-2.

$$E_{sp} = \Delta V\, C_{ex,sp} \qquad \text{Equation 3-2}$$

where ΔV is the voltage window. The obtained plot of galvanostatic charge/discharge provides information on several electrochemical processes happening with the material.

3.2 Electrode materials and electrolytes

3.2.1 Glucose-Citric acid temperature series

Hard carbon materials used in this research were prepared from glucose in two steps that consist of HTC at low temperature and carbonization at high temperature.[184] In the first stage, 10 g glucose (D-(+)-glucose, ≥99.5%, Sigma Aldrich) was dissolved in 90 mL deionised water and the pH adjusted to 1-2 by the addition of 3.6 g citric acid (≥99.5%, Sigma Aldrich). The

solution was placed in a Teflon container, then inside a stainless-steel autoclave vessel and heated at 230ºC for 12h then dried at 80 ºC overnight. In the second stage, the resulting material was pyrolyzed under continuous nitrogen gas flow in a tube furnace. Pyrolysis was conducted at 1000ºC, 1300ºC, 1500ºC, 1700ºC and 1900 ºC. The resulting hard carbon samples are denoted GC1000, GC1300, GC1500, GC1700, and GC1900.

3.2.2 Soft Templated carbons

Mesoporous carbon materials were synthesized by soft templating of carbon precursors with a soft block copolymer and subsequent solvothermal carbonization at moderate temperatures around under self-generated pressure. Biomass precursor phloroglucinol (1,3,5-benzentriol, C6H6O3), Triblock copolymer Pluronic F127 (poly(ethylene oxide)-block– poly(propylene oxide)-block–poly(ethylene oxide, PEO106PPO70-PEO106) as template and glyoxylic acid, which has bi-functionality (aldehyde and carboxylic acid groups) not only behave like a cross-linker for the formation of the resin but also has the role of a catalyst by creation of H-bonding between the precursors, and absolute ethanol (C_2H_6O) were added to the reaction mixture. All chemicals were purchased from Sigma-Aldrich and used as received. In a typical experiment, 0.82 g phloroglucinol and 0.61 g glyoxylic acid monohydrate was mixed with 1.61 g Pluronic F127 and dissolved under stirring at room temperature in absolute 40 ml ethanol. The obtained clear solution was prepared in glass inlets was transferred into Teflon inlets, which then again were placed in stainless steel autoclaves (Parr Instruments). After that, hydrothermal treatment was carried out at 80 °C for 4 h and subsequent 200 °C for 12 h was performed to cross-link the phenolic resin framework. The obtained materials were exposed to further heat treatment for drying and carbonised in a high temperature oven under inert N_2-atmosphere. For this purpose, the dried materials were placed in ceramic crucibles, put in the high temperature oven. The pyrolysis was done at 1000 ºC, 1300 ºC , and 1500 ºC with a heating rate of 5 ºC $min^{-1}$with a dwell time 2 h. After the carbonisation, samples were allowed to cool down to room temperature.

3.2.3 $Na_3V_2(PO_4)_2F_3$ /C cathode

The $Na_3V_2(PO_4)_2F_3$ /C (NVPF/C) sample was synthesized via a simple hydrothermal method.[233] Apart from carbon black, all of the chemicals used to synthesize NVPF/C cathode materials were purchased from Sigma-Aldrich. A typical synthesis is as follows: 0.98g V_2O_5 and 0.337g oxalic acid were added into 15 mL deionized water under continuous magnetic stirring at 70 °C for 20 min. Subsequently 0.252 g $NH_4H_2PO_4$, 0.130 g NaF and 0.03 g carbon black (Super P conductive, 99+%, Alfa Aesar) were added into the blue solution under stirring.

The obtained mixture was transferred to 50 mL Teflon inlets, which then again were placed in stainless steel autoclaves and kept in an electrical oven at 180 °C for 12 h. After it cooled down to the room temperature the obtained gel was dried by a freeze dryer overnight, the as-prepared product was annealed in N_2 at 475 °C for 9 h with a heating rate of 5°C min^{-1}, and the NVPF/C material was synthesized.

3.3 Structural and Physical Characterization Method

The morphology and structure of the as-prepared samples were characterized by Scanning electron microscopy (SEM) using a FEI Inspect-F SEM at 10 kV. For cross section measurements of GC1300, samples after cycling were washed with dimethyl carbonate and dried at 25 °C under vacuum overnight. electrodes were cut by scalpel. Transferring time for air sensitive sodiated samples was 60 s at maximum. The nanostructure of the samples was investigated using a JEOL 2100Plus TEM at 200 kV operating voltage. Raman spectra were measured using a Renishaw in Via Raman instrument with a laser wavelength of 633 nm. . Small/wide angle X-ray scattering (SAXS/WAXS) was measured on a Xenocs nano-InXider with a Cu-kα source and a two-detector setup for combined SAXS/WAXS measurements. Powder samples were packed in 2 mm Kapton capillaries and measured for 10 min, the empty capillary was measured separately and used for background subtraction. Neutron total scattering experiments were performed at the NIMROD[234] instrument at ISIS (Harwell, UK), each sample was contained in a thin-walled Vanadium flat plate cell measured for 2 hours using a 30×30mm beam. The data were normalised using a 3mm VNb null scattering plate and scattering from the empty cell and instrument subtracted. The PDF and S(Q) were calculated using the Gudrun programme, both functions were normalised to absolute scale and corrected for beam attenuation, multiple-scattering and inelasticity effects.[235,236] SAXS/WAXS and Neutron total scattering measurements and data analysis were made possible through the help of Anders C.S. Jensen, the measurements were conducted at ISIS Pulsed Neutron and Muon Source, Rutherford Appleton Laboratory. The textural properties of the GCs were determined from the adsorption isotherms of N_2 at 77 K and CO_2 at 273 K using Autosorb iQ-C (Quantachrome Instruments, USA) instrument. The specific surface areas were calculated by Brunauer-Emmett-Teller (BET) method for N_2 or Dubinin-Radushkevich (DR) method for CO_2. The BET surface area (S_{BET}) was calculated in the relative pressure range of 0.05–0.3 for N_2 adsorption. The pore size distribution (PSD) was calculated using a non-local density functional theory (NLDFT) method for slit pores adapted for these materials. Before the gas adsorption analysis samples were degassed overnight under vacuum at 200 °C. The surface

chemistry and electronic structure were characterized using a Thermo Fisher Scientific K-Alpha+, after drying the samples at 120ºC overnight. XPS system equipped with Al (Kα) source operating at 2×10^{-9} mbar base pressure at ambient temperature. Atomic compositions were obtained from the averaged spectra taken from 3 areas for each sample. For *ex-situ* measurements, after the cell disassembly, the recovered electrodes were carefully washed several times with a related solvent, namely DMC and Diglyme. Then the washed electrodes were dried 6 hours to fully evaporate the solvent and then transferred to the vacuum container. Argon sputtering for the XPS depth-profiling was carried out using ion beam energies of 500 eV. The etch rate rate calibrated on Tantalum pentoxide (Ta_2O_5) surface was ~ 0.05 nm/s. The quantitative analyses were performed using Casa XPS software. The binding energies were corrected to the C 1s peak position at 284.8 eV originating from surface hydrocarbons.

3.4 Electrode Preparation and Cell Assembly

3.4.1 Electrode Preparation

3.4.2 Cell Assembly

All the electrochemical cell performance measurements have been evaluated using CR2032 coin-type cells (MTI corporation). The CR2032 coin cell cases are 20 mm in diameter and 3.2 mm in thickness. The cell preparation was conducted in an argon-filled glovebox. To assemble the cell, a carbon anode is placed in the bottom case (Figure 3.6) with carbon side up. Then a glass fibre separator saturated with electrolyte is put on top of electrolyte. After that, a sodium metal sheet was placed on the separator and a spacer was placed on top. Finally, a spring is put on top of the spacer followed by the top case. The coin cell is closed using a compact crimping machine.

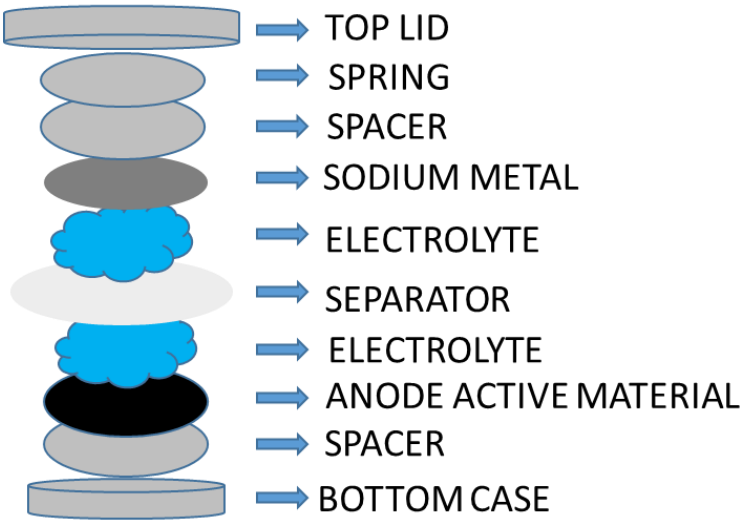


Figure 3.6 Scheme of coin cell assembly.

3.5 Electrochemical Measurements

In electrochemistry, an electrochemical cell consists of two half-cells, and a half-cell is a structure that consists of a conductive electrode and a surrounding electrolyte. The reason why the half-cell configuration is preferred in laboratory scale research is that we can focus only on the electrode of interest. In a sodium ion half-cell, it is common to only have one working electrode, against sodium metal foil. The underlying principle is to remove the uncertainty triggered by electrochemical cycling of the cell with two working electrodes. However, use of sodium metal in a half-cell configuration can lead to poor electrochemical performances than it is expected. It has been shown that the presence of a sodium metal electrode in a half cell causes quicker degradation of the electrolyte and therefore e decreases in capacity and cycling efficiency. Thus, if someone wants to draw conclusion about how a material will perform in real life application, the testing should be done in a full cell as it reflects the conditions as close as encountered in real life. Hard carbon materials coated on current collector were used as working electrode, and electrodes are prepared in the same way for all electrochemical measurements. Electrodes were made using an 85:5:10 weight ratio of active material, carbon black (Super P conductive, 99+%, Alfa Aesar), and carboxymethyl cellulose binder (CMC) (Mw~250,000, Sigma Aldrich), respectively. The obtained slurry was coated in a 250 µm layer on Al foil (conductive carbon coated, 18 µm, MTI corporation) by doctor blade and dried at room temperature for 24h and then at 100˚C for 2 h under vacuum. The foils were cut to a given diameter (usually 13 mm diameter) with a punchcutter. The electrolyte and half-cell preparation were conducted in an argon-filled glove box with $H_2O < 0.5$ ppm, $O_2 < 0.5$ ppm.

The CR2032 coin cells were assembled with a sodium metal disc (1 mm thick, sodium ingot, 99.8% metals basis, Alfa Aesar) as a counter electrode (CE), and a hard carbon anode as the working electrode (WE). The loading of electrode active materials on current collector was ranging from 2.5-5 mg/cm^2. Whatman GF/B glass microfibre was used as a separator. A 1 M electrolyte solutions containing predried (80 °C overnight) sodium hexafluorophosphate ($NaPF_6$ Alfa Aesar, 99+%) and sodium perchlorate ($NaClO_4$ Alfa Aesar, anhydrous, ACS, 98.0-102.0%) in pre-dried (in 4 Å porous molecular sieves, overnight) 1:1 volume mixture of ethylene carbonate (EC, anhydrous 99%, Sigma Aldrich), dimethyl carbonate (DMC, 99.9+%, Sigma Aldrich), diglyme (2-methoxyethyl ether, anhydrous, 99.5% Sigma Aldrich) was prepared by stirring until fully dissolved. For full cell assembly, the NVPF/C material was sodiated (discharged) in 1 M $NaClO_4$ in EC:DMC with a sodium metal disc as a counter electrode to make sure there is enough sodium content for the following full cell configuration. The NVPF/C was subsequently washed with DMC and then were paired with hard carbon in 1 M $NaClO_4$ in EC:DMC. Galvanostatic cycling tests were performed on a Land system in the potential range of 0.001-2.5 V vs Na+/Na for half-cell and between 1.75 and 4 V for full cell configuration. Sodiation/desodiation current rate was 30 mA/ g. which corresponds to a cycling rate of C/10. Cyclic voltammetry was performed on a Biologic VSP-300 potentiostat at a scan rate of 0.1 mV s^{-1}. Electrochemical dilatometry (ECD-3-nano cell by EL-CELL GmbH) was employed to study the electrode dynamics during cycling. ECD-nano cells are designed in a way that only quantifies the dilation of the working electrode in one dimension by the help of a sensor during the electrochemical cycling. The tests were performed in a three electrode-cell configuration having 10 mm diameter of electrode (here hard carbon, the loading of electrode active materials on current collector was ranging from 2-4.5 mg/cm^2) as the working electrode and of sodium metal as the counter (12 mm diameter) and reference electrodes. A special ceramic porous separator, which was soaked in 400µL of electrolyte to wet the electrode, was fixed in position between a metal frame and the spring. Therefore, only the dilatation of the electrode was recorded. The cells were cycled galvanostatically at 10 mA/ g at constant temperature (25°C) in a chamber.

3.6 Computational Methods

All the computational calculations were made possible through the help of Emilia Olsson. Special thanks to Emilia for helping to enhance and support the experimental studies with this section. For the atomic scale simulations of Na storage on defective graphene surfaces and in graphitic stacks with different interlayer distances, all calculations were conducted using

density functional theory (DFT) as implemented in the Vienna Ab initio Simulation Package (VASP, version 5.3.5).[237–240] To simulate sodium storage and migration in the planar graphitic layers with varying interlayer distance, a 4×4×2 supercell (64 atoms) was constructed, whereby up to eight sodium was added to each cell in between the two planar graphitic layers. The two planar graphitic layers were placed in an AB stacking mode, whilst varying the interlayer distance (d_{002} according to experimental characterisation). For the calculations of sodium on defective graphitic surfaces, we used graphene to simulate the hard carbon basal plane. Based on previous experience of modelling this kind of systems, an 8 × 8 supercell (without defects 72 carbon atoms) with a converged vacuum gap of 15 Å was used.[241] All calculations used the projector-augmented wave method (PAW) to describe the ion-electron interaction.[242] The plane wave cut-off and k-space integrals were chosen so that the total energy was converged to 1 meV/atom. The kinetic energy cut-off was 800 eV, with a 5×5×2 Γ-centred Monkhorst-Pack grid to sample the Brillouin zone for the graphitic systems and a 9×9×1 Γ-centred Monkhorst-Pack grid for the graphene models.[243] To express the interacting electron exchange-correlation energy, the generalized gradient approximation (GGA) with Perdew-Burke-Ernzerhof (PBE) [244,245] functionals were used (with electronic convergence criteria of 10^{-5} eV and ionic convergence criteria of 10^{-3} eV·Å^{-1}). All calculations were performed spin-polarized and are periodic. Due to the large polarizability of the graphite and sodium, it is necessary to include dispersion corrections to accurately estimate the metal adsorption and binding energies, in addition to the graphitic interlayer binding energy. [246,247] Here, the DFT-D3 method with Becke-Johnson damping by Grimme and co-workers was selected. [248,249]

4 INVESTIGATION OF SODIUM-ION STORAGE MECHANISM IN HARD CARBON ELECTRODE

4.1 Introductions

The effect of the pyrolysis temperature on the structural evolution, electrochemical performance and storage mechanism of hard carbons has been extensively investigated.[76,121,250]As a common trend, simultaneous decrease in surface area and the number of defects in hard carbon, and an increased degree of graphitization were observed with an increase in heat treatment temperature. All these morphological differences also create different electrode architecture and dynamics, which have considerable influence on sodium ion storage mechanism and the electrode's behaviour during battery cycling. Despite reports of numerous promising hard carbon materials, discrepancies in the understanding of the sodium storage mechanism still exist.[130,251]In order to investigate the dynamic behaviour of the batteries, several *in- situ* and *ex-situ* techniques have already been applied successfully, either at the cell, electrode or material level during the electrochemical cycling. The different mechanisms found in the literature may result from comparing carbon materials from different origins. Besides the type of materials, the applied experimental conditions and the characterization techniques used, and differences in detailed chemistry, especially heteroatomic doping, may be the cause of different conclusions. In this chapter, a series of hard carbons were synthesised via hydrothermal treatment of glucose with citric acid as a catalyst (GCs) which were further carbonized at different temperatures with the aim of identifying the effect of different carbon structural features such as pores, functional groups, interlayer spacing on the Na storage performance. These features can be modulated and controlled by changing the carbonisation temperature during the pyrolysis step of glucose-derived carbon spheres. As expected the resulting hard carbons exhibited a variety of textures and structures, all furthermore showing different electrode architectures with different degrees of surface functionality and defects, porosity and distinct electrochemical behaviour and Coulombic efficiencies. With the support of experimental and theoretical studies, modified structures were used to investigate the effect of hard carbon structure on the sodium storage mechanism. A fundamental understanding of the hard carbon morphology and the sodium storage mechanisms is essential for efficiently designed hard carbon materials for high capacity and high-efficiency NIBs.

4.2 Results and Discussion

4.2.1 Structural characterisations

The SEM micrographs (Figure 4.1) show that the GCs have a spherical shape with a relatively narrow particle size distribution, ranging from 5 to 8 µm. The coating process for electrode preparation did not change the GCs` material morphology and no change was observed in the particle size (Figure 4.1).

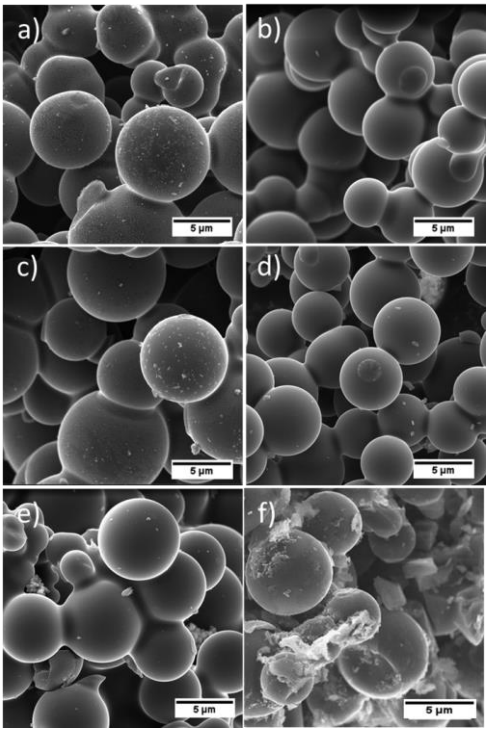


Figure 4.1 SEM images of a) GC1000 b) GC1300 c) GC1500 d) GC1700 e) GC1900 and f) GC1300 electrode (with binder)

Small angle neutron scattering (SANS) and small angle X-ray scattering (SAXS)[129] were used to determine pore sizes. The pore size was modelled using a Guinier-Porod equation.[129] SANS (Figure 4.3) and SAXS (Appendix I, Figure 1. 1) data show a Guinier plateau at around 0.1 $Å^{-1}$, indicating dilute nanopores of random size and shape (Appendix I, Figure 1. 1g). From this, the average pore size was determined (Figure 4.3) and showed a small increase from 1.5 to 2 nm between 1000 ºC to 1500 ºC, followed by a sharper increase to 3.3 nm at 1900 ºC. The pore size was also characterized by N_2 and CO_2 gas adsorption (Figure 4.2). The N_2 adsorption showed low surface area below 11 m^2/g for all samples Table 4.1), suggesting that there is little to no open porosity. All the GCs materials except GC1000 exhibit a type V-shape, specific to mesoporous materials and implying stronger interaction between adsorbed molecules than adsorbent surface-adsorbate interactions. Hysteresis loop classification helps to understand the specifics of the texture of the adsorbent. Isotherms of GC1300, GC1500 and GC1700 exhibit

a type H4 hysteresis loop often attributed to very narrow slit pores or bottle shaped pores. GC1900 shows type H3 hysteresis loop which is an indication of plate like particles that create slit like pores or wide capillaries.

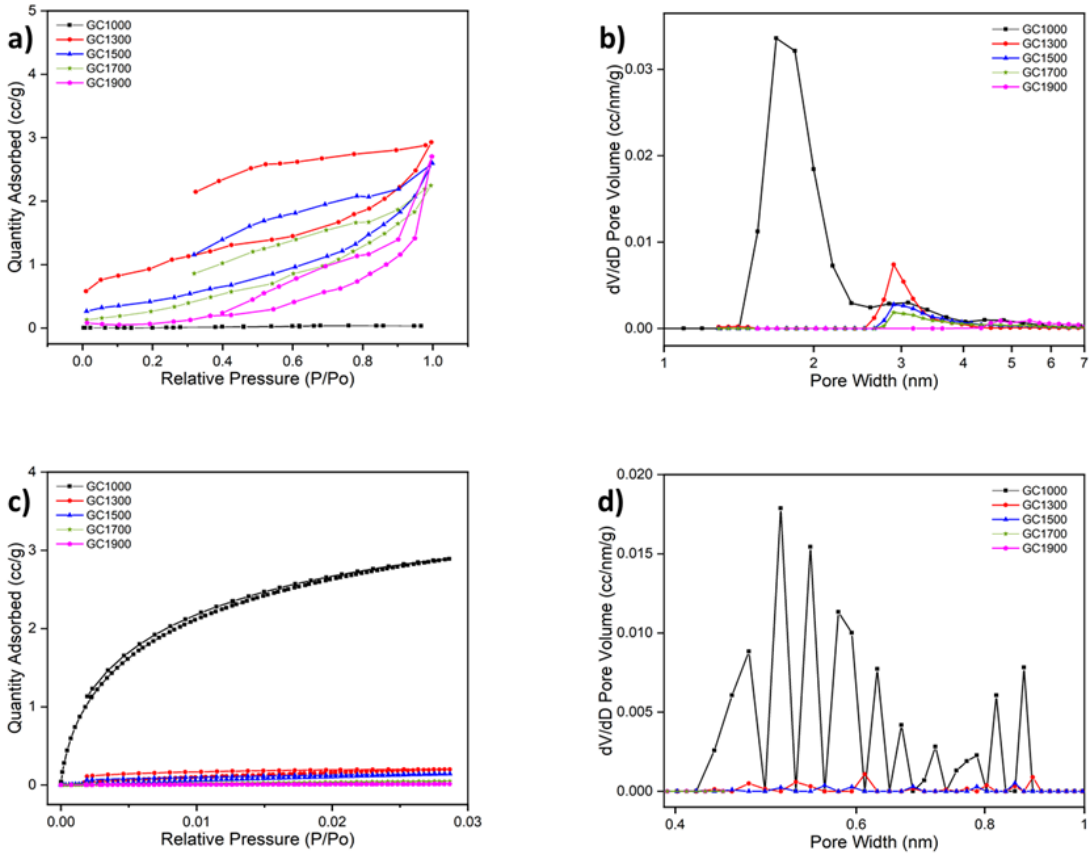


Figure 4.2 N_2 adsorption a) Isotherms b) Pore size distribution and CO_2 adsorption c) Isotherms d) Pore Size Distribution.

The CO_2 gas adsorption showed a much higher surface area ranging from 496 to 2.5m^2/g and a pore size range of 0.5-0.8 nm for all samples (Figure 4.2 and Table 4.1), significantly smaller than the pore sizes obtained from SAXS/SANS analysis (Figure 4.3). The CO_2 adsorption surface area furthermore decreases with increasing temperature to just 2.6 m^2/g for the high-temperature sample (GC1900). In SAXS, change in surface area can be analysed by the Guinier-Porod region[129] (Figure 4.3) which is proportional to the surface area of the nanopores. The intensity of the nano-pore feature in the SAXS/SANS measurements show a minor decrease with temperature suggesting that the pore-density remain largely constant (Appendix I, Figure 1. 1). This suggests that the gas adsorption measurements (Table 4.1) are either probing a surface structure which is removed at higher temperatures or the internal pores

become more closed with increasing temperature as closed pores can be formed that are not accessible for gas probing but can be measured by X-ray and neutron scattering.

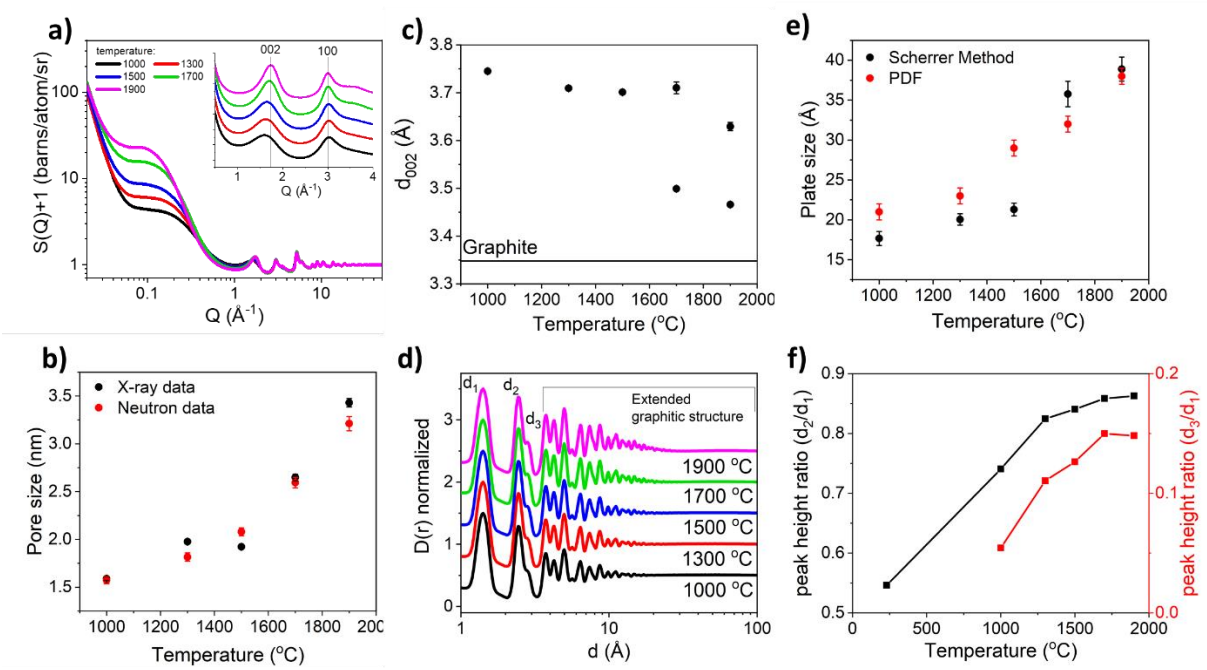


Figure 4.3. a) Structure factor (The Guinier-Porod region showing scattering of the nanopores (Q<1 Å-1) and scattering from the atomic structure at higher Q) and b) mean pore size determined from the Guinier-Porod region of the SANS and SAXS data c) interlayer spacing of the graphitic d) planes pair distribution functions (PDF) of the GCs with the PDF normalized to the height of the first peak at 1.5 Å e) size of the basal plane determined using the Scherrer method and the PDF, and f) peak height ratio of the first three peak observed in the PDF (Figure 4.3d)

A graphitic local structure with turbostratic stacking of the basal plane is observed in the neutron total scattering (Figure 4.3) and WAXS measurements (Appendix I, Figure 1. 1). The data show the characteristic peaks from the plane of the (002) and (100) reflection at 1.8 and 3 $Å^{-1}$, respectively. The interlayer distances (d_{002}) (Figure 4.3c) are well above the limit where sodium intercalation in graphitic layers is energetically favourable.[74,241]At higher temperatures the 002 peak shifts to shorter distances and the peak shape becomes asymmetrical, requiring a two peak model to achieve a decent fit (Appendix I, Figure 1. 1e). This suggests that as the graphitic domains develop, some domains are not able to grow along the *c*-axis likely due to steric constraint. Therefore, a formation of two distinct populations in interlayer distance (Figure 4.3) are observed in the higher temperature materials. The mean size of the graphitic domains was determined by the Scherrer equation using the width of peak from the plane of the (100) reflection (Figure 4.3a) and directly from the pair distribution functions (PDF) (Figure 4.3d). Both techniques showed an increased domain size from ~2 nm at 1000 ºC to ~4 nm at 1900 ºC (Figure 4.3e), which is an indication of structural ordering. The increase in the graphitic domain size is associated with a simultaneous increase in the pore size,

suggesting that the dimensions of the pores are determined by the size of the graphitic domains. The TEM images (Figure 4.4) show that all samples have typically disordered carbon structures, although more organised regions with longer graphitic domains appear with the increase of the carbonisation temperature. Due to the presence of strong crosslinks formed during HTC, even at 1900°C, the material still shows the characteristics of hard carbon as the temperature was not sufficient to transform the structure to a highly ordered graphitic morphology. To further study the structural changes with carbonization temperature, Raman spectroscopy was conducted, and the results are shown in Figure 4.4f, and Table 4.1.The Raman spectroscopy of the GC series shows that the D and G bands sharpen and become narrower with increasing carbonization temperature, which indicates the development of aromatic six-membered rings. The increase in I_D/I_G suggests the decrease in concentration of defects along the graphene sheets at higher carbonization temperatures.[252] Moreover, the L_a is calculated from the I_D/I_G ratio and shows an increase in the crystallite length and coherence, and therefore a higher degree of graphitic order.[199,200]Furthermore, the appearance of the 2D peak at 1700 and 1900°C implies the presence of larger domains of graphitic ordering, consistent with the neutron total scattering and SAXS/WAXS results and observations made by TEM.[199,200,253]

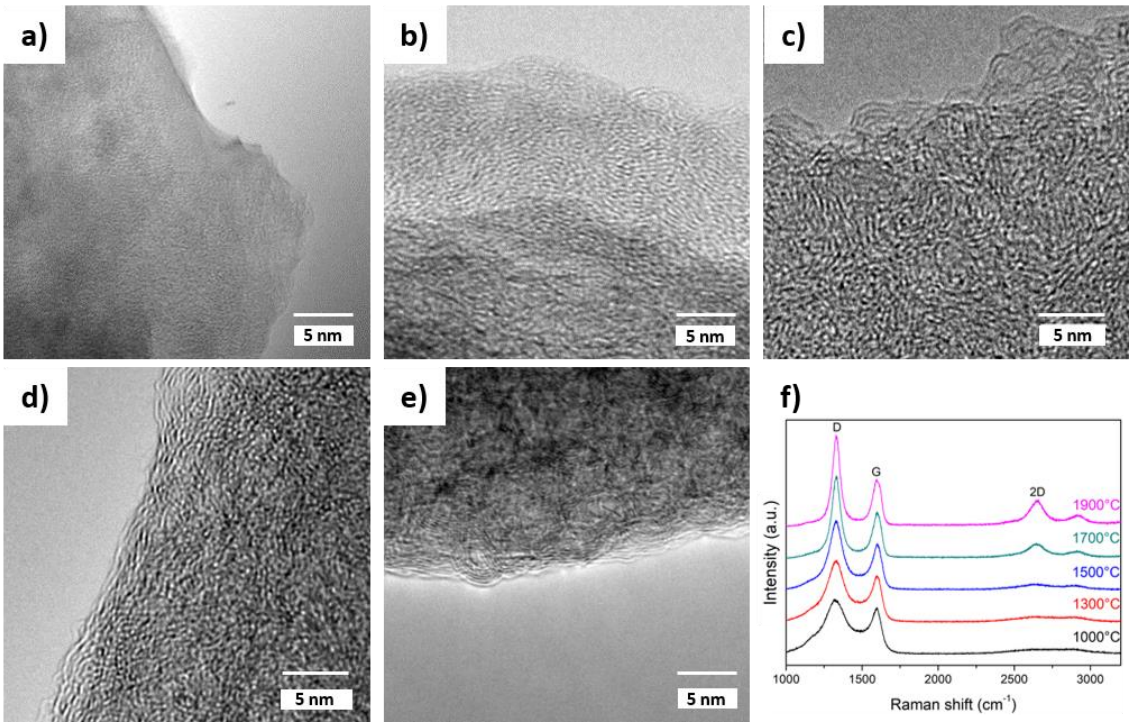


Figure 4.4 TEM images of a) GC1000, b) GC1300, c) GC1500, d) GC1700, e) GC1900, and f) Raman spectra as a function of carbonization temperature.

The PDF can be used to observe changes in the local structure (Figure 4.3d). The peak at ~1.3 Å (marked as d_1) corresponds to the direct C-C and C-O bonds (a schematic of all the relevant distances is provided in Figure 4.5). The peak at ~2.8 Å (marked as d_2) relates to the second nearest neighbouring carbon and the presence of the signal at ~3.1Å (marked as d_3) indicates that the structure has the characteristic interatomic distance of the C1-C4 distance in a 6-membered aromatic ring structure. An increase in the ratio of the d_2/d_1 peak (Figure 4.3f) shows that increasing carbonization temperature increases the average number of carbons in the 2nd nearest neighbour position compared to the number of directly bonded carbons. The difference between the ratio of the d_2/d_1 is largest between the precursor (HTC sample before pyrolysis) and GC1000, as expected given that the HTC sample is dominated by 5-membered ring structures, aliphatic chains and contains few aromatic compounds.[254] The difference between the d_2/d_1 ratios is also relatively large between GC1000 and GC1300. This difference decreases after GC1300, which shows that in between the graphitic domains there are still 5-membered ring structures, defects and crosslinkers left up to 1300°C that can act as feedstock for the formation of new graphitic domains, as the size of the graphitic domains does not change much in this temperature range. Above 1500°C the changes are likely related to the removal of edge terminations as the basal plane increases from 2 to 4 nm (Figure 4.3). This is supported by the increase in the d_3/d_1 intensity ratio, suggesting a higher density of aromatic structure with increasing carbonisation temperature.

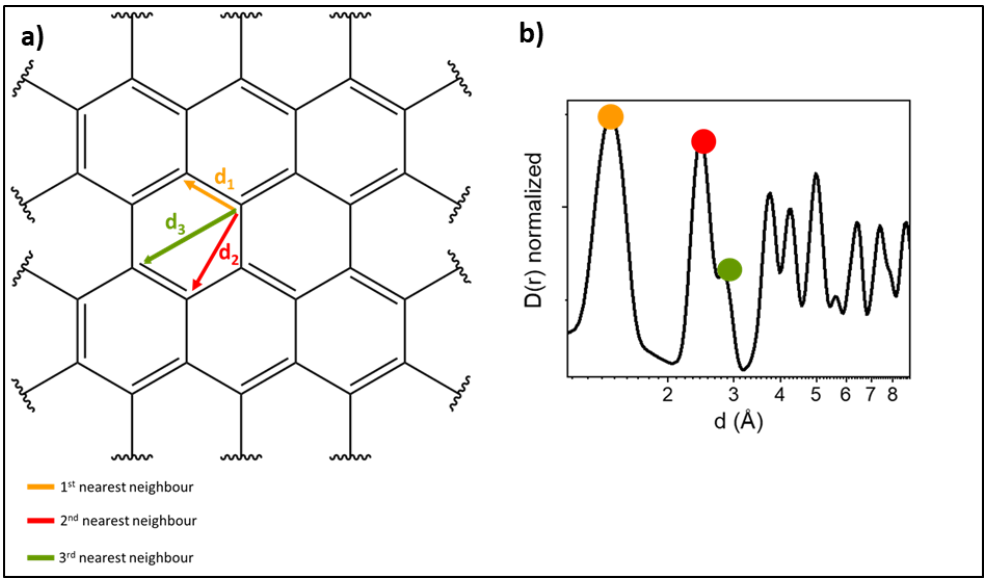


Figure 4.5 a) Schematic of PDF data along a graphene sheet. b) Schematic of nearest neighbour positions in PDF data.

The presence of heteroatoms in the GCs was investigated by XPS to evaluate concentration of heteroatoms that may contribute to possible Faradaic reactions occurring on the surface of the

electrode material [255,256], and the deconvoluted C1s and O1s spectra are shown in Figure 4.6b.The peaks at 533.3 eV and 531.5 eV in the O1s spectra are assigned to C-O and C=O species respectively. The proportion of these peaks decreases with increasing carbonization temperature, this assignment is confirmed by the deconvoluted peaks at 287.6 eV and 288.2 eV in the C1s core-level spectrum. The XPS analysis (Table 4.1 and Figure 4.6) shows that there is an increase in carbon content (C1s, at%) and a reduction in oxygen content (O1s, at%) with increasing carbonization temperature. Overall, the high-temperature materials have fewer functional groups and defects, narrower interlayer distances and larger pore sizes compared to the low-temperature materials. [37]

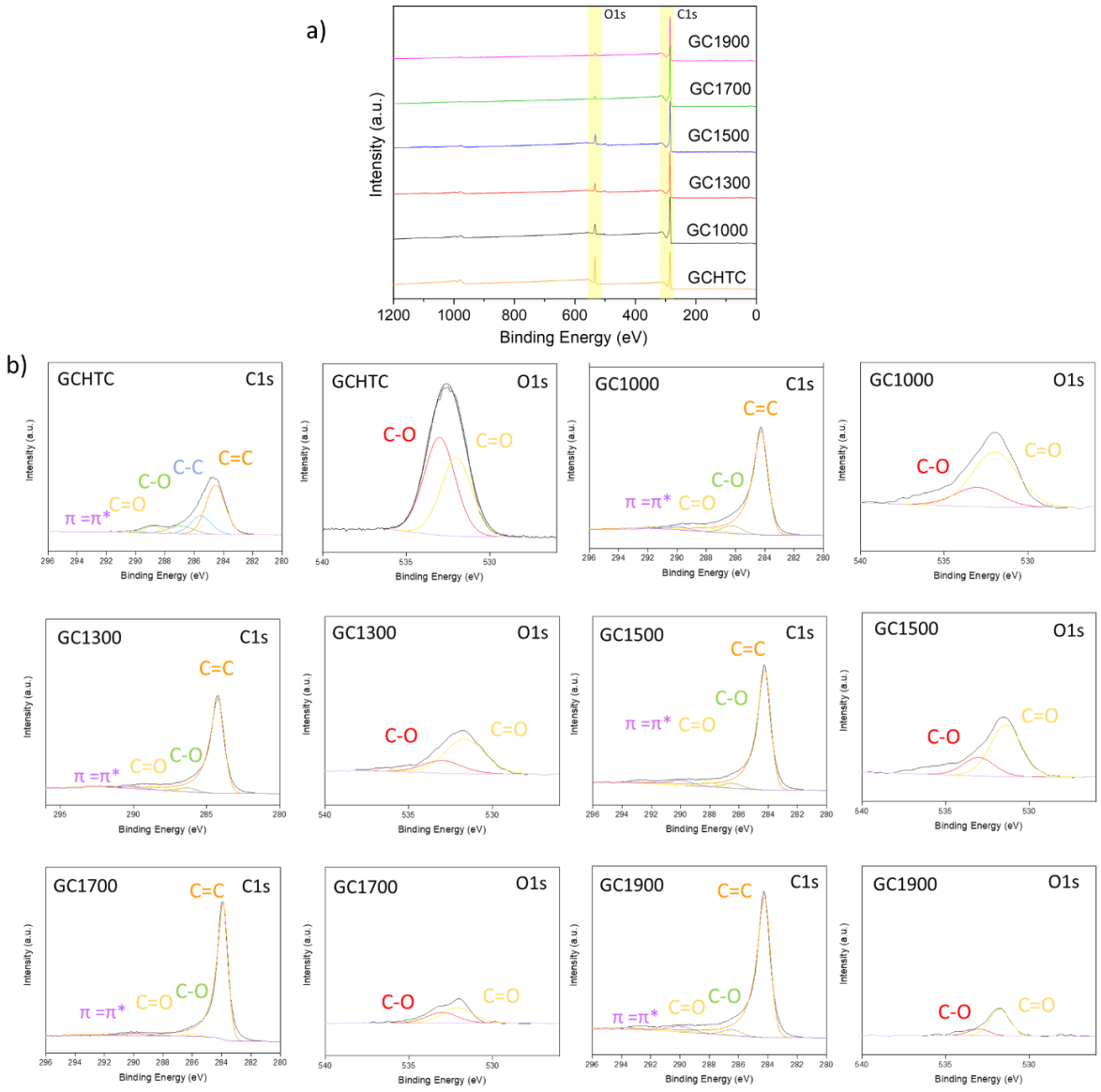


Figure 4.6 a) Wide survey XPS spectra and b) core level C1s and O1s spectra for the materials GCHTC (before carbonization) and after carbonization at each temperature

4.2.2 Electrochemical Characterisations

To observe the effects of all these structural differences on the electrochemical storage performance, GCs were electrochemically tested in half-cell configuration with Na metal as the counter electrode. Figure 4.7shows the first three CV curves of the GCs at a scan rate of 0.1 mVs^{-1}. In the first cathodic scan of all the samples, the broad peak at around 0.4 V may be attributed to the reactions of the active sites on the carbon anode material with solvent molecules and electrolyte ions leading to the formation of the SEI in the first cycle.[31] The irreversible area under the broad peak of GC1000 is much higher compared to the higher temperature materials, due to the higher number of defects and surface functional groups present which react irreversibly with the electrolyte. Additionally, GC1000 has a larger specific surface area which facilitates the SEI formation, and also contributes to the initial irreversible capacity. A sharp peak in the low potential region of 0.1 V can be ascribed to the oxidation or reduction reactions that involves electron transfer.

Table 4.1 Summary of the characteristics of the GC materials. S_{N2} and S_{CO2} surface area determined by N_2 and adsorption CO_2 adsorption respectively. r is the correlation coefficient of BET measurement. C1s and O1s are atomic compositions obtained by XPS. STD deviation formula used in calculations is shown in Appendix II.

Materials	GC1000	GC1300	GC1500	GC1700	GC1900
d_{002} (Å)	3.75 (±0.004)	3.68 (±0.003)	3.66 (±0.002)	3.50 (±0.004)	3.45 (±0.002)
d_{100} (Å)	2.04 (±0.001)	2.04 (±0.001)	2.04 (±0.001)	2.05 (±0.001)	2.10 (±0.001)
Pore Size $_{SAXS}$ (nm)	1.6 (±0.017)	2 (±0.018)	2 (±0.019)	2.6 (±0.034)	3.5 (±0.044)
I_D/I_G	1.15	1.32	1.50	1.82	2.02
L_a (nm)	0.9	1	1.1	1.2	1.3
S_{N2} (m^2g^{-1}) / (r)	11/ (0.99)	4 /(0.99)	2 / (0.99)	1/ (0.98)	0.5 (0.96)
Pore Size $_{N2}$ (nm)	1.6	2.7	2.8	2.9	4.8
Pore Volume $_{N2}$ (cc/g)	0.021	0.020	0.018	0.003	0.003
S_{CO2} (m^2g^{-1})/ (r)	496/ (0.99)	164/ (0.99)	76/ (0.99)	5.2/ (0.97)	2.6/ (0.95)
Pore Volume $_{CO2}$ (cc/g)	0.36	0.24	0.21	0.005	0.004
C1s, %	86.2 (±0.5)	89.6 (±0.6)	90.3(±0.3)	97.6 (±0.3)	97.8 (±0.4)
O1s, %	13.8 (±0.2)	10.4 (±0.3)	9.7 (±0.2)	2.4(±0.5)	2.2(±0.5)
1st Cycle Capacity ($mAh\ g^{-1}$)	265	301	210	81	66
STD deviation ($mAh\ g^{-1}$)	25	37	32	13	17
ICE (%)	72	83	74	76	66

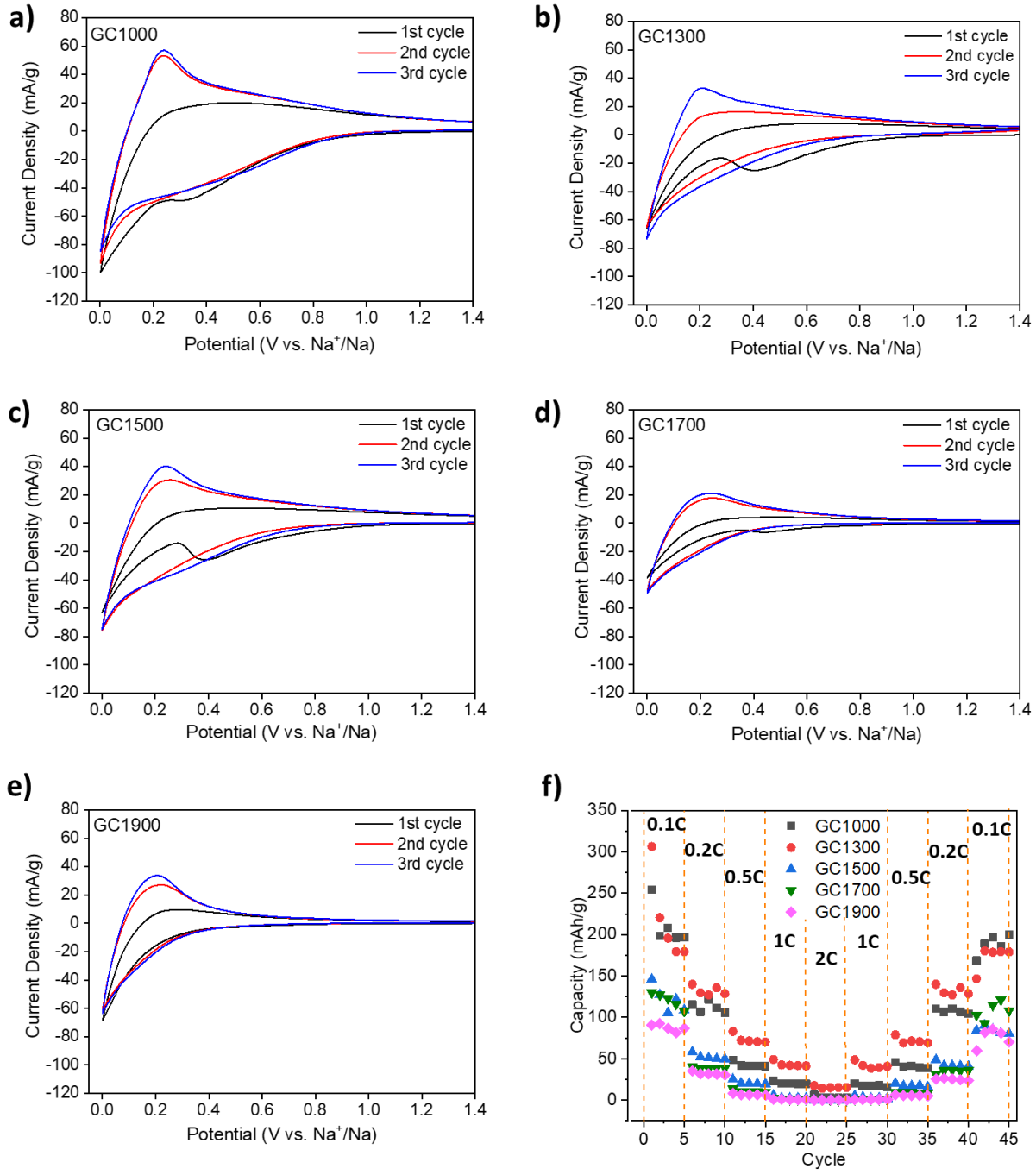


Figure 4.7 Cyclic Voltammetry a) GC1000 b) GC1300 c) GC1500 d) GC1700 and e) GC1900 and f) rate performance of the discharge capacities at current densities between 30 and 600 mA/g.

Figure 4.8a shows the galvanostatic potential profiles of the first and second discharge-charge cycles for the hard carbons tested at 0.1 C. GC1300 delivers the highest total discharge capacity of 301 mAh/g with an Initial Coulombic Efficiency (ICE) of 83% (Table 4.1). The voltage profile can be divided into two regions, the high voltage sloping region between 1 and 0.1 V and the low voltage plateau region around 0.1 V. The capacities of these separate regions were

evaluated from the discharge profiles in the first cycles (Figure 4.8b). It can be seen that as the carbonization temperature increases, the sloping region capacity contribution decreases. GC1000 with the highest oxygen content shows the largest sloping region capacity contribution (Figure 4.8b), consistent with previously proposed sodium storage models where oxygen-containing defects offer favorable sodium adsorption sites.[115,257] Besides the contribution of surface functional groups and defects, variations of interlayer distance (d_{002}) between graphitic layers also affect Na insertion, as the expanded graphitic layers serve as Na storage sites. A larger contribution to the sloping region is seen in the lower temperature hard carbons with larger interlayer distance as compared to the higher carbonization temperatures. Therefore, contribution of both Na adsorption on defect sites and insertion in turbostratic carbon domains can be observed in sloping voltage profiles. We assume that after all the existing interlayer spaces and defects reaches its maximum sodium storage capacity, pore filling starts corresponding to the low voltage plateau region. As in the example of temperature increase from 1000 ºC to 1300 ºC, the plateau capacity of the higher temperature materials is expected to increase with the larger pore sizes. Nevertheless, at higher temperatures, while pore size continues to increase, the interlayer spacing narrows, the ion diffusion pathways to reach some pores therefore become inaccessible, corresponding to decrease in plateau region capacity. Therefore, an optimum concentration of internal (closed) porosity with energetically favorable interlayer distance is important to maximize the plateau capacity.

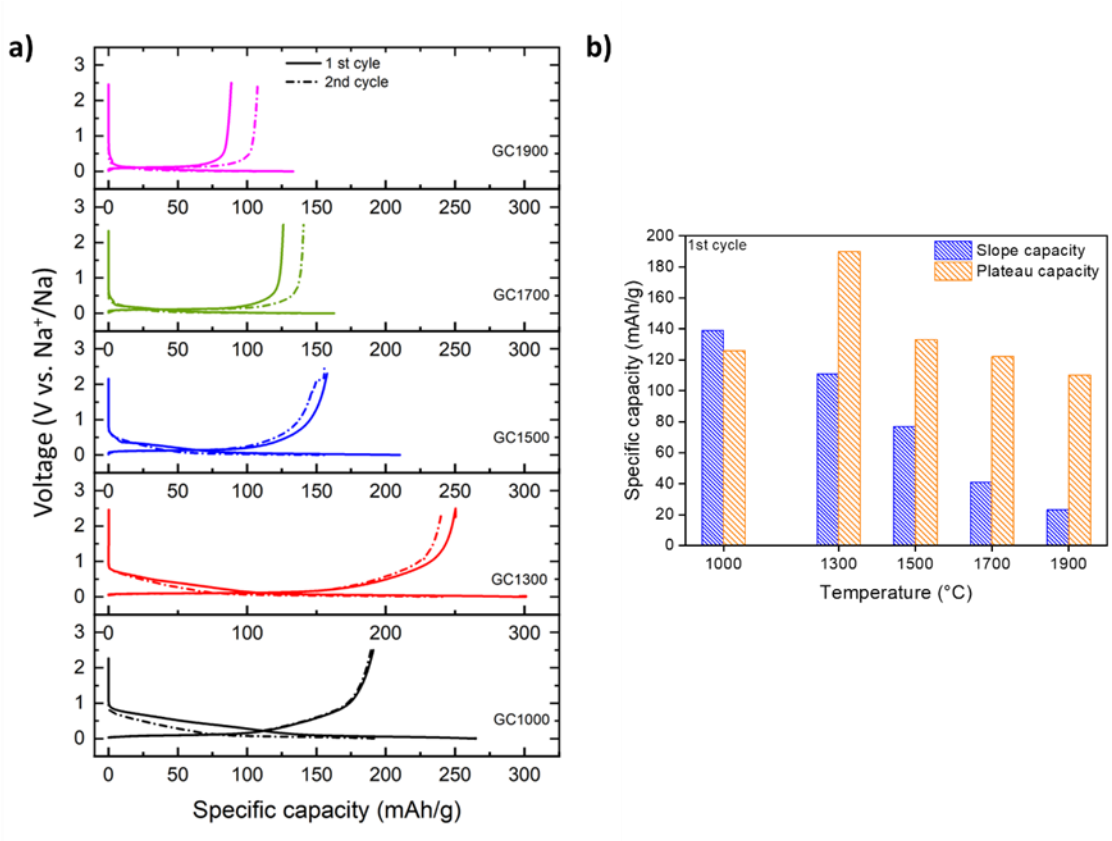


Figure 4.8 a) The galvanostatic sodiation (discharge) and desodiation (charge) potential profiles of GC1000, GC1300, GC1500, GC1700 and GC1900. b) Specific capacities of different samples at high voltage sloping region (0.1 – 1.0 V) and low voltage plateau region (around 0.1 V)

4.2.3 *In-situ* Electrochemical Dilatometry

The Na storage behaviour of the electrodes was further studied by in situ electrochemical dilatometry (ECD, Figure 4.9a) over the first three cycles. The thickness of the electrodes used in dilatometry measurements quite similar to (error margins are shown in Appendix I, Figure 1. 2) the thickness of electrodes used in the coin cell for the galvanostatic cycling. The initial thicknesses of GC1000, GC1300, GC1500, GC1700, GC1900 (film thickness without Al foil) were 104 µm, 162 µm, 127 µm, 94 µm, 81 µm. As an example, Figure 4.9 shows results for the carbon with the highest capacity (GC1300). Results for the other electrodes are shown in the Appendix I, Figure 1. 2. Due to the difference of the cell setups of ECD and coin cells, ICE values and capacities obtained from each setup might be variable. As the loading and thickness of the different electrodes deviated from each other, it is difficult to establish a quantitative link between the performance of the electrode and their expansion/shrinkage. However, some interesting observations can be made. (1) The electrodes undergo an activation cycle, i.e., the first cycle leads to a slight increase in electrode thickness. This increase might originate from side reactions, e.g., SEI formation and/or rearrangement of particles that creates variation in

electrode microstructure. (2) The expansion (difference in thickness between initial and desodiated state, Appendix I, Figure 1. 2) for all electrodes was in the range of 1.03 to 0.25 % only (Table 4.2). These values are much smaller compared to when solvated sodium ions are intercalated[223], indicating that solvent cointercalation into the carbon matrix does not take place. Small values can be also found for other carbon composites at similar capacity values. [258,259] Considering full cells, minimal expansion will help to achieve a long cycle life. (3) Figure 4.9 compares the electrode expansion during sodiation for the different electrodes (2nd cycle, data was normalized). Although sodiation occurs at constant current, the expansion of the electrode is not linear.

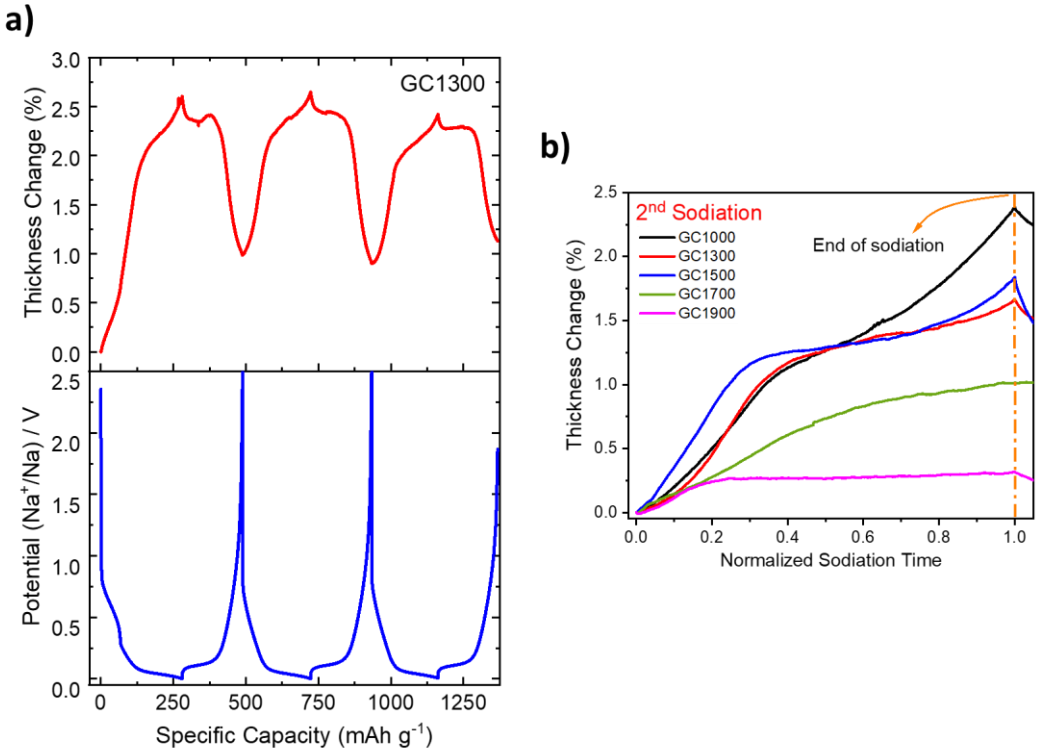


Figure 4.9 a) In-situ electrochemical dilatometry measurements of the electrode thickness change inthe first three cycles for GC1300 b) percentage thickness change of each electrodes during the second sodiation.

As mentioned above, the voltage profile can be roughly divided into a sloping region and a plateau region. The ECD results show that the expansion of the electrode is greater in the sloping region than in the plateau region. This supports the concept that the sloping region is due to ion insertion between graphitic layers since sodium intercalation in graphite typically results in large interlayer expansion.[260] Conversely, pore filling results in minimal thickness change, and therefore supports the assignment of this process occurring during the plateau region, where less pronounced electrode expansion is observed.

Table 4.2 Breathing percentage of electrode after first cycle.

	Breathing, %
GC1000	0.58
GC1300	1.03
GC1500	0.40
GC1700	0.97
GC1900	0.25

4.2.4 *Ex-situ* SEM images

The e*x-situ* SEM images of GC1300 (Figure 4.10) show cross-sections of the electrode after the first sodiation and desodiation process. Since the electrode has a variable surface height, three different regions were measured to obtain the average thickness (before cycling ~144, after the first sodiation ~178 µm, after the first cycle ~170 µm). The result is consistent with the *in-situ* electrochemical dilatometry observation that the structure remained expanded as compared to the initial state of the electrode. From the experimental characterisation of the hard carbon samples above, it was shown that the materials contain expanded graphitic stacks with different interlayer distances and graphitic surfaces with oxygen heteroatom defects.

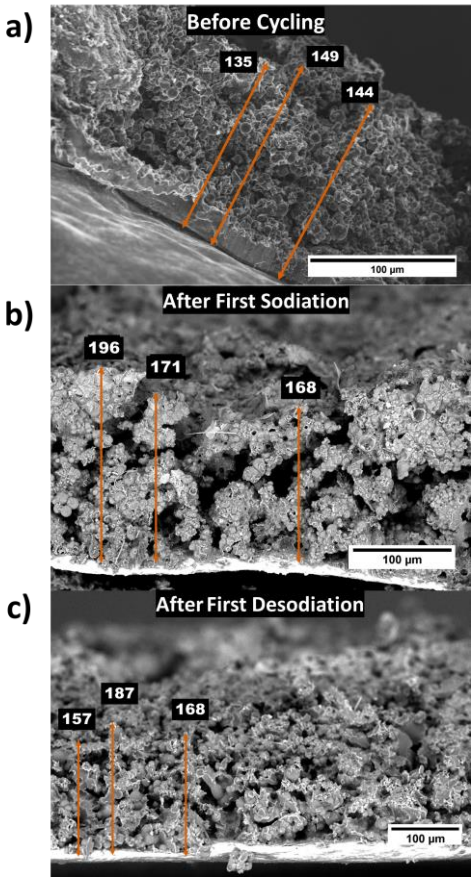


Figure 4.10 Ex-situ SEM pictures for GC1300 a) before cycling b) c) after first sodiation and d) at the end of first cycle.

4.2.5 Computation calculations

To bring atomistic insight into the effect of oxygen-containing surface defects and differing graphitic interlayer distances on the sodium storage and incorporation in the hard carbon samples, density functional theory (DFT) simulations were employed. The surface defects and oxygen heteroatoms on the hard carbon surfaces were modelled in terms of oxygen defects on a graphene monolayer. To understand the difference in intercalation behaviour for the different hard carbon samples with varying graphitic interlayer distance, a double layer planar graphitic model was employed. The effect of pore size on sodium incorporation in hard carbon was probed in a previous publication.[149] To study the effect of different interlayer spacing on the sodium incorporation and migration, the sodium binding energy in the bi-layer graphitic layers with different d_{002} was calculated (see supporting information for details). To calculate the sodium binding energy (E_{bind})[261,262], Appendix I, equation 2 was adapted to include sodium in between two graphitic sheets. The calculated binding energies are presented in Appendix I Table 1. 1, with a more negative E_{bind} indicating a more energetically stable structure. It is clearly seen from Appendix I Table 1. 2 that the sodium incorporation in the graphitic stacks become more favourable with increasing d_{002}. Hence, GC1000 is the most favourable for sodium intercalation from these calculations, whereas GC1900 would not be expected to store much sodium in the graphitic stacks with calculated d_{002}. The sloping region is partly attributed to sodium storage in expanded graphitic stacks. Hence, a stronger (more negative) E_{bind} is in line with the more distinct sloping regions observed for the GC1000, GC1300, and GC1500 samples as compared to GC1900. From the calculated E_{bind}, the Na storage capacity of GC1700 should also have contribution from the graphitic stack filling in its sloping region. However, the distinctly smaller sloping region of GC1700 compared to that of the lower carbonisation temperature samples (GC1000, GC1300, and GC1500) indicates that the capacity from the graphitic stack filling in GC1700 is relatively small.

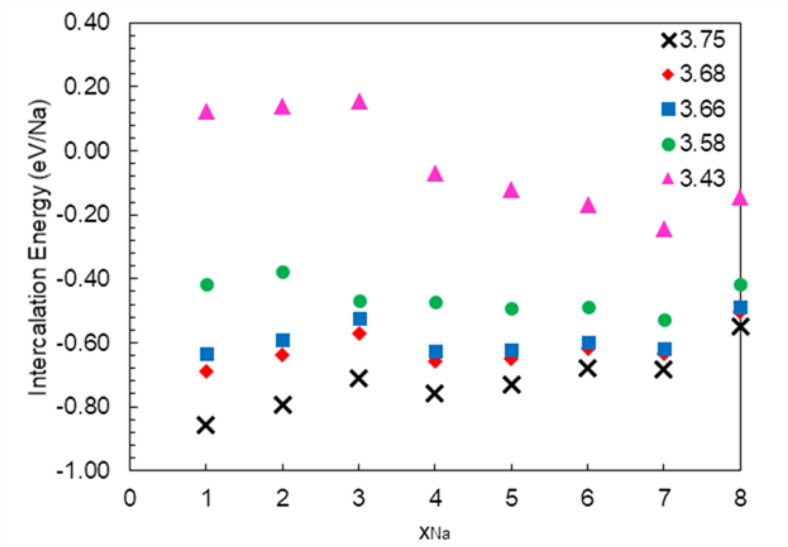


Figure 4.11 Intercalation energy per sodium atom as a function of number of sodium (x) in Na_xC_{64} with different interlayer distance.. 3.75 corresponds to GC1000, 3.68 to GC1300, 3.66 to GC1500, 3.58 to GC1700, and 3.43 to GC1900.

To form an understanding of the sodium storage in the graphitic models with different interlayer distances, the intercalation energy per sodium atom at different sodium loading (up to 8 Na) in the graphitic models of different interlayer distance (Figure 4.11) was calculated. It is clearly seen that sodium intercalation in GC1900 is energetically unfavourable. GC1900 would hence be expected to have a lower sodium intercalation potential than the samples with higher average interlayer distance. Overall, the calculated intercalation energies show that sodium intercalation increases with increasing the interlayer distance (Figure 4.11), which could explain the higher sloping region capacities measured for the GC1000, GC1300 and GC1500 samples compared to high temperature materials GC1700 and GC1900. To assess the effect of oxygen-containing defects on sodium storage, which would contribute to the sloping region, a selection of graphene defects was modelled (Figure 4.12). These defects have not been explicitly shown to be present in the experiments above, due to the difficulty in identifying/specifying the exact defects from the XPS analysis. Nonetheless, the models here allow us to explore different possible defect configurations at the atomic level and will serve as a guide to how oxygen-containing defects influence the sodium adsorption. In a previous publication, the effect of a wider selection of graphene defects on sodium adsorption was investigated, and reference to that study is made here.[241]

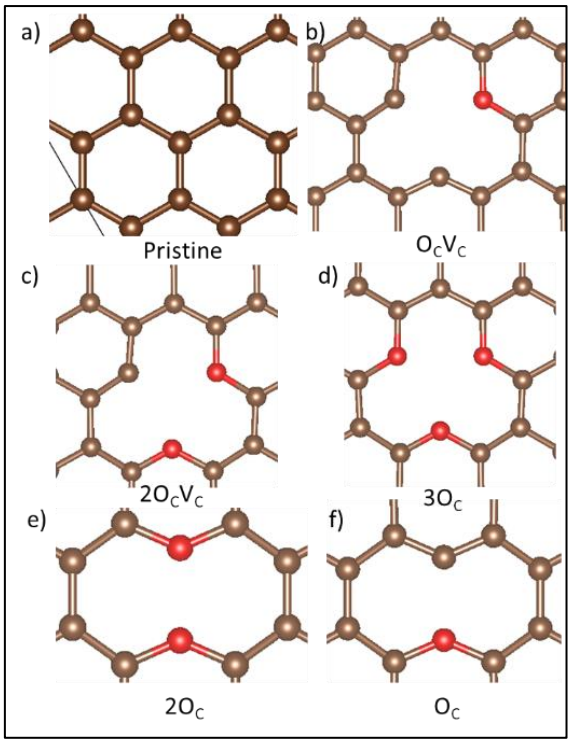


Figure 4.12 Defective graphene models with a) no defect (pristine graphene), b) one oxygen substituted carbon site, with one carbon vacancy site (O_CV_C), c) two oxygen substituted carbon sites, with one carbon vacancy site ($2O_CV_C$), d) three oxygen substituted carbon sites ($3O_C$), e) two oxygen substituted carbon sites ($2O_C$) [241], and f) one oxygen substituted carbon site (O_C). Structures were visualized with VESTA.[263]

For each postulated defect in Figure 4.12, its equilibrium defect formation energy (E_f^{defect}) [264,265] was calculated (see the supporting information). The calculated E_f^{defect} are collected in Appendix I, Table 1. 2 and show that oxygen-containing defects are energetically favourable on the graphene basal plane. Comparing E_f^{defect}, none of the investigated defects have higher E_f^{defect} than the $3O_C$ defect, or lower than the $2O_C$ defect. The formation energies of the O_C and $2O_CV_C$ defects are furthermore relatively low, which indicates that a high concentration of these defects in the hard carbon basal planes would be probable. This confirms the experimental observation that hard carbons are prone to the formation of oxygen surface defects. To assess the sodium storage on these defective surfaces, the sodium adsorption energy (E_{ads}^{Na}) [261,262] was calculated (equation S2). The more negative the adsorption energy is, the stronger the adsorption. The calculated adsorption energies for sodium on defect sites are collected in Appendix I, Table 1. 1. The presence of oxygen-containing defects improves the sodium storage capacity of the carbon surface, except for the O_C defect (-2.85 eV) which shows no change in the sodium adsorption energy. The strong sodium adsorption energies calculated for the O_CV_C defect indicate that this defect would greatly improve sodium storage. Hence, in the

hard carbon samples with more oxygen content and oxygen surface defects (i.e., GC1000, GC1300, and GC1500), a considerable amount of sodium would be expected to be stored on defect sites. Therefore, a larger contribution to the sloping region capacity due to the presence of these kinds of defects in the lower temperature sample would be expected as compared to the GC1700 and GC1900 samples. This is consistent with the XPS results in Table 1 which show that GC1700 and GC1900 have a lower oxygen content than the lower temperature samples, and hence the contribution from sodium storage on defect sites in the GC1700 and GC1900 samples will be much less. Hence, the sloping region of GC1700 is much shorter than for GC1000-1500.

4.3 Conclusions

In this study, a series of hard carbon materials derived from glucose was produced, and the effect of the different hard carbon configuration on the sodium storage mechanism investigated by using TEM, Raman, XPS, SAXS/WAXS, SANS, and gas adsorption techniques. It demonstrates that the presence of oxygen defects and large interlayer spacing has a more considerable contribution to the sloping region. Experimental results also supported by DFT simulations showing that sodium intercalation ability increases with increasing interlayer distance, while oxygen-containing surface defects improve the sloping region capacity. Increasing the number and size of the internal (closed) pores with increasing carbonization temperatures enhanced contribution of plateau region capacity up to 75% of total capacity. In situ ECD measurements reveal that expansion of the electrodes (expansion/shrinkage during cycling) is very small which is helpful considering full cells. Moreover, sodium storage during the sloping region leads to a greater electrode expansion compared to the plateau region. This led us to hypothesize that the slope region capacity is due to sodium ion adsorption on disordered graphene layers and intercalation into graphene layers with suitable spacing. In the plateau region sodium ion storage mechanism dominates over pore filling.

5 TUNING THE CLOSED PORE STRUCTURE OF HARD CARBONS FOR NA-ION BATTERIES

5.1 Introduction

In the previous chapter, closed pores are found to be the main microstructure in charge of sodium storage especially in the plateau region capacity. Therefore, it is critical for high-capacity carbon anodes to develop a strategy to succeed in the construction of an optimal closed pores framework. These optimization issue compelled us to in them further and to answer following questions about, what would happen if materials with more closed porosity is used as NIB anodes? What would happen if we increase the size of the closed pores? Would we see an even greater capacity in especially low voltage plateau region? The soft template method has received greater attention due to the limited synthesis steps, easy production of large quantities[266] and moreover, the possibility of designing various structures of carbon materials.[267–269] Generally, this method involves three steps to form a mesoporous carbon, (1) solid surfactant self-assembly, (2) developing of carbon precursor over this surfactant self-assembly, which can be achieved by solvent-annealing strategy, solvent evaporation induced self-assembly (EISA) strategy or hydro/solvo thermal treatment[268–272], (3) the complete removal of the template via further carbonization to obtain the mesoporous solid. Here in this chapter, mesoporous hard carbon materials were produced by means of self-assembly of phloroglucinol as carbon precursor, glyoxylic acid as a cross-linker and catalyst, and Pluronic F127 as a structure templating agent, using a solvothermal approach. The resulting materials were carbonized further at high temperatures to obtain mesoporous hard carbons. This chapter is divided into four sub-sections. The first part is dedicated to the preliminary hard carbon material characterizations. In the second part, the electrochemical performance of hard carbon electrodes with different morphology in $NaPF_6$ EC:DMC and consequent evolution of the SEI layer on the sodiated electrodes are investigated. In the third sub-section, a comparative study of electrochemical performance and storage mechanism of hard carbons obtained from HTC method (in chapter 4) with native closed micro porosity and soft templated hard carbons that consists of closed mesopores is reported.

5.2 Results and discussion

5.2.1 Hard carbons: texture evolution with temperature

To obtain hard carbons with tailored porosities, phloroglucinol and glyoxal were hydrothermally carbonised in the presence of a soft templating agent (Pluronic F127). In the

presence of Pluronic F127 micelles, the crosslinked resin develops around the templated domains, and micro-mesoporous structures are expected once the sacrificial polymer is removed by high-temperature pyrolysis at 1000 °C, 1300 °C and 1500 °C (Figure 5.1). Materials obtained at these temperatures were labelled accordingly as ST1000, ST1300 and ST1500, respectively.

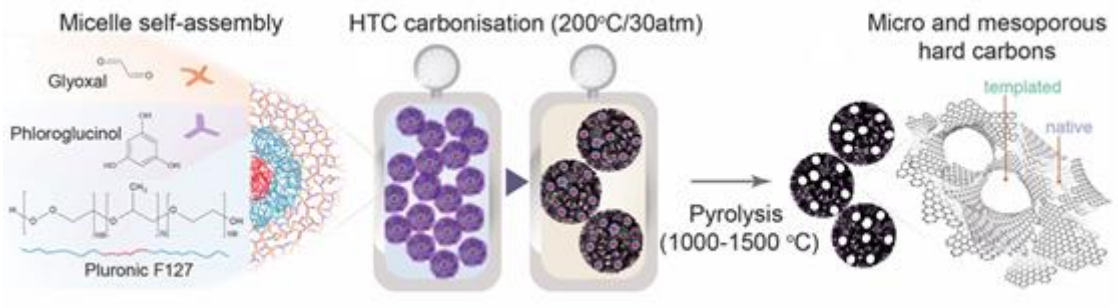


Figure 5.1 Formation of mesoporous structures via solid surfactant self-assembly and developing of carbon precursor over this surfactant self-assembly during HTC, followed by the complete removal of the template via high temperature pyrolysis.

Representative SEM images (Figure 5.2) show the typical spherical morphology of the carbonised samples with particles ranging from 2 to 4 µm, irrespective of temperature. TEM (Figure 5.3a,b,c) of the sample treated at 1000 °C shows a disordered structure dominated by amorphous domains, proving this thermal energy is insufficient to initiate the growth of graphitic structures. Above 1300 °C graphene layers with random orientation are observed, while more organised and longer graphitic domains are observed above 1500 °C. These observations showed a similar trend to that of glucose derived materials.

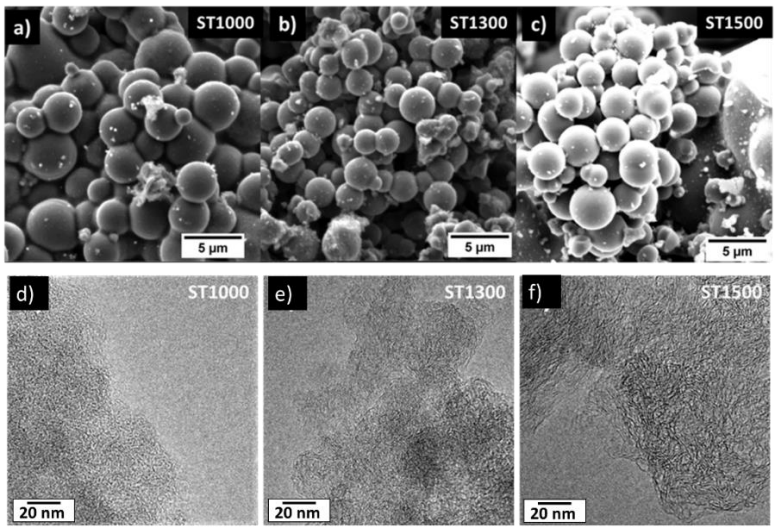


Figure 5.2 SEM images of a) ST1000 b) ST1300 and c) ST1500, TEM images of d) ST1000 e) ST1300 and f) ST1500 showing the evolution of graphitic domains

The structural ordering of these prepared hard carbon materials with increasing temperature, in agreement with the TEM observations (Figure 5.2), was proved by Raman spectroscopy through the evolution of the typical hard carbons' broad D- and G-band signals. As temperature increases, the sharpening and narrowing of both D- and G-bands becomes more apparent, simultaneously enhancing the I_D/I_G ratio. ST1500 shows higher structural order (I_D/I_G = 1.48) than ST1300 (I_D/I_G = 1.34) and ST1000 (I_D/I_G = 1.29).

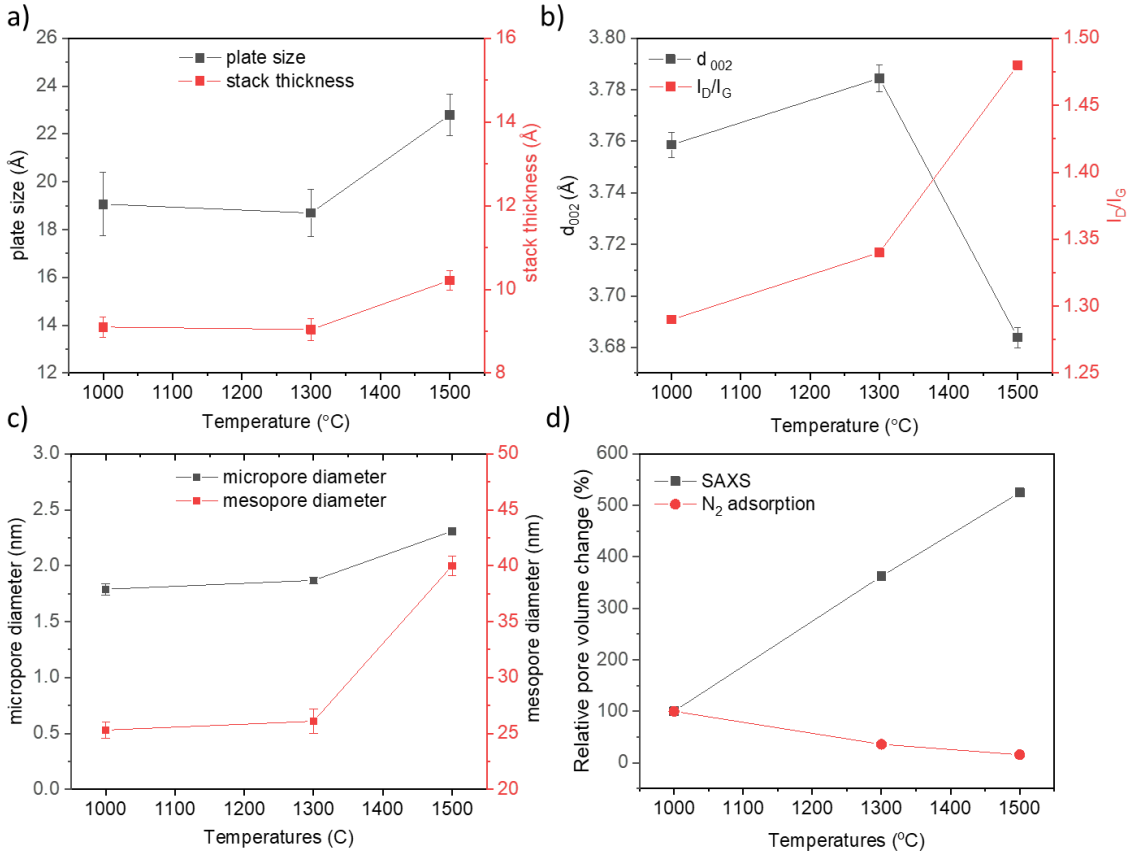


Figure 5.3; a) basal plane size and thickness of basal plane stacks obtained from the 100 and 002 peaks, b) I_D/I_G ratio from Raman spectra and average interlayer spacing between the graphitic basal planes (d002) determined from the 002 peak, c) Pore size diameter of the micropores native to hard carbon and mesopores formed from the templating polymer, d) Relative pore volume changes obtained from gas adsorption and SAXS pattern.

A more detailed analysis on the development of these graphitic domains with temperature was done through X-ray and total neutron scattering. As shown in Appendix II Figure 2. 1, from the neutron structure factor (Q) it is possible to discern the shift to lower Q values of the peak corresponding to the (002) diffraction of the local graphitic layers at 1.8 $Å^{-1}$, while the (100) peak at 3 $Å^{-1}$ remains almost unaltered. From the fitting of the (002) diffraction it was possible to estimate a decreasing interlayer distance of *ca.* 3.75 Å for the material prepared at 1000 °C and of 3.68 Å for that annealed at 1500 °C (Figure 5.3f) corroborating the enhancement of

graphitisation and alignment of the layers with temperature. Alongside, the domain thickness and in-plane crystallite size, calculated using the Scherrer equation, show how temperature promotes the growth of the domains both in lateral dimensions (from 19 to 23 Å) and thickness (from 9.0 to 10.3 Å). More detail on the local structure is seen in the pair distribution function (PDF) (Appendix II, Figure 2. 1b) and difference PDFs (Appendix II, Figure 2. 1c). The short-range correlations of the C-C bonds of a hexagonal unit in a graphene layer are represented by the peaks up to 5 Å. The signals at 1.4 Å and 1.64 Å show a mixture of sp^2 and sp^3 hybridized carbon, respectively. Upon heating, to 1000 °C the sp^3 hybridized C-C correlation disappears, and the signal at 2.9 Å (3rd neighbour carbon) which is a characteristic of the six-membered rings becomes more pronounced, indicating the growth of aromatic domains within the material (Appendix II, Figure 2. 1c), as confirmed by TEM and Raman spectroscopy. XPS also confirmed the removal of polar surface groups and heteroatom defects by increasing carbonization temperature. Analysis of the XPS data shows a composition of 37 at% O and 62 at% C for ST1000; this ratio is slightly decreased after high-temperature carbonisation, with a decreasing amount of O with increasing temperature (Table 5.1). The porosity of the carbons prepared in this work arises not only from the native disordered structure of hard carbons but also from the solvothermal synthesis in which a templating agent was employed. Porosity was evaluated through N_2 adsorption analysis (Figure 5.4) showing the transition of a predominantly mesoporous carbon (ST1000) to a substantially less porous material in ST1500. As summarised in Table 5.1, it is possible to discern the surface area and pore volume decrease with increased carbonization temperature.

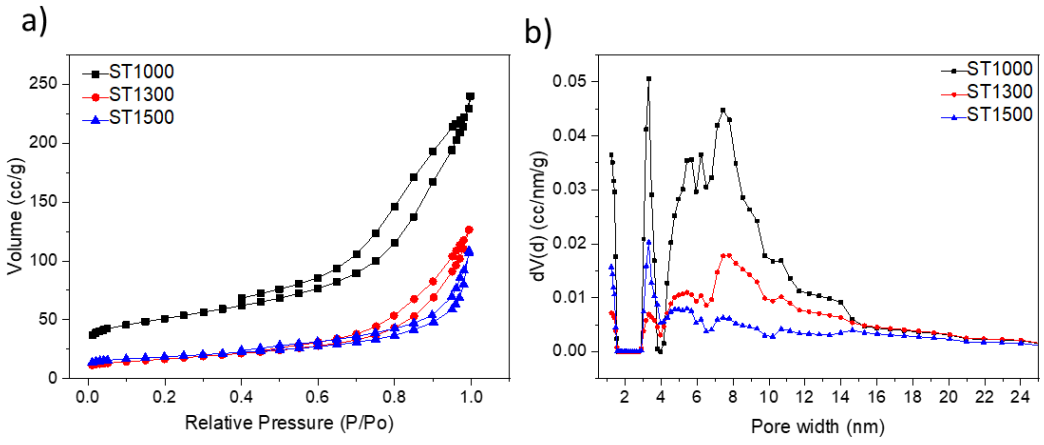


Figure 5.4 a) N_2 adsorption/desorption isotherms at 77 K, b) pore size distributions of ST1000-ST1500 obtained from the NLDFT method.

The closed pores are also essential to understand, as they have a substantial effect on the sodium storage performance in hard carbons at low potentials.[219,220] In this case, small angle neutron

scattering (SANS) was used to detect closed pores. By evaluating the Guinier-Porod region[129,273] observed at 0.2 $Å^{-1}$ in the scattering (Appendix II, Figure 2. 2) profile, the size and degree of each of these porosities could be calculated. As shown in Figure 5.3, pores below 2.5 nm could be related to the native pores found in hard carbon [36,69,225] and those above 25 nm to the template effect. The closed pore diameters vary from 1.8 to 2.3 nm for micropores and 25 nm to 40 nm for mesopores. The higher pyrolysis temperature (ST1500) shows a more distinctive peak in the Guinier-Porod region, signifying an increase in porosity and closed pores diameters with increasing carbonization temperature. Porosity measurements suggest that closed porosity is developing whilst open pores are diminishing with increasing pyrolysis temperature.

Table 5.1 Surface area and pore volumes of the hard carbon materials calculated from N_2 adsorption isotherms, C1s and O1s are atomic compositions obtained by XPS. r is the correlation coefficient of BET measurement.

Sample	N_2 adsorption		C 1s, %	O1s, %
	Surface Area, m^2/g (r)	Pore Volume, cc/g		
ST1000	181 (0.99)	0.324	62 (±0.5)	37 (±0.3)
ST1300	66 (0.99)	0.116	65 (±0.4)	34 (±0.4)
ST1500	21 (0.99)	0.051	67 (±0.5)	33 (±0.4)

5.2.2 Electrochemical performance as a function of hard carbon morphology

The electrochemical performance of the materials prepared at different carbonisation temperatures was evaluated in half-cells, using metallic sodium as the counter electrode. Figure 5.5 shows the initial galvanostatic discharge-charge profiles for all materials at 0.1C between voltages of 0 and 3 V. As expected, with its low surface area and higher degree of closed porosity, ST1500 shows the highest initial capacity of 525 mAh/g with initial Coulombic efficiency (ICE) of 60%. On the other hand, ST1000 material with high functionality (e.g., oxygen-containing surface groups) and high surface area (Table 5.1) shows the highest

irreversible capacity. In the discharge profile of ST electrodes, higher voltage plateau region was observed at around 0.4-0.5V, which could be an indication of redox reactions.

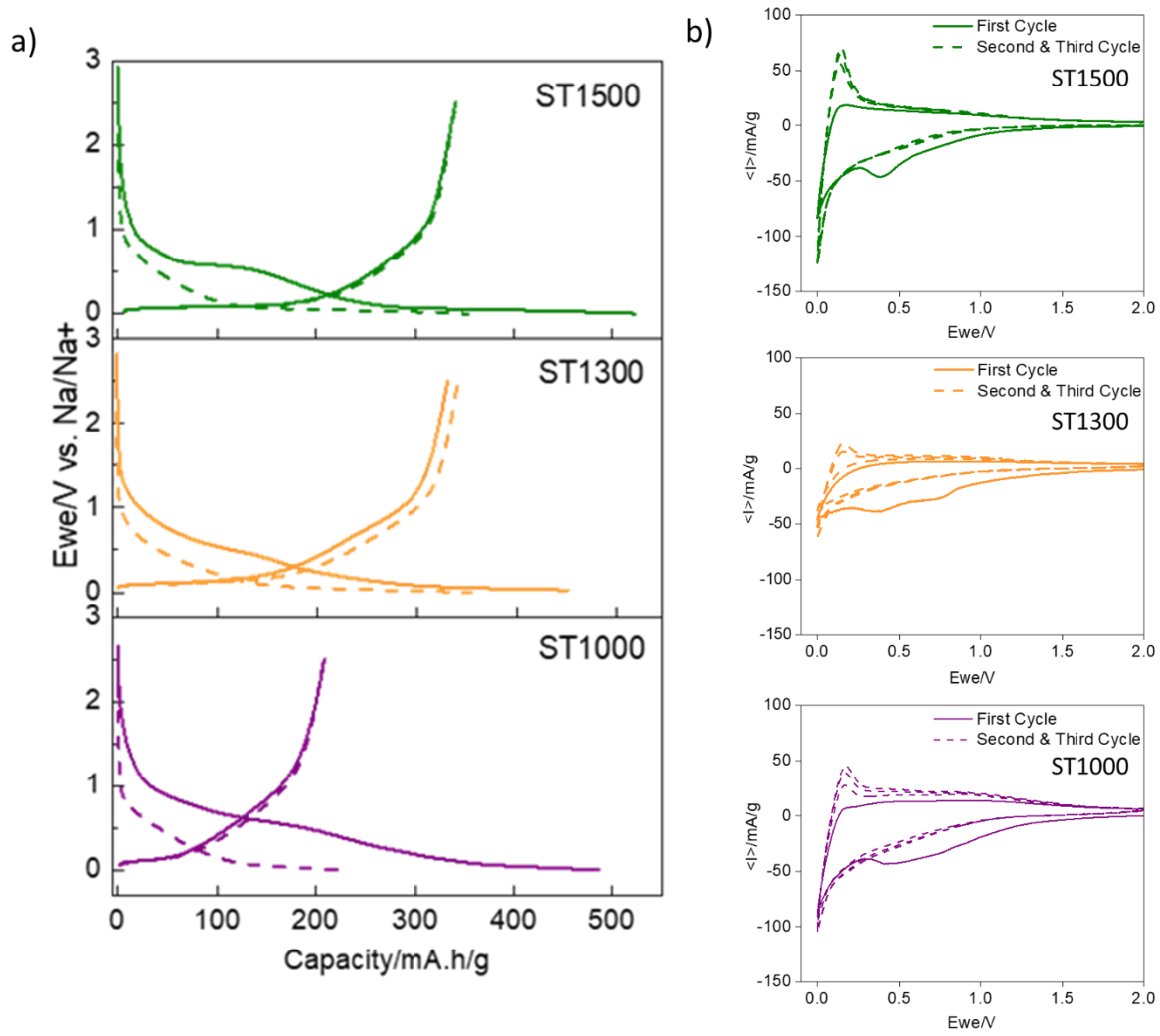


Figure 5.5 a) Galvanostatic discharge-charge profiles showing the effect of different morphology on electrochemical performance, b) Cyclic voltammetry of the first cycle and second cycle

CV for all materials were performed to discern these additional processes at 0.1 mV/s (Figure 5.5)The cathodic current is visibly larger with increasing carbonisation temperature (ST1500 > ST1000) which suggests that decreasing the surface area in our hard carbons has a positive effect, as the Na-ions are effectively stored rather than consumed in irreversible secondary reactions and trapped in the SEI during the first cycle. Accordingly, in the first CV cycles (Figure 5.5), where we expect to observe the first irreversible reactions and the SEI formation, it is possible to discern a broad peak (between 0.4 and 1 V) for ST1000 that is more defined for ST1300 (two peaks at 0.4V and 0.8 V) and for ST1500 (centred at 0.4 V). After second

cycle, cathodic peaks started to disappear, suggesting the irreversible processes happening inside cell. The rate performance was characterized at the current rates from 0.1C to 2C (Figure 5.6). All samples suffer a capacity decay at the high current rates due to the excessive polarization on the electrode. When the cycle life is compared, the ST1500 can still recover most of its initial capacity values in the following reverse process and retains 83% of the initial capacity after 200 cycles (243 mAh /g), as shown in Figure 5.6b. This long cycle life principally arises from small resistance during cycling, provided by internal mesopores of the carbon skeleton and thus the effective penetration of the electrolyte. The initial capacity discrepancies found in various cells might be attributed to the possible temperature instability of the laboratory work area. This demonstrates the significance of temperature regulation in the cell environment. Table 5.2 displays the mean capacities as well as the standard deviation of capacity.

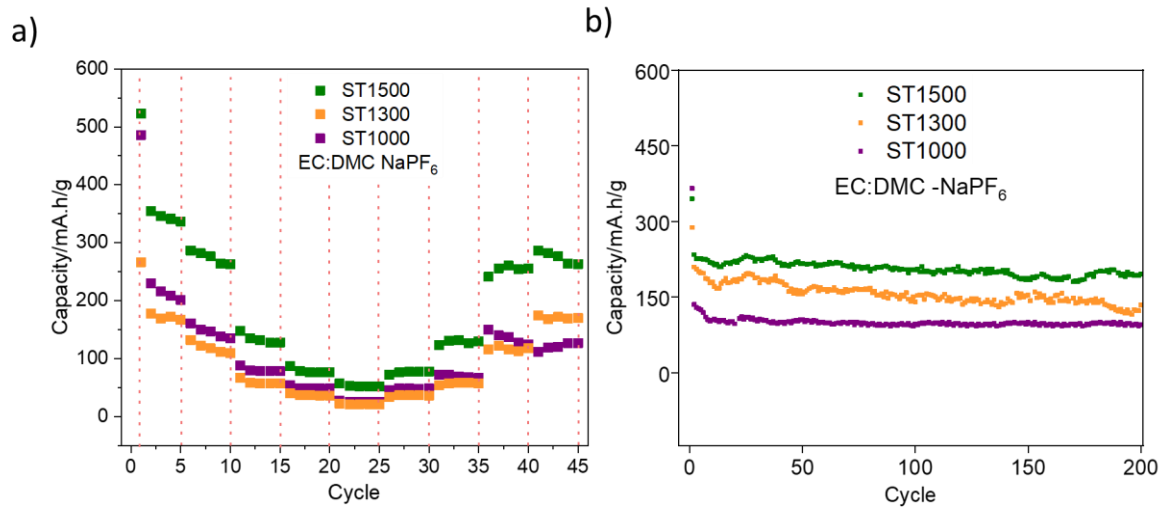


Figure 5.6 Rate performance of the discharge capacities of ST1000, ST1300, ST1500 at current densities between 30 and 600 mA/g

5.2.3 Performance Comparison of GC and ST hard carbon anode electrodes

Table 5.2 displays the pore characteristics of GC (HTC method) and ST (Soft templated method) materials obtained by N_2 gas adsorption. The specific surface area of ST samples is higher than their GC counterparts, and it decreases with the elevation of carbonization temperature for both materials. Moving from GC materials to ST materials, the pore size distributions become more concentrated at 2.5–15 nm (it is 1.5-5 nm for GC), and the open pore volume increases accordingly. This result demonstrates that solvothermal carbonization method temperature can increase the number of open pores. This is corroborating with the recent findings published by Hu et al. [274]; the existence of ethanol as a solvent enables the

microstructural changes as large steam gas produced during carbonization process may assist to open the pores.

Table 5.2 Summary of open pore characteristics obtained from N_2 adsorption, XPS and electrochemical performances. STD deviation formula used in calculations is shown in Appendix II. r is the correlation coefficient of BET measurement.

	Surface Area m^2/g (r)	**Pore Size Distribution nm**	**C/O ratio, %**	**1st cycle capacity mA h/g**	**Mean 1st cycle Capacity mA h/g**	**STD deviation mA h/g**	**2nd cycle capacity mA h/g**	**Initial Coulombic efficiency %**
GC1000	11 (0.99)		6.24	265	258	25	147	72
GC1300	4 (0.99)	1.5-5	8.61	301	290	37	243	83
GC1500	2 (0.99)		9.34	210	200	32	186	74
ST1000	181 (0.99)		1.67	487	486	46	220	45
ST1300	66 (0.99)	2.5-15	1.91	468	354	74	334	72
ST1500	21 (0.98)		2.03	525	454	40	353	67

However, the pore analyses presented above focused on open pores rather than closed pores. Therefore, the SANS technique, which detects both open and closed pores, was used, and the radius of a closed pore can be calculated by fitting the characteristic length associated with the scattering power difference.[129] According to the SANS patterns, GC materials possess closed pore diameters with the average value from 1.6 to 2 nm; whilst ST materials shows two different closed pore nature which varies from 1.8 to 2.3 nm for micropores and 25 nm to 40 nm for mesopores (Figure 5.7b).

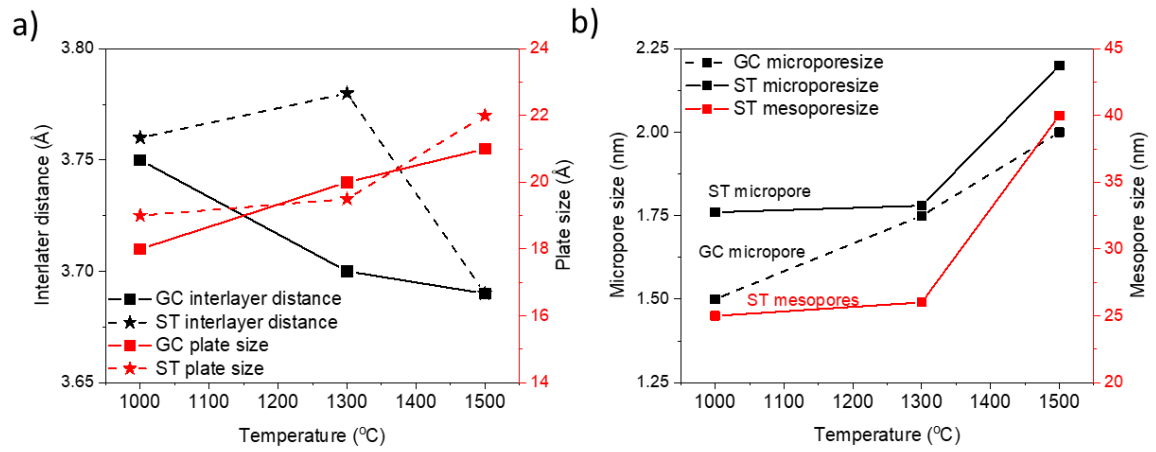


Figure 5.7 Comparison of structural properties

Total neutron scattering and WAXS measurements were used to investigate graphitic domains. As shown in Figure 5.7a, GC and ST materials mostly shows same characteristics in terms of plate size and interlayer spacings. The electrochemical properties of GC and ST carbons were investigated using half-cell tests in order to compare the influence of material microstructure on Na storage behaviour.

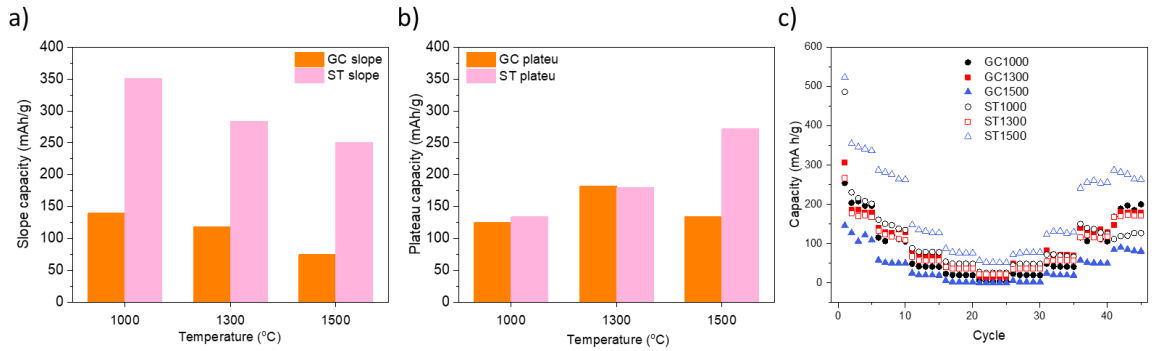


Figure 5.8 Comparison of electrochemical performance in a) sloping region and b) plateau region and c) rate performance

Table 5.1 shows the electrochemical performance of the materials in the first cycle. ST electrodes generally shows higher capacity in the first cycle however due to their higher surface area they suffer from large irreversible capacity and low first cycle coulombic efficiency. The ST1500 electrode, with its greater size and higher degree of closed pores and lower surface area and narrow open mesopores, outperforms the others in terms of rate performance (Figure 5.8). This shows that the enlarged pores favour the diffusion and storage of large radius of Na-ion. The poorest rate capability and electrochemical performance of GC1500 electrode also confirms the importance of larger closed pores, because when carbonization temperature increases, diffusion routes for ions are closed off, and some micropores become unavailable

for sodium storage, resulting in a smaller capacity. Furthermore, GC1500 and ST1500 has quite similar micropore size, plate size and interlayer spacing, however existence of larger closed pores of ST1500 enables alternative pathway for ions to reach storage sites for ST1500 and therefore improved performance. In terms of storage mechanisms, two groups of materials show distinct contributions from different voltage regions. ST materials with a larger quantity of oxygen-containing defect have a higher sloping capacity than GC materials, and this contribution is decreasing with increasing C/O ratio. It is also important to note that, higher voltage plateau region observed in the discharge profile of ST electrodes was counted as slope region contribution, however possible redox reactions occurring at that voltage might be also an indication of pore filling. Additionally, plateau capacity contributions for ST materials are increasing by increasing the size of closed pores with increased carbonization temperature. Lower carbonization temperature ST materials are predicted to have a greater contribution from the low voltage plateau region than their GC counterparts due to their larger closed pores. However, contrary to what is expected, the greatest difference in capacity contributions comes from the sloping region rather than the plateau region, as it is shown in Figure 5.8a and b. The overall findings indicate that ST1500 electrode with nearly 40 nm mesopores size shows a significant improvement in the plateau capacity; whilst the lower carbonization temperature electrodes do not have additional contribution from the large closed pores, this can be due to the large number of oxygen functional groups exist in those materials that form a thick SEI layer on the electrodes and impede the access of the closed pores.

5.3 Conclusions

In this study, mesoporous hard carbon materials were synthesized by soft templating of carbon precursors with a soft block copolymer via solvothermal carbonization and subsequent high temperatures to tune the microstructure of hard carbon anodes. The first part of this study was dedicated to the hard carbon characterizations and reveals the closed pore evolution of the hard carbons with increasing carbonization temperature. In the second part, the electrochemical performance of the hard carbon electrodes with different textural properties were measured in $NaPF_6$ EC:DMC. The ST1500 exhibits promising ion storage performance with a high reversible capacity of 334 mA h/g that can still recover most of its initial capacity values in the following reverse process and maintains 83% of the initial capacity after 200 cycles (243 mAh /g). ST1500's excellent rate efficiency and cyclability show that closed pores do optimise the structure such that the ions reach the sites where they can be deposited. It is followed by a comparative study of electrochemical performance and storage mechanism of microporous

hard carbons obtained from HTC method (in chapter 4) and soft templated hard carbons that consists of closed mesopores. Findings indicate that high surface area and surface interactions have big impact on pores accessibility and not all closed pores contribute to ion storage as well as it is predicted due to the possible SEI formation. ST1500 it shows a very large contribution compared to GC1500 to the plateau capacity. When it is compared their GC counter parts, lower carbonization temperature of ST materials show poor low voltage capacity contributions than it is expected which may be attributed to the presence of a large number of oxygen functional groups in such materials, which create a thick SEI layer on the electrodes and obstruct closed pore accessibility. Therefore, the effect of the electrode electrolyte interface on electrochemical efficiency will be addressed in the following chapter. These results will enrich the microstructure tuning strategy and provide new opportunities to develop high performance carbon anodes for NIBs.

6 ELECTRODE-ELECTROLYTE INTERFACE AND SEI FORMATION: SALT AND SOLVENT EFFECTS

6.1 Introduction

The specific capacity of batteries is mainly determined by the characteristics of the electrode active materials and therefore most of the research interest in NIBs has focused on the investigation of electrode materials. Studies dealing with the electrolyte are much rarer than those on electrodes, despite the fact that the energy density, cycle life, storage performance and reversible capacity of active materials is controlled by the choice of electrolyte and the accompanied interphase between electrode surface and electrolyte.[275,276] A good harmony between the electrolyte and electrode can boost the performance of electrode materials. Therefore, it is of crucial importance to control the microstructure of hard carbon anodes and electrolyte chemistry, and thus components of the SEI with the purpose of achieving high anode performance in NIBs. The SEI layer formed from the decomposition materials associated with the electrolyte of the battery. These decomposition materials are insoluble and can significantly vary depending on electrode morphology and the physicochemical properties of the electrolyte (dielectric constant, viscosity, conductivity, Lewis acidity/basicity) have a strong impact on their properties such as ionic transmission, stability, thickness, etc.[166,277] As is the case with solvents, experimental applications for LIBs systems were also transferred to NIBs. However, reduced electrochemical stability and high reactivity of Na metal in conventional organic electrolytes compared with Li metal can cause a detrimental distortion to the surrounding cell environment, lead to degradation of the electrolyte, and the constant disintegration and reformation of the SEI that eventually results in low Coulombic efficiency, and poor cycling life.[278,279] In this regard, investigating the effect the electrolyte components on the carbon electrode while considering the influence of the metallic sodium anode in half-cell configuration and comparison of half/full cell configuration could provide a crucial understanding toward the development of the Na ion battery systems. The poly-anion type compounds have stable 3D open framework with large interstitial channels which provides the rapid Na ion movement.[280,281] The NVPF electrode generally exhibits a high average operating potential over 3.85 V (vs. Na^+/Na) and an theoretical energy density of 507 W h k/g. [282,283] Nevertheless, the inferior electronic conductivity of 10^{-12} S cm^{-1} limits the long-term cycling stability and rate performance of NVPF, which limits its further practical applications.[233] Numerous attempts focusing on optimising electron conductivity and ion diffusion have been

made to improve the electrochemical efficiency of NVPF. Construction of composite structures with carbon-based materials have been proposed to improve electronic conductivity, prevent particle agglomeration, and ensure structural stability during cycling. These carbon-based materials can be mesoporous carbon,[283] graphene,[284] and other carbonaceous materials.[285]
In this chapter, the influence of the physicochemical properties of the electrolyte components will be evaluated. The best performing hard carbon material in the previous chapter is taken to investigate the impact of the physicochemical properties of different electrolyte components (solvent, salt anion) on the electrochemical cell performance, in terms of reversible capacity and long term cyclability. The comparison of 1M $NaPF_6$ in EC:DMC with $NaClO_4$ in EC:DMC and then with 1M $NaPF_6$ in diglyme were used to understand salt anion and solvent effect, respectively. These comparisons were proposed to relate different degrees of solvent-ion interactions (e.g., nature of Na^+ solvation, cation-pair interactions) to the battery performance through the analysis of the evolving SEI. We further demonstrate that the salt anion plays a vital role in the SEI formation process at the carbon anode and sodium metal cathode. We further investigate the electrode interface, reversibility and long term cyclability of full cell configuration with hard carbon and an NVPF/C electrode in $NaClO_4$ in EC:DMC electrolyte solution.

6.2 Results and discussion

6.2.1 Properties of bulk electrolytes

Each element of the electrolyte (salt, solvent, and additive) affects the above cell performance parameters to quite a different degree. Therefore, electrolyte optimisation is made through changing the elements of the electrolyte. The choice of sodium salt has profound effects on the ionic conductivity and electrochemical stability. The ionic conductivity (σ) of the electrolyte, which is responsible for fast and efficient ion transport even at high charge and discharge rates, is mainly affected by the strength of ion-ion interactions (the amount of charge carriers). The salt anions are also responsible for limiting the upper voltage of the ESW, while the lower limit is mainly determined by solvent reduction. The main differences between the salts used in this study are the ion mobility ($NaClO_4 > NaPF_6$), the salt dissociation constant ($NaClO_4 < NaPF_6$) and the donor number (DN, DN_{PF6-} (2.50) < DN_{ClO4-} (8.44))[148], which are the key properties that determine ionic conductivity in a given solvent (in EC:DMC, σ_{NaClO4}= 5 Scm^{-1} σ_{NaPF6}= 6.5 Scm^{-1}).[286]

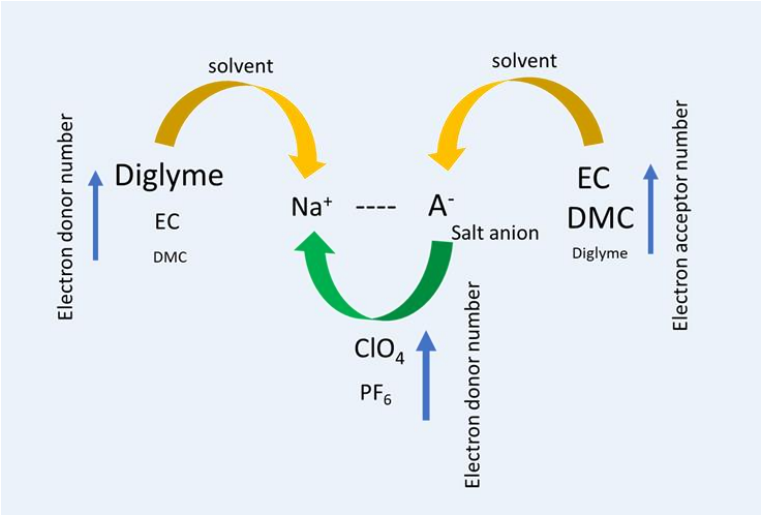


Figure 6.1 Illustration of AN and DN concept of Gutmann

Higher anion DN tends to generate stronger interaction between anion and cation, which leads to lower ionic conductivities, whilst high solvent DN allowing stronger solvation of the cation and improves cell performance. Solvation of cation plays a definitive role in the formation of a stable and protective SEI when combined with low DN anion. Diglyme has a fairly high DN compared to carbonate based solvents (DN = 19.2[287] vs. 16.4 or 17.2 for EC and DMC, respectively). Recent studies have shown that, in contrast to diglyme, EC:DMC cannot effectively keep the anion apart from the Na^+ ion during the desolvation process at the anode due to its low DN number.[288] This has been suggested to provoke capacity fading due to the continuous decomposition of the anion on the anode surface. Such observed tendencies clearly demonstrate the complex interplay of solvent-cation-anion interactions that determine the cycling behaviour of a battery.

Table 6.1 Properties of electrolyte components,

	$NaPF_6$	$NaClO_4$	EC	DMC	Diglyme
Acceptor Number [289]	-	-	18	18	9.9
Donor Number[159]	2.5	8.44	16.4	17.2	19.2
Conductivity (Scm^{-1})[286]	6.5	5	-	-	-
Dielectric Constant[290]	-	-	89.78	3.1075	7.23

Figure 6.2 compares the Raman spectra for electrolytes with different salt anion to provide further understanding about solvation and coordination structures. Higher shifts are expected for restricted vibration modes, when the solvent molecules are interacting with ions through solvation. The Raman spectra of the EC solvent mixture shows two peaks at 715 and 895 cm^{-1}solvent. According to literature, the former peak could be assigned to CH_2 rocking and

C−O stretching[291], symmetric ring deformation of EC[292,293] or C=O bending mode.[294] For $NaPF_6$ in EC:DMC, the shape of EC:DMC band became broader and less symmetric due to the peak shift of the P-F vibration.[295,296]This band shift in the 700-800 cm^{-1} region usually gives an information about solvation process: $NaPF_6$ salt is dissolved and solvated PF_6^- ions appeared in the electrolyte. Moreover, the band shift to lower wavenumber of solvated $NaPF_6$ in EC:DMC suggests that the PF_6^- anions have a high degree of mobility in EC:DMC solvent mixture compared to diglyme.[288] Due to the its high dielectric constant, EC:DMC it has a higher capability to disassociate $NaPF_6$ (ε_{EC}= 89.78, ε_{DMC}= 3.1075, $\varepsilon_{Diglyme}$= 7.23)[290]However, this ability of high mobility of PF_6^- in EC:DMC gives the anion more opportunity to contact not only with the Na^+ but it also leads to a high frequency of PF_6^- occurrence on the electrode interface.[297]

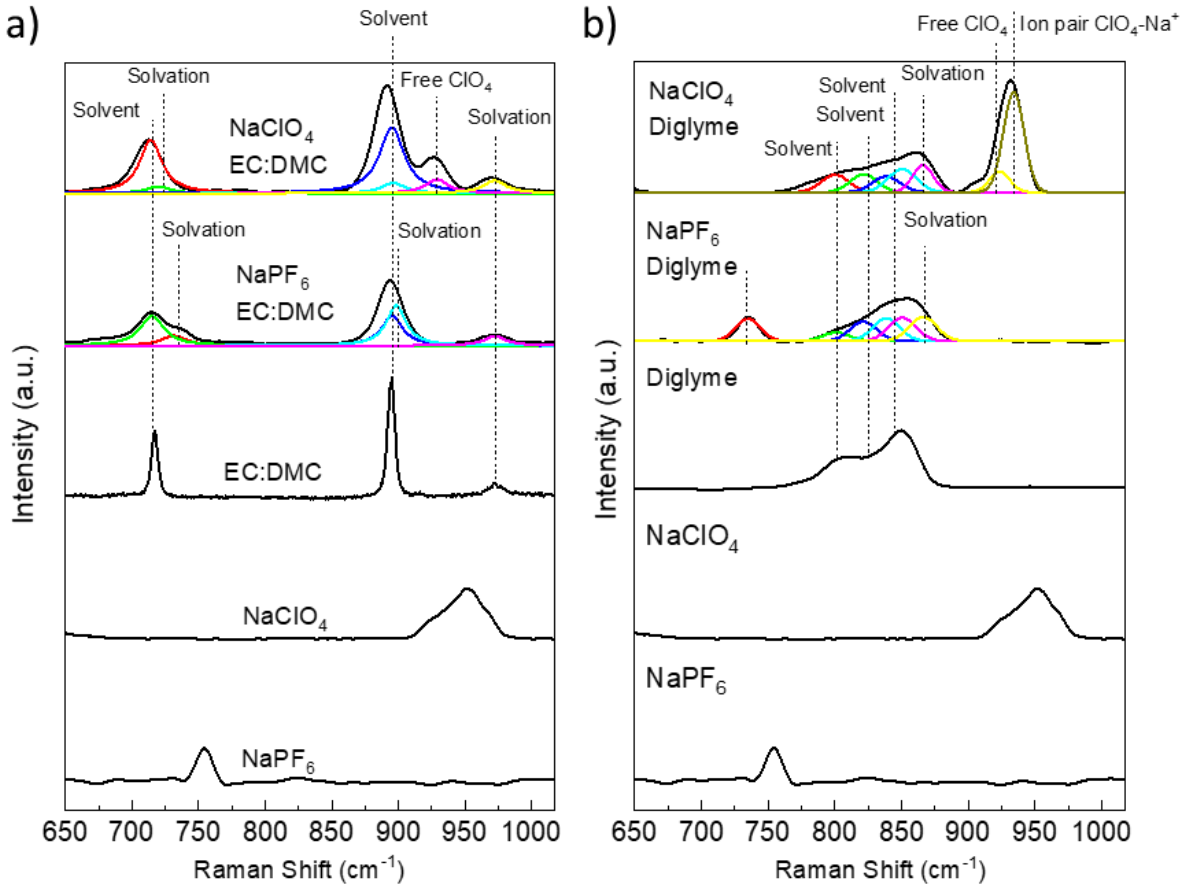


Figure 6.2 Raman spectra of CH_2 rocking/C−O stretching vibrations in a) EC:DMC b) Diglyme based electrolytes

The Raman shifts at about 892 and 969 cm^{-1} are assigned to the vibration bands of EC and DMC, both of which are accompanied by satellite peaks of cation solvation. When we compare $NaPF_6$ and $NaClO_4$ in EC:DMC electrolyte in the 920-990 cm^{-1} region, it can be seen that the

majority of ClO_4^- exists as free anions on account of the dissociation of $NaClO_4$ salt and strong Na^+ solvation ability of solvent molecules. The vibrational spectroscopy of ClO_4^- anions appears at 933 cm^{-1}. [298] Battisti et al.[292] studied ion-ion-solvent interactions of ClO_4^- anion with Raman spectroscopy and reported that there are four kinds of symmetrical stretching vibration of ClO_4^- anions in solution assigned to the following species: free anions, solvent-separated ion pairs, contact ion pairs, and multiple ion aggregates. These assignments are based on a report by James et al.[298] in which the component band analysis of the $C1O_4^-$ at various concentrations of electrolyte was investigated, and show that below 3M , there are only free anions, and that solvent-separated ion pairs contact and multiple ion aggregates are only found at higher concentrations. Therefore, considering the lower concentration of the present study, the Raman peak at 933 cm^{-1} could be interpreted as free ClO_4^- anions. The deconvolution of the broad diglyme band between 780-900 cm^{-1}, ascribed to mixed -CH_2- rocking and C-O-C stretching modes, was done following the methodology reported by Komaba et al.[299] vibrations at 862.6 and 833.8 cm^{-1} are assigned to solvating molecules whilst the bands at lower shifts 847.2, 822.51 and 801.57 cm-^{1} were ascribed to free solvent molecules. The vibrational spectroscopy of ClO_4^- appears as free anions at 933, whist contact- ion appears at 939 cm^{-1}. It is clear that these molecules are more abundant in the cell environment than the solvated sodium, based on the peak strength. Additionally, in diglyme solvents, the ClO_4^- anions can coordinate with the Na^+ competitively and exclude diglyme from the solvation structure due to the high DN of the $NaClO_4$ salt which gives rise to freer diglyme in the cell. This free solvent can ultimately lead to Na metal consumption which degrades the electrochemical performance during cycles.

6.2.2 Electrochemical performance

As shown in Figure 6.3, the $NaClO_4$ EC:DMC system presents the highest first cycle capacity but the worst long term cyclability. The first cycle capacity of the $NaPF_6$ salt is higher in EC:DMC compared to diglyme, whilst changing to diglyme improves the ICE with excellent capacity retention (~70%) after 200 cycles(Figure 6.3), suggesting the formation of a more stable SEI layer. [168] All these changes in reversible capacity, ICE and long-term cycling shows the impact of salt and solvent on the electrochemical performance (Table 6.2). Therefore, this part dedicated to understanding interface chemistry, its effect on cell performance. The main research questions of this part are to understand the reason for capacity decrease in the $NaClO_4$ EC:DMC system in the long term, and how to stabilise the capacity.

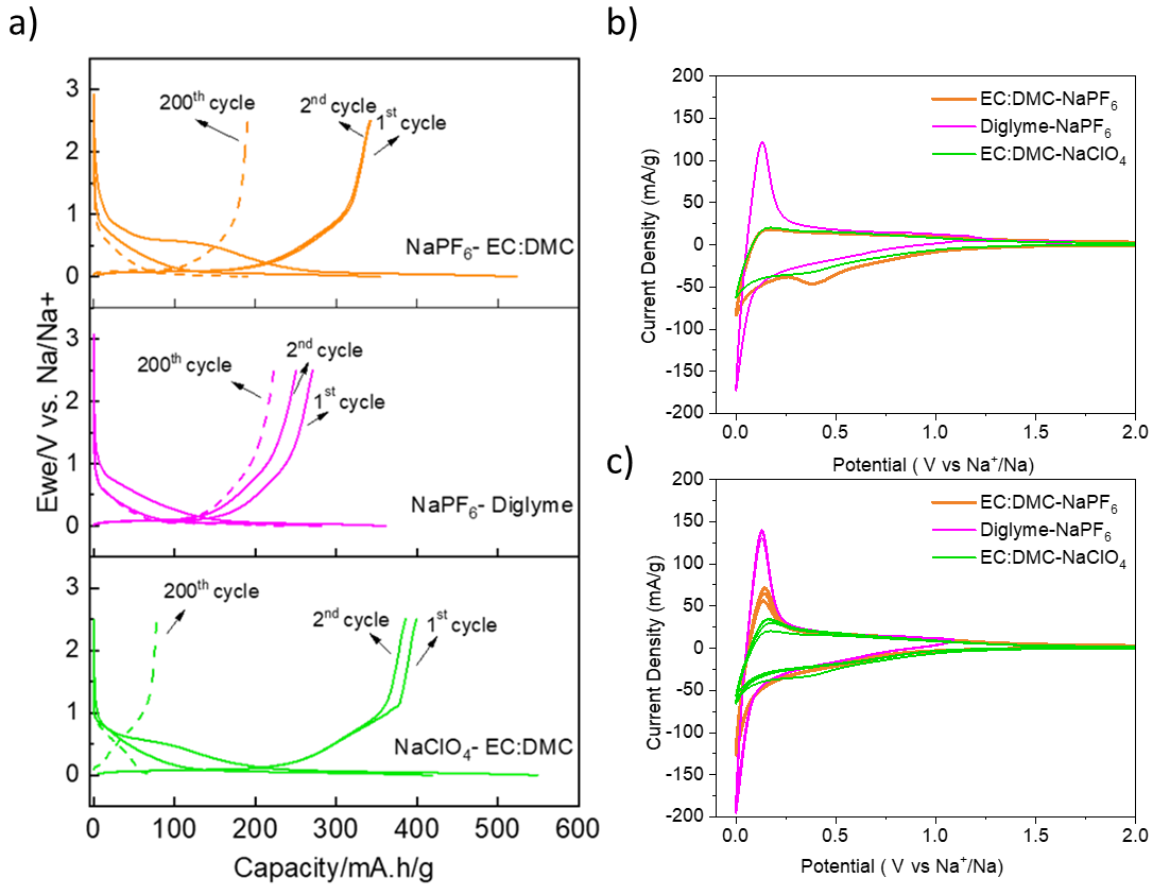


Figure 6.3 a)Galvanostatic charge/discharge profiles for ST1000-ST1500 in the first, second and 200th cycles, b) Cyclic Voltammetry of ST1500 in the first cyle c) second, third and fourth cycles cycle.

Cyclic voltammetry (CV) tests were conducted at a scanning rate of 0.1 mV s^{-1} in the voltage range of 0–2 V to understand the different electrochemical characteristics of the two solvents (Figure 6.3). Again, in diglyme, interphase formation during the first CV cycle seems to improve the charge transfer at the electrode/electrolyte interface and protect the electrode from further degradation. During the initial cathodic scan of EC:DMC with $NaPF_6$ salt, there is a broad reduction plateau around 0.4 V suggesting formation of SEI. The CV curves of the cell with diglyme solvent have sharp reduction and oxidation peaks at around 0.01 V and 0.2 V. The reduction peak is attributed to insertion of sodium ion into the voids in hard carbon, while the oxidation peak corresponds to their reversible removal from the structure.

Table 6.2 Electrochemical properties of the different salt and solvent combinations

	$NaPF_6$ EC:DMC	$NaClO_4$ EC:DMC	$NaPF_6$ Diglyme
1st cycle (mAh/g)	523	549	364
STD deviation (mAh/g)	50	53	48
2nd cycle (mAh/g)	355	419	282
ICE (%)	68	76	77
200th cycle (mAh/g)	190	77	239
Long Term Efficiency (%)	36	14	66

However, for the EC:DMC electrolyte in the first cycle, the oxidation peak is absent for this reversible ion interaction, only appearing from the second cycle onwards. This irreversible ion interaction might result from arising SEI growth during the first cycle that traps Na ions in the hard carbon structure. When comparing $NaPF_6$ with $NaClO_4$ in EC:DMC solvents, it is clear that the $NaClO_4$ electrolyte shows higher first cycle capacity and ICE% than the one with $NaPF_6$ (Figure 6.3).

6.2.3 SEI as a function of electrolyte

Characterising the contributions from solvent decomposition is critical to comprehend the nature and chemical composition of the SEI layer. ST1500 electrodes electrochemically cycled in different electrolyte system were analysed by detailed XPS measurements to reveal the SEI surface composition and its depth evolution. For this purpose, XPS detail spectra were acquired in the range of the C1s, O1s, F1s and Na1s photoelectron peaks from the pristine electrode surfaces and after sequential removal of the surface layer (by sputtering). In Figure 6.4, Compared with pristine ST1500 electrodes (Figure 6.4a), the appearance of higher intensity F, Na and O peaks observed on the surfaces of the electrodes cycled in both ether- and ester-based electrolytes show the development of SEIs with organic and inorganic species.

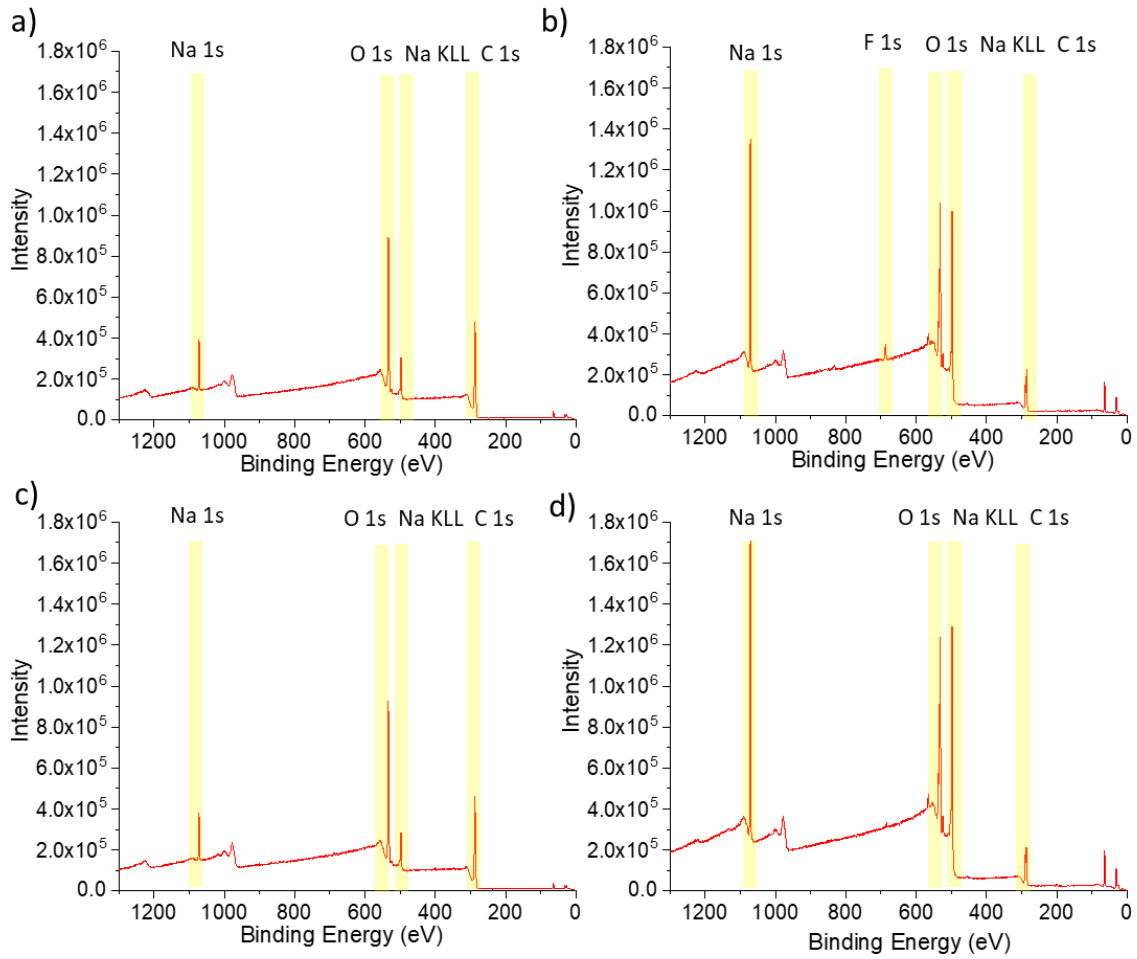


Figure 6.4 XPS survey spectra for samples: a) pristine ST1500 electrode; ST1500 electrodes cycled in b) EC:DMC- $NaPF_6$ and c) Diglyme- $NaPF_6$ and d) EC:DMC- $NaClO_4$

In Figure 6.5a, strong peak at 284.5 eV in the spectra is assigned to sp^2 carbon in hard carbon electrode, which becomes very weak after sodiation of the electrode, due to the SEI formation on the electrode surface (Figure 6.5b,c,d). Four additional peaks which exhibits at 285.0, 286.5, 288.3 and 290.5 eV can be attributed to CH_2, C–O, O=C–O and CO_3 environment of carbon, respectively. These mono-, bi-, and trioxygenated conditions of carbon are due to species resulting from solvent degradation/reduction, which have been extensively identified in the case of Li-ion cells. [300,301]The C–O environment can be attributed to alkyl carbonates (R–CH_2–OCO_2Na, or to polyethers/esters[168,302], or R–CH_2–ONa species. On the other hand, the O=C–O environment can be assigned to esters or oxalate ions,[303] while the CO_3 environment can be attributed to alkali carbonates ($NaCO_3$) and/or sodium alkyl carbonates. To obtain information on the depth profile of the SEI composition, XPS spectra were acquired for the un-sputtered sodiated samples and then, after sequential removal (30s intervals) of thin surface layers to generate a composition depth profile shown in. As shown in Figure 6.5a,b,c,d, after

sodiation of the electrodes, the sp^2 carbon peak in the C 1s spectra arising from the graphitic feature of hard carbon electrodes almost disappeared. This is an indication of a layer covering the surface of the hard carbon. When Ar^+ etching proceeds, the concentration of sp^2 carbon became higher in the C1s spectra of electrode in ether-based electrolytes before ester-based electrolytes, indicating that the electrode surface layer is thinner in ether-based electrolytes than that in ester-based electrolytes (Figure 6.5a). The C1s peak contributions shows that diglyme based electrolyte has higher degree of C-O containing organic compound on the exterior SEI and it`s percentage is decreasing in bulk electrolyte for all the electrolyte systems. It should be also considered that argon and oxygen form a strong donor–acceptor chemical bond, therefore Ar^+ sputtering might be causing the reduction of C-O bonds. Inorganic species such as sodium carbonate (Na_2CO_3) shows a sharp decrease after the first sputtering step for $NaPF_6$ EC:DMC (Figure 6.5c), whilst remaining at nearly same intensity for the $NaClO_4$ based electrolyte even after 60 s of etching (Figure 6.5c).

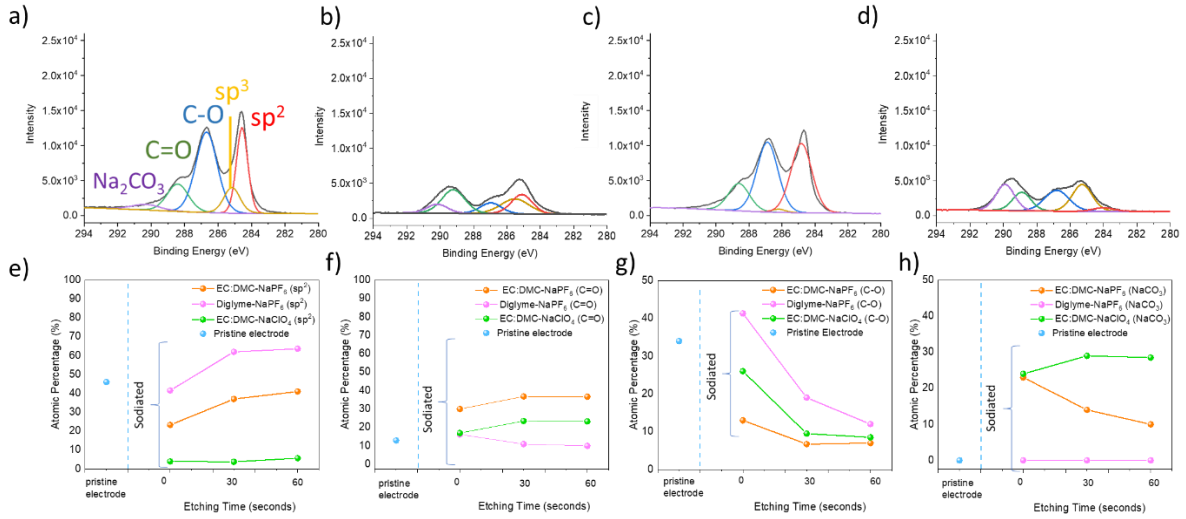


Figure 6.5 C 1s spectra of a) pristine ST1500 electrode, cycled ST1500 electrode in a) $NaPF_6$ EC:DMC b) $NaPF_6$ Diglyme c)$NaClO_4$ EC:DMC, Atomic percentage of e-h) pristine sample, cycled sampled in different electrolyte with no etching (x=0), after 30 seconds of etching (x=30), after 60 seconds of etching (x=60)

XPS O 1s spectra (Figure 6.6a,b,c,d) also support the existence of O=C–O environment, corresponding to a peak at 531.8 eV. The peak with the binding energy of 533.5 eV, which was assigned to C–O environment can be attributed to alkyl carbonates generated by the decomposition of solvent. Furthermore, the Na Auger electron peak specifically shows that the bulk of the species are sodium-based compounds. The corresponding O 1s spectra (Figure 6.6e,f,g) show that the amount of C=O bonds is increasing with etching in glyme electrodes suggests that they might arise from the electrode binder. On the other hand, for carbonates,

existence of C=O bonds can be related to electrolyte reduction products which is found in external and internal SEI. It is good to mention here the fact that some inorganics originating from the reduction of conductive salts are less conductive for sodium ion transfer and thermodynamically unstable which in the end affects electrochemical performance.

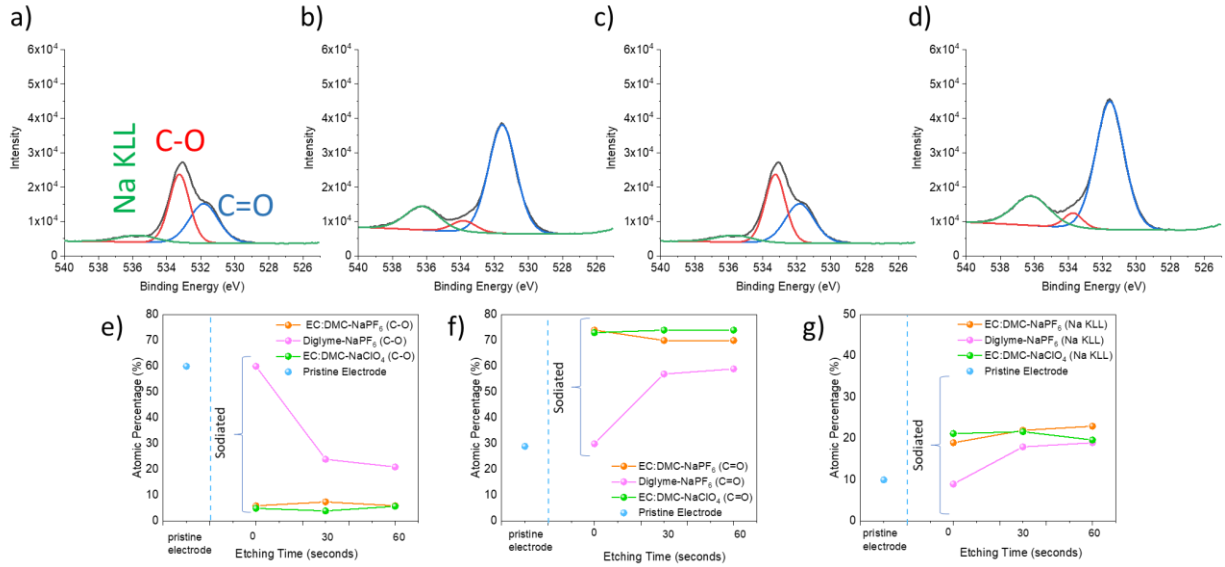


Figure 6.6 O1s spectra of a) pristine ST1500 electrode, cycled ST1500 electrode in a) $NaPF_6$ EC:DMC b) $NaPF_6$ Diglyme c)$NaClO_4$ EC:DMC Atomic percentage of e-g) pristine sample, cycled sampled in different electrolyte with no etching (x=0), after 30 seconds of etching (x=30), after 60 seconds of etching (x=60)

In ester-based electrolytes, the Na signal (Figure 6.7a) on the sodiated electrode surface shows no change over sputtering time, suggests the existence of Na-containing inorganic species such as NaF (for $NaPF_6$ salt based electrolytes), NaCl (for $NaClO_4$ salt based electrolytes), and Na_2CO_3 both on the surface and and across the SEI bulk. In the $NaPF_6$ electrolytes, the F 1s spectra (Figure 6.7) shows the Na-F signal intensity was increased by etching; suggesting SEI was formed with more Na-F inside compared to surface. Overall, it can be concluded that the SEI formed in the diglyme-based electrolyte comprises both organic and inorganic (NaF) components. Inorganics like NaF are mainly placed in bulk or internal SEI surface (close to electrode interface), on the other hand organics (polyesters (C-O), alkyl carbonates (C=O)) spread over the whole thickness of the SEI but mainly on the external SEI surface (close to electrolyte). In $NaClO_4$ based electrolytes, the structure of the SEI consists of an inorganic inner layer, composed mostly of NaCl from the electrochemical reduction of $NaClO_4$, and a carbonate-rich outermost shell originated from the decomposition of the organics (Figure 6.7c). NaCl leads to non-conductive SEI, enabling further degradation of the SEI upon subsequent cycles. It should be also mentioned here that the SEI was never completely removed by the

sputtering process. This may be related to the open and defective turbostratic structure of hard carbon, where the SEI is not only restricted to the superficial region but also penetrates the entire electrode structure.

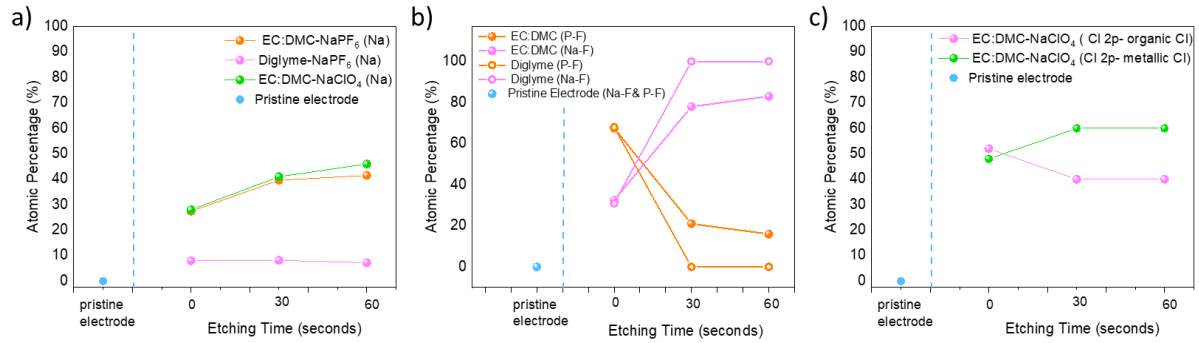


Figure 6.7 a) Na 1s, b) F1s and Cl 2p spectra of pristine ST1500 electrode, cycled ST1500 electrode in different electrolyte (x=0), after 30 seconds of etching (x=30), after 60 seconds of etching (x=60)

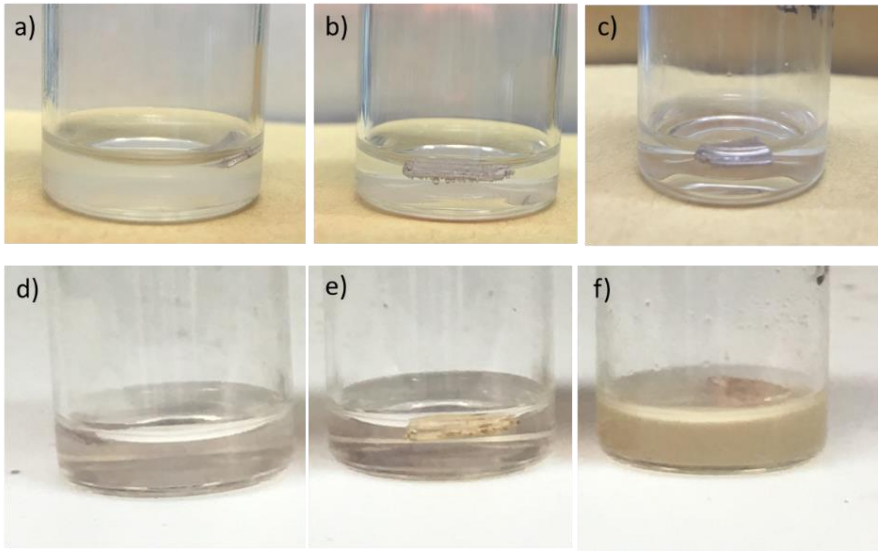


Figure 6.8 Na metal in electrolytes a) $NaPF_6$ EC:DMC b) NaPF6 Diglyme c) NaClO4 EC:DMC right after Na addition, in d) $NaPF_6$ EC:DMC e) $NaClO_4$ Diglyme f) $NaClO_4$ EC:DMC after 4 days.

When metallic sodium was immersed in EC:DMC with $NaPF_6$ a cloudy solution was observed, while for $NaPF_6$ in diglyme and $NaClO_4$ in EC:DMC, originally greater solubility was observed. After 4 days, in the case of $NaClO_4$ electrolyte, the corrosion reactions were so severe leading to dissolution of the sodium metal over time, as can be observed from the colour change of the electrolyte (Figure 6.8f). These observations show that decomposition of the sodium metal and the electrolyte can take place very rapidly even without electrochemical cycling. To gain more insight into the chemical composition of the decomposition products on the metallic Na, the electrode surface was further analysed by XPS. Metallic Na anodes in the investigated electrolytes were electrochemically tested in half-cell configuration. The F1s core level spectra

in Figure 6.9 verify the presence of salt anion decomposition products in all analysed SEIs, indicating the importance of the anion in the decomposition process. The signal at 684.0 eV and 687.4 eV refer to NaF[152,304] and respectively. For $NaPF_6$ salt-based electrolytes, the NaF which is a decomposition product from the salt, only appeared after etching, suggesting its major presence in the interior of the SEI. Additionally, the presence of F–C (sp^2) at 687.2 eV only in both EC:DMC and diglyme might result from a reaction between surface defects on hard carbon and decomposition products of the salt..[168]

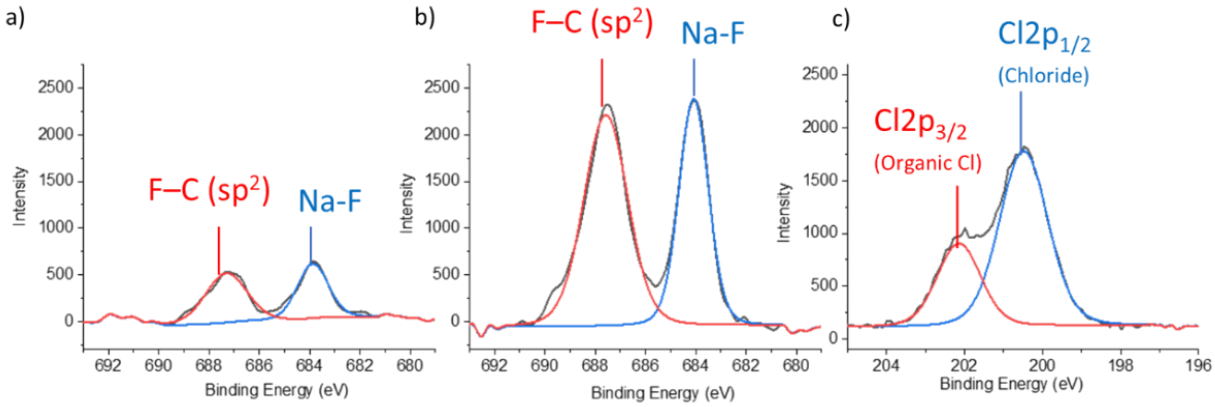


Figure 6.9 F1 s spectra of the surface of metallic sodium cathode aged a) in $NaPF_6$ EC:DMC b) in $NaPF_6$ Diglyme and c) Cl 2p spectra of ST1500 discharged electrode in $NaClO_4$ EC:DMC

For the $NaClO_4$ based system, the presence of NaCl (200.5eV) and other organic salt degradation products (202.1 eV) are observed (Figure 6.9). It has been shown that decomposition of $NaClO_4$ on the Na metal surface leads to a less stable interlayer.[305] The influence of $NaClO_4$ salt on the Na metal has indeed been observed in earlier studies on Na-air batteries where the use of ClO_4^- resulted in the formation of NaCl.[148] They claimed that because NaCl has a weaker bond than NaF due to the higher electronegativity of the F^- anion, and this weak bond leads to a less protective and more degradable, less stable SEI on the metallic Na surface. Furthermore, fluorides have been linked to the formation of uniform and stable SEIs both on metallic counter electrodes and different types of anodes. [306–308] Therefore, colossal capacity fading with the $NaClO_4$/EC:DMC system can be also related to decomposition products occurs on metallic Na counter electrode.

6.2.4 Half/Full cell comparison

It is worth noting that having metallic Na in the system implies that, apart from the irreversible reactions occurring at the surface of our carbons and the formation of the SEI, we should also consider that decomposition of solvents might be more pronounced at the highly reducing surface of Na, which can lead to poor cyclability. Accordingly, the cathodic peak in the CV

measurements (Figure 6.3) of the $NaPF_6$-based electrolytes linked to Na^+ adsorption becomes slightly larger for each material in the second cycle onwards but it is not observed for the $NaClO_4$ based electrolyte. This suggests that the resistivity of the interfaces is linked to the SEI formed on the metallic Na counter electrode. The differences between SEI formation in these electrolytes can also be visually seen when looking at metallic sodium aged in the electrolytes for 4 days (Figure 6.8) To eliminate the effect of metallic Na counter electrode and its SEI on the electrochemical process, full cell testing was conducted.

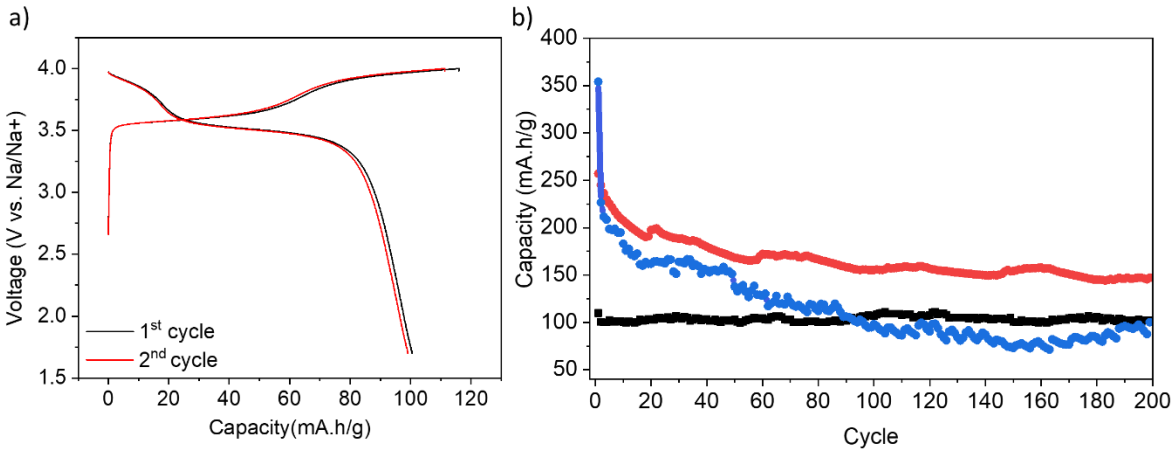


Figure 6.10 a)Activation and pre-charging of NVPF/C material. Typical discharge/charge profile of a Na-ion half-cell using NVPF/C as cathode, Na metal as anode and 1 M NaClO4 in EC:DMC as electrolyte, b) Long-term cycling performance of full cell ST1500// NVPF/C (red line),half-cell ST1500 (blue line) and half-cell NVPF/C (black line)

For that, a full cell was assembled consisting of the hard carbon negative and the NVPF/C positive electrodes in 1M $NaClO_4$ EC:DMC. The mass balance of the cell was found to be optimum at a ratio of 3:1 in agreement with reversible capacities of 300 mA h/ g and 108 mA h/ g for anode and cathode electrodes, respectively (Figure 6.10a). Compared to ST1500/Na metal cells, ST1500-NVPF/C cells exhibited much better stability in long term cyclic performance, and the capacity retention after 200 cycles is >50% (for ST1500/Na metal cell, 28%)(Figure 6.10b). After the electrochemical tests in the $NaClO_4$ solution, cell was disassembled and then *ex-situ* XPS with Ar^+ etching conducted. Figure 6.11 shows the compositions of the SEI layer at different depths obtained by analysis of the XPS spectra. The C 1s spectra show that the percentage of electrolyte decomposition products in bulk and the surface SEI of full cell is negligible. The most significant feature shown in O 1s spectra of full cell is that, the concentration of Na KLL (Na-containing inorganic species such as Na_2O) increases clearly with increasing etching depth, while the composition of C-O (from organic polymers) shows a completely opposite trend with etching depth in the SEI formed in the full

cell configuration. The measurement confirms that the organic species are mainly distributed near the SEI/ electrolyte surface while the interior of the SEI is mainly composed of inorganic species in the full cell anode. The interior SEI made of mostly inorganic Na_2O which are highly resistant to electrolyte solvent and conductive creates a stable thin film which is resulting in low charge transfer resistance and energy barrier at the electrode interface.[309] On the other hand, the exterior part of the SEI mainly consists of thin organic polymers which can significantly decrease the diffusion length of sodium ions and prevent extra decomposition of the electrolyte.[168]

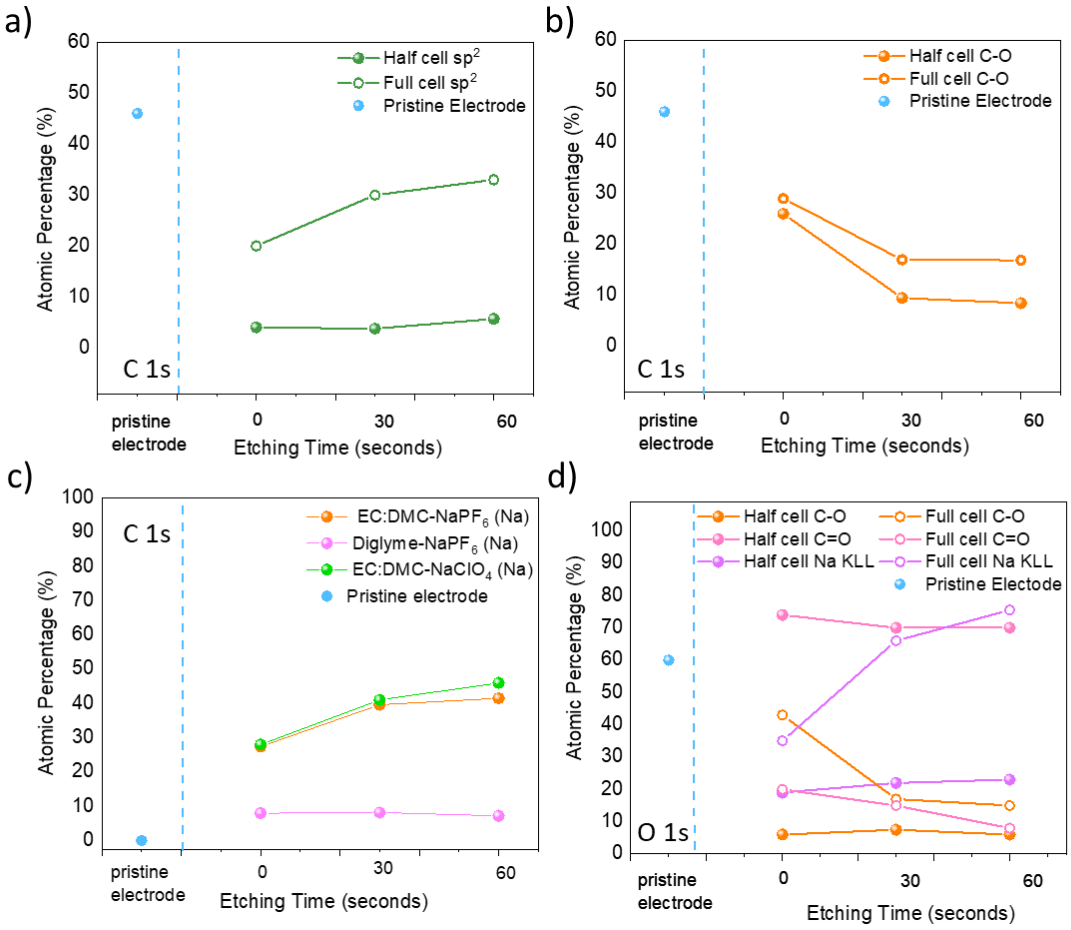


Figure 6.11 The atomic fractions calculated from the XPS a-c) C1s spectra and d) O 1s spectra of the hard carbon anode cycled in 1M $NaClO_4$ EC:DMC.

6.3 Conclusions

In this study, mesoporous hard carbon materials were synthesized by soft templating of carbon precursors with a soft block copolymer via solvothermal carbonization and subsequent high temperature. A comparative study of electrolytes was presented, ST1500 electrode (the highest performance electrode in chapter 5 was taken to investigate the impact of the physicochemical properties of electrolyte components (solvent, salt anion) on the electrochemical cell

performance, specifically reversible capacity and long term cyclability. Among the electrolyte systems, $NaClO_4$ shows the highest first and second cycle capacity, though this performance does not continue when compared over 200 cycles. This also shows the importance of reporting more than two cycles in the field as results might be misleading without showing the long-term capability of the different electrode or electrolyte systems. Solvation abilities of different electrolytes were investigated by Raman spectroscopy and it shows that in carbonate-based electrolytes, $NaClO_4$ shows stretching vibrations of free anions, ClO_4 which then effects the surface chemistry of the electrodes; whilst in the glyme based $NaClO_4$ counterparts, stretching vibrations of contact ion pair is observed. This means that the $ClO4^-$ anions can coordinate with the Na^+ competitively and exclude diglyme from the solvation structure, giving rise to freer diglyme in the cell. This free solvent can ultimately lead to Na metal consumption which degrades the electrochemical performance during cycles. This explains the why electrochemical tests of this systems fail and cannot be completed experimentally. In glyme based $NaPF_6$ electrolytes, stretching vibrations of contact ion pair is observed which is supposed to have a detrimental impact on system performance; however, $NaPF_6$-based electrolytes have the most robust cycling efficiency. The same solvent with different salt anions demonstrated the most distinct electrochemical results. Therefore, this study further investigate SEI chemistry an demonstrate that the salt anion plays a vital role in the SEI formation process at the hard carbon as well as sodium metal where less protective, conductive and more degradable layer is found for $NaClO_4$/EC:DMC systems.

The chemistry and composition of the SEI layer are found to be crucial for charge transfer, with organic species produced in the external SEI with some inorganic species occurs more closer to electrode interface to favour resistivity, conductivity and stability of thin film. Additionally, employing metallic sodium anodes and the unstable decomposition layer occurred on its surface therefore shows its damaging consequences for the long-term cycling performance of batteries. A full cell configuration was assembled consisting of the hard carbon negative and the NVPF/C positive electrodes and tested in 1M $NaClO_4$ EC:DMC. Surface analysis of the hard carbon with Ar^+ etching shows more resistant SEI layer distribution with low charge transfer resistance compared to half-cell counterparts. The corresponding research for the design of the electrolyte and electrochemical optimization will grow in importance in forthcoming years, as the outcomes of this study will contribute to machine learning models and will benefit finding hidden patterns of the interfaces to understand the big picture of the electrochemical cell.

7 CONCLUSIONS & FUTURE WORK

In this thesis, an extensive and in-depth analysis in understanding and designing of sustainable hard carbon materials and engineering the electrode-electrolyte interfaces for sodium-ion batteries has been carried out. Different aspects of hard carbon anode materials were studied in a holistic way. In the first chapter of this work, a series of hard carbons was prepared by hydrothermal carbonisation of glucose followed by high temperature carbonization and the effect of structural transformation of the carbon on the ion storage mechanism was investigated. Experimental results supported by computational calculations established a relationship between defect concentration, interlayer spacing, porosity and electrochemical behaviour of the electrode and shows that sodium intercalation ability increases with increasing interlayer distance, while oxygen-containing surface defects improve the sloping region capacity, as demonstrated with the expansion of electrode analysed by *in-situ* electrochemical dilatometry. At the same time, enhanced plateau region capacity was observed by increasing the number and size of the closed pores confirming the pore filling occurs during the low voltage plateau region. Closed pores were therefore found to be the significantly important for sodium storage during low voltage plateau region. Therefore, a suitable closed porous framework within the hard carbon structure is essential for high storage capacity. In the second chapter of this thesis, the soft templating method has been used in the formation of closed mesopores within the hard carbon, to improve and investigate the closed pore contribution to the cell performance. ST1500's excellent rate efficiency and cyclability show that closed pores optimise the structure such that the ions reach the sites where they can be deposited. Then, a comparative study of electrochemical performance and storage mechanism of hard carbons obtained from HTC method (in chapter 4) with native closed micro porosity and soft templated hard carbons that consists of templated closed mesopores is reported. ST1500 shows a very large contribution to plateau capacity compared to GC1500. Poor plateau capacity contributions of lower carbonization temperature of ST materials may be attributed to the presence of a large number of oxygen functional groups in such materials, which create a thick SEI layer on the electrodes and obstruct closed pore accessibility. This thesis then focuses on the understanding of the electrode interface and investigation of the electrolyte interphase chemistry, as the electrode interface is the gate for sodium uptake and further bulk diffusion. The optimization of the physiochemistry of electrolyte components plays a critical role in the enhancement of the chemistry of electrolyte interphase as well as the electrochemical performance of the cell. Here, in Chapter 6 , the effect of physicochemical properties of the solvent and salt anion in the

process of electrolyte decomposition were demonstrated by comparing most common solvents and salts in the literature. We further investigate SEI chemistry an demonstrate that the salt anion plays a vital role in the SEI formation process at the hard carbon as well as sodium metal where less protective, conductive and more degradable layer is found for $NaClO_4$/EC:DMC systems. A full cell configuration was assembled consisting of the hard carbon negative and the NVPF/C positive electrodes and tested in 1M $NaClO_4$ EC:DMC. Surface analysis of the hard carbon with Ar^+ etching shows more resistant SEI layer distribution with low charge transfer resistance compared to half-cell counterparts. The chemistry and composition of the SEI layer are found to be crucial for charge transfer, with organic species produced in the external SEI with some inorganic species occurs more closer to electrode interface to favour resistivity, conductivity and stability of thin film. This research suggests that rational understanding engineering of SEI is critical to achieving high rate and long-term cycling of electrode materials for NIBs through optimal electrolyte design.

In this study, the experimental full-cell experiments were conducted in coin-cell format. Further research in pouch and cylindrical cells could provide useful measurements for assessing the realistic operation of sodium-ion batteries with hard carbon anodes. Furthermore, due to time constraints and Covid-19 limitations, designed experiments on tin-hard carbon alloy anodes could not be completed and included in this thesis. In this planned work, hard carbons with different morphology was used as a volume controlling matrix and different choice of binder systems are applied to enhance cycling stability and rate capability. This work as a future work is planned to be completed. It should be considered in the future work for NIBs research community that NIBs were ultimately designed to be used in large-scale grid-level storage rather than electrical vehicles and portable electronics. The critical field of study in NIBs is determining how to maximize cycle life and increase efficiency in the first cycle. As a result, it is not most critical that these batteries are not lightweight, portable or energy dense. The most critical thing is that they are able to last a long time and are cheap. Therefore, it may be useful to explore the scientific interests in long-life batteries, non-degradable electrolytes, and even solid-state electrolytes. More research is needed to extend the study of the sodium hard carbon system to other carbons with controlled structures and provide additional data in favour of or against the suggested sodium insertion mechanisms and interface interactions. However, what is important than producing new data is that thoroughly review and analyse the data present in the literature right now and find out statically meaningful patterns. This would

be a brilliant idea, because it would certainly provide insightful results to direct and design new experiments in the field.

8 REFERENCES

[1] D. Larcher, J.-M. Tarascon, *Nat. Chem.* **2015**, *7*, 19.

[2] N. S. Lewis, *MRS Bull.* **2007**, *32*, 808.

[3] International Energy Agency, *Key World Energy Statistics*, **2019**.

[4] BP, *BP Statistical Review of World Energy*, **2019**.

[5] BP, *BP Statistical Review of World Energy*, **2020**.

[6] "Energy Consumption in the UK," **2020**.

[7] R. G. Newell, D. Raimi, S. Villanueva, B. Prest, *Global Energy Outlook*, **2020**.

[8] International Energy Agency, *CO2 Emissions from Fuel Combustion: Overview*, **2020**.

[9] International Energy Agency, *The CO2 Emissions Challenge-The Role of CCUS in Low-Carbon Power Systems*, **2021**.

[10] United Nations Framework Convention on Climate Change, *Adoption of the Paris Agreement*, **2015**.

[11] *Climate Change Act*, Statute Law Database, **2008**.

[12] *The Sixth Carbon Budget The UK's Path to Net Zero*, **2020**.

[13] E. & I. S. Department for Business, *UK Greenhouse Gas Emissions, Final Figures*, **2019**.

[14] "Provisional UK greenhouse gas emissions national statistics," **2019**.

[15] *Modelling 2050: Electricity System Analysis*, **2020**.

[16] Climate Change Committee, *The Sixth Carbon Budget Methodology Report*, **2020**.

[17] International Energy Agency, *CO2 Emissions from Fuel Combustion- Highlights*, **2019**.

[18] P. Denholm, E. Ela, B. Kirby, M. Milligan, *The Role of Energy Storage with Renewable Electricity Generation*, **2010**.

[19] H. Pan, Y. S. Hu, L. Chen, *Energy Environ. Sci.* **2013**, *6*, 2338.

[20] World Economic Forum, *A Vision for a Sustainable Battery Value Chain in 2030 Unlocking the Full Potential to Power Sustainable Development and Climate Change Mitigation*, **2019**.

[21] International Energy Agency, *Innovation in Batteries and Electricity Storage*, **2020**.

[22] Y. Kim, K. H. Ha, S. M. Oh, K. T. Lee, *Chem. - A Eur. J.* **2014**, *20*, 11980.

[23] Y. Liang, C.-Z. Zhao, H. Yuan, Y. Chen, W. Zhang, J.-Q. Huang, D. Yu, Y. Liu, M.-M. Titirici, Y.-L. Chueh, H. Yu, Q. Zhang, **2019**.

[24] K. Edström, R. Dominko, M. Fichtner, S. Perraud, C. Punckt, P. Asinari, I. Eligio Castelli, R. Chistensen, S. Clark, A. Grimaud, K. Hermansson, A. Heuer, H. Lorrmann,

O. Martin, L. Tejs Vegge, W. Wenzel, P. Bayle-Guillemaud, J. Behm, E. Berg, A. Grimaud, M. Hahlin, S. Hartmann, A. Latz, S. Lyonnard, J. Amici, M. Berecibar, S. Bodoardo, L. Jabbour, J. Kallo, E. Elyssée Paillard, *Inventing the Sustainable Batteries of the Future*, Brussels, Belgium, **2020**.

[25] G. A. Elia, K. Marquardt, K. Hoeppner, S. Fantini, R. Lin, E. Knipping, W. Peters, J.-F. Drillet, S. Passerini, R. Hahn, *Adv. Mater.* **2016**, *28*, 7564.

[26] C. P. Grey, J. M. Tarascon, *Nat. Mater.* **2017**, *16*, 45.

[27] D. Saurel, B. Orayech, B. Xiao, D. Carriazo, X. Li, **2018**, *1703268*, 1.

[28] J.-Y. Hwang, S.-T. Myung, Y.-K. Sun, *Chem. Soc. Rev.* **2017**, *46*, 3529.

[29] K. Chayambuka, G. Mulder, D. L. Danilov, P. H. L Notten, *From Li-Ion Batteries toward Na-Ion Chemistries: Challenges and Opportunities*, **2020**.

[30] W. Luo, F. Shen, C. Bommier, H. Zhu, X. Ji, L. Hu, *Acc. Chem. Res.* **2016**, *49*, 231.

[31] D. A. Stevens, J. R. Dahn, *J. Electrochem. Soc.* **2001**, *148*, A803.

[32] P. Thomas, D. Billaud, *Electrochim. Acta* **2002**, *47*, 3303.

[33] X. Dou, I. Hasa, D. Saurel, C. Vaalma, L. Wu, D. Buchholz, D. Bresser, S. Komaba, S. Passerini, *Mater. Today* **2019**, *23*, 87.

[34] J. M. Stratford, P. K. Allan, O. Pecher, P. A. Chater, C. P. Grey, *Chem. Commun.* **2016**, *52*, 12430.

[35] C. Bommier, W. Luo, W. Y. Gao, A. Greaney, S. Ma, X. Ji, *Carbon N. Y.* **2014**, *76*, 165.

[36] H. Au, H. Alptekin, A. C. S. Jensen, E. Olsson, C. A. O'Keefe, T. Smith, M. Crespo-Ribadeneyra, T. F. Headen, C. P. Grey, Q. Cai, A. J. Drew, M. M. Titirici, *Energy Environ. Sci.* **2020**, *13*, 3469.

[37] C. Matei Ghimbeu, J. Górka, V. Simone, L. Simonin, S. Martinet, C. Vix-Guterl, *Nano Energy* **2018**, *44*, 327.

[38] J. Fondard, E. Irisarri, C. Courrèges, M. R. Palacin, A. Ponrouch, R. Dedryvère, *J. Electrochem. Soc.* **2020**, *167*, 070526.

[39] G. G. Eshetu, S. Grugeon, H. Kim, S. Jeong, L. Wu, G. Gachot, S. Laruelle, M. Armand, S. Passerini, *ChemSusChem* **2016**, *9*, 462.

[40] E. Peled, *J. Electrochem. Soc.* **1979**, *126*, 2047.

[41] C. Yan, R. Xu, Y. Xiao, J. Ding, L. Xu, B. Li, J. Huang, *Adv. Funct. Mater.* **2020**, *30*, 1909887.

[42] G. Pancaldi, *Volta: Science and Culture in the Age of Enlightenment*, Princeton University Press, **2005**.

[43] D. Pavlov, *Lead-Acid Batteries: Science and Technology*, **2011**.

[44] K. Desmond, *Innovators in Battery Technology: Profiles of 95 Influential Electrochemists*, **2016**.

[45] R. M. Dell, D. A. J. Rand, in *Underst. Batter.*, Royal Society Of Chemistry, **2001**, p. 387.

[46] Bobba S, Claudiu P, Huygens D, Alves-Dias P, Gawlik B, Tzimas E, Wittmer D, Nuss P, Grohol M, Saveyn H, Buraoui F., *Report on Critical Raw Materials and the Circular Economy*, **2018**.

[47] B. Diouf, R. Pode, *Renew. Energy* **2015**, *76*, 375.

[48] M. Stecca, L. Ramirez Elizondo, T. Batista Soeiro, P. Bauer, P. Palensky, *IEEE Open J. Ind. Electron. Soc.* **2020**, 1.

[49] Tsiropoulos I, Tarvydas D, Lebedeva N., "Li-ion batteries for mobility and stationary storage applications scenarios for costs and market growth," **2018**.

[50] M. S. Whittingham, **1976**, *192*, 1126.

[51] R. M. Dell, D. A. J. D. Rand, *Understanding Batteries*, Royal Society Of Chemistry, Cambridge, **2001**.

[52] D. W. Murphy, F. A. Trumbore, *J. Electrochem. Soc.* **1976**, *123*, 960.

[53] M. A. Py, R. R. Haering, *Artic. Can. J. Phys.* **1983**, *61*, 76.

[54] J. R. Akridge, H. Vourlis, *Solid State Ionics* **1988**, *28–30*, 841.

[55] J. Akridge, H. Vourlis, *Solid State Ionics* **1986**, *18–19*, 1082.

[56] R. Yazami, P. Touzain, *J. Power Sources* **1983**, *9*, 365.

[57] T. Nagaura, M. Nagamine, I. Tanabe, N. Miyamoto, *Prog Batter. Sol Cells* **1989**, *8*, 84.

[58] T Nagaura -, *Prog. Batter. Sol. Cells* **1990**, *9*, 209.

[59] M. M. Thackeray, C. Wolverton, E. D. Isaacs, *Energy Environ. Sci.* **2012**, *5*, 7854.

[60] P. W. Gruber, P. A. Medina, G. A. Keoleian, S. E. Kesler, M. P. Everson, T. J. Wallington, *J. Ind. Ecol.* **2011**, *15*, 760.

[61] H. Pan, Y.-S. Hu, L. Chen, *Energy Environ. Sci.* **2018**, *6*, 2338.

[62] U.S. Department of the Interior, *Mineral Commodity Summaries- Geological Survey Lithium*, **2020**.

[63] B. Nykvist, M. Nilsson, *Nat. Clim. Chang.* **2015**, *5*, 329.

[64] Amnesty international, *"This Is What We Die for,"* **2016**.

[65] M. Armand, J. M. Tarascon, *Nature* **2008**, *451*, 652.

[66] J. M. Tarascon, *Nat. Chem.* **2010**, *2*, 510.

[67] K. Mizushima, P. C. Jones, P. J. Wiseman, J. B. Goodenough, *Mater. Res. Bull.* **1980**, *15*, 783.

[68] M. S. Whittingham, *Science (80-.).* **1976**, *192*, 1126.

[69] D. A. Stevens, J. R. Dahn, *J. Electrochem. Soc.* **2000**, *147*, 1271.

[70] D. A. Stevens, J. R. Dahn, *J. Electrochem. Soc.* **2001**, *148*, A803.

[71] R. D. Shannon, *Acta Crystallogr. Sect. A* **1976**, *32*, 751.

[72] K. K. Kundu, A. K. Rakshit, M. N. Das, *Electrochim. Acta* **1972**, *17*, 1921.

[73] H. Hou, X. Qiu, W. Wei, Y. Zhang, X. Ji, *Adv. Energy Mater.* **2017**, *7*, DOI 10.1002/aenm.201602898.

[74] A. C. S. Jensen, E. Olsson, H. Au, H. Alptekin, Z. Yang, S. Cottrell, K. Yokoyama, Q. Cai, M. M. Titirici, A. J. Drew, *J. Mater. Chem. A* **2020**, *8*, 743.

[75] J. Peters, D. Buchholz, S. Passerini, M. Weil, *Energy Environ. Sci.* **2016**, *9*, 1744.

[76] H. Hou, X. Qiu, W. Wei, Y. Zhang, X. Ji, *Carbon Anode Materials for Advanced Sodium-Ion Batteries*, **2017**.

[77] D. Y. W. Yu, P. V. Prikhodchenko, C. W. Mason, S. K. Batabyal, J. Gun, S. Sladkevich, A. G. Medvedev, O. Lev, *Nat. Commun.* **2013**, *4*, 1.

[78] N. Yabuuchi, K. Kubota, M. Dahbi, S. Komaba, *Chem. Rev.* **2014**, *114*, 11636.

[79] P. Barpanda, G. Oyama, S. I. Nishimura, S. C. Chung, A. Yamada, *Nat. Commun.* **2014**, *5*, 1.

[80] C. Deng, S. Zhang, B. Zhao, *Energy Storage Mater.* **2016**, *4*, 71.

[81] A. Bauer, J. Song, S. Vail, W. Pan, J. Barker, Y. Lu, *Adv. Energy Mater.* **2018**, *8*.

[82] J. Ayre, "18650 Sodium-Ion Battery Developed At RS2E," can be found under https://cleantechnica.com/2015/12/01/18650-sodium-ion-battery-developed-at-rs2e/, **2015**.

[83] J. M. Tarascon, *Joule* **2020**, *4*, 1616.

[84] R. Xiaohui, L. Yaxiang, Q. Xingguo, *Energy Storage Sci. Technol.* **2020**, *9*, 515.

[85] A. Mauger, C. M. Julien, *Materials (Basel).* **2020**, *13*, 3453.

[86] C. Vaalma, D. Buchholz, M. Weil, S. P. Materials, *Nat. Rev. Mater.* **2018**, *3*.

[87] R. A. Huggins, *Advanced Batteries: Materials Science Aspects*, Springer US, **2009**.

[88] C. D. Rahn, C. Y. Wang, *Battery Systems Engineering*, John Wiley And Sons, **2013**.

[89] and D. A. R. Dell, Ronald M., *"How a Batter. Oper. Underst. Batter.* **2001**, pp. 10.

[90] C. X. Zu, H. Li, *Energy Environ. Sci.* **2011**, *4*, 2614.

[91] C. Glaize, S. Geniès, *Lithium Batteries and Other Electrochemical Storage Systems*,

Wiley, **2013**.

[92] A. Ponrouch, D. Monti, A. Boschin, B. Steen, P. Johansson, M. R. Palacín, *J. Mater. Chem. A* **2015**, *3*, 22.

[93] P. Barpanda, G. Oyama, S. Nishimura, S.-C. Chung, A. Yamada, *Nat. Commun.* **2014**, *5*, 4358.

[94] G. Zhou, D.-W. Wang, F. Li, L. Zhang, N. Li, Z.-S. Wu, L. Wen, G. Q. (Max) Lu, H.-M. Cheng, *Chem. Mater.* **2010**, *22*, 5306.

[95] L. Lu, X. Han, J. Li, J. Hua, M. Ouyang, *J. Power Sources* **2013**, *226*, 272.

[96] L. Li, Y. Zheng, S. Zhang, J. Yang, Z. Shao, Z. Guo, *Energy Environ. Sci.* **2018**, *11*, 2310.

[97] Y. Li, Y.-S. S. Hu, M.-M. M. Titirici, L. Chen, X. Huang, *Adv. Energy Mater.* **2016**, *6*, 10.

[98] A. Metrot, D. Guerard, D. Billaud, A. Herold, *Synth. Met.* **1980**, *1*, 363.

[99] P. Ge, M. Fouletier, *Solid State Ionics* **1988**, *28–30*, 1172.

[100] N. Adhoum, J. Bouteillon, D. Dumas, J. C. Poignet, *Electrochim. Acta* **2006**, *51*, 5402.

[101] M. M. Doeff, Y. Ma, S. J. Visco, L. C. De Jonghe, *J. Electrochem. Soc.* **1993**, *140*, L169.

[102] Y. Li, Y. Lu, C. Zhao, Y. S. Hu, M. M. Titirici, H. Li, X. Huang, L. Chen, *Energy Storage Mater.* **2017**, *7*, 130.

[103] R. E. Franklin, *Proc. R. Soc. London. Ser. A. Math. Phys. Sci.* **1951**, *209*, 196.

[104] P. J. F. Harris, *J. Mater. Sci.* **2013**, *48*, 565.

[105] B. E. Warren, A. X.-R. Study, *Raman Spectr. Graph. J. Chem. Phys.* **1934**, *2*, 1503.

[106] I. Edwards, R. Menendez, H. Marsh, *Introduction to Carbon Science*, **2013**.

[107] Z. Li, C. Bommier, Z. Sen Chong, Z. Jian, T. W. Surta, X. Wang, Z. Xing, J. C. Neuefeind, W. F. Stickle, M. Dolgos, P. A. Greaney, X. Ji, *Adv. Energy Mater.* **2017**, *7*, 1.

[108] R. E. Franklin, *Acta Crystallogr.* **1950**.

[109] A. Ponrouch, A. Goñi, M. Palacín, *Electrochem. commun.* **2013**, *27*, 85.

[110] R. Zeng, W. Zhang, W. Yin, K.-L. Hong, L. Qie, Z.-Q. Yi, D. Wang, C. Wu, Q.-J. Fan, W.-X. Zhang, Y.-H. Huang, *J. Mater. Chem. A* **2014**, *2*, 12733.

[111] L. Wu, D. Buchholz, C. Vaalma, G. A. Giffin, S. Passerini, *ChemElectroChem* **2016**, *3*, 292.

[112] P. Liu, Y. Li, Y. Hu, H. Li, L. Chen, X. Huang, *J. Mater. Chem. A* **2016**, *4*, 13046.

[113] K. Wang, Y. Jin, S. Sun, Y. Huang, J. Peng, J. Luo, Q. Zhang, Y. Qiu, C. Fang, J. Han,

ACS Omega **2017**, *2*, 1687.

[114] W. Lv, F. Wen, J. Xiang, J. Zhao, L. Li, L. Wang, Z. Liu, Y. Tian, *Electrochim. Acta* **2015**, *176*, 533.

[115] B. Zhang, C. M. Ghimbeu, C. Laberty, C. Vix-Guterl, J.-M. M. Tarascon, *Adv. Energy Mater.* **2016**, *6*, 1501588.

[116] Y. Li, M. Paranthaman, K. Akato, A. Naskar, A. . Levine, R. . Lee, S.-O. Kim, J. Zhang, S. Dai, A. Manthiram, *J. Power Sources* **2016**, *316*, 232.

[117] A. Navarro-Suárez, D. Saurel, S.-F. P, E. Castillo-Martínez, J. Carretero-González, T. Rojo, *J. Power Sources* **2018**, *397*, 296.

[118] P. Thomas, D. Billaud, *Electrochim. Acta* **2001**, *46*, 3359.

[119] S. Komaba, W. Murata, T. Ishikawa, N. Yabuuchi, T. Ozeki, T. Nakayama, A. Ogata, K. Gotoh, K. Fujiwara, *Adv. Funct. Mater.* **2011**, *21*, 3859.

[120] Z. Li, L. Ma, T. W. Surta, C. Bommier, Z. Jian, Z. Xing, W. F. Stickle, M. Dolgos, K. Amine, J. Lu, T. Wu, X. Ji, *ACS Energy Lett.* **2016**, *1*, 395.

[121] W. Luo, J. Schardt, C. Bommier, B. Wang, J. Razink, J. Simonsen, X. Ji, *J. Mater. Chem. A* **2013**, *1*, 10662.

[122] C. Bommier, X. Ji, *Isr. J. Chem.* **2015**, *55*, 486.

[123] Z. Li, Z. Jian, X. Wang, I. A. Rodríguez-Pérez, C. Bommier, X. Ji, *Chem. Commun.* **2017**, 2610.

[124] W. Luo, C. Bommier, Z. Jian, X. Li, R. Carter, S. Vail, Y. Lu, J.-J. Lee, X. Ji, *ACS Appl. Mater. Interfaces* **2015**, *7*, 39.

[125] A. Ponrouch, M. R. Palacín, *Electrochem. commun.* **2015**, *54*, 51.

[126] H. Yamamoto, S. Muratsubaki, K. Kubota, M. Fukunishi, H. Watanabe, J. Kim, S. Komaba, *J. Mater. Chem. A* **2018**, *6*, 16844.

[127] L. Xiao, Y. Cao, W. A. Henderson, M. L. Sushko, Y. Shao, J. Xiao, W. Wang, M. H. Engelhard, Z. Nie, J. Liu, **2016**, *19*, 279.

[128] Z. Jian, C. Bommier, L. Luo, Z. Li, W. Wang, C. Wang, P. A. Greaney, X. Ji, *Chem. Mater.* **2017**, *29*, 2314.

[129] D. A. Stevens, J. R. Dahn, *J. Electrochem. Soc.* **2000**, *147*, 4428.

[130] S. Komaba, W. Murata, T. Ishikawa, N. Yabuuchi, T. Ozeki, T. Nakayama, A. Ogata, K. Gotoh, K. Fujiwara, *Adv. Funct. Mater.* **2011**, *21*, 3859.

[131] P. Bai, Y. He, X. Zou, X. Zhao, P. Xiong, Y. Xu, *Adv. Energy Mater.* **2018**, *8*, DOI 10.1002/aenm.201703217.

[132] Y. Cao, L. Xiao, M. L. Sushko, W. Wang, B. Schwenzer, J. Xiao, Z. Nie, L. V. Saraf, Z. Yang, J. Liu, *Nano Lett.* **2012**, *12*, 3783.

[133] C. Matei Ghimbeu, J. Górka, V. Simone, L. Simonin, S. Martinet, C. Vix-Guterl, *Nano Energy* **2018**, *44*, 327.

[134] Y. Morikawa, S. Nishimura, R. Hashimoto, M. Ohnuma, A. Yamada, *Adv. Energy Mater.* **2020**, *10*, 1903176.

[135] Q. Liu, Z. Hu, M. Chen, C. Zou, H. Jin, S. Wang, S. Chou, Y. Liu, S. Dou, *Adv. Funct. Mater.* **2020**, *30*, 1909530.

[136] C. Liu, Z. G. Neale, G. Cao, *Mater. Today* **2016**, *19*, 109.

[137] P.-F. Wang, Y. You, Y.-X. Yin, Y.-G. Guo, *Adv. Energy Mater.* **2018**, *8*, 1701912.

[138] J. Hwang, S. Myung, C. Yoon, SS Kim, *Wiley Online Libr.* **2016**, *26*, 8083.

[139] H. V. Ramasamy, K. Kaliyappan, R. Thangavel, V. Aravindan, K. Kang, D. U. Kim, Y. Park, X. Sun, Y. S. Lee, *J. Mater. Chem. A* **2017**, *5*, 8408.

[140] S. Kalluri, K. Hau Seng, W. Kong Pang, Z. Guo, Z. Chen, H. K. Liu, S. X. Dou, *ACS Appl. Mater. Interfaces* **2014**, *6*, 8953.

[141] A. Manthiram, J. B. Goodenough, *J. Solid State Chem.* **1987**, *71*, 349.

[142] C. Masquelier, L. Croguennec, *Chem. Rev.* **2013**, *113*, 6552.

[143] Y. Fang, X. Y. Yu, X. W. (David) Lou, *Matter* **2019**, *1*, 90.

[144] Y. Fang, L. Xiao, X. Ai, Y. Cao, H. Y. Yang J Fang, X. P. Ai, Y. L. Cao, H. X. Yang, L. F. Xiao, **2015**, DOI 10.1002/adma.201502018.

[145] J. Qian, C. Wu, Y. Cao, Z. Ma, Y. Huang, X. Ai, H. Yang, *Adv. Energy Mater.* **2018**, *8*, 1702619.

[146] Z. Lin, Q. Xia, W. Wang, W. Li, S. Chou, *InfoMat* **2019**, *1*, 376.

[147] E. Jónsson, P. Johansson, *Phys. Chem. Chem. Phys.* **2012**, *14*, 10774.

[148] L. Lutz, D. Alves Dalla Corte, M. Tang, E. Salager, M. Deschamps, A. Grimaud, L. Johnson, P. G. Bruce, J. M. Tarascon, *Chem. Mater.* **2017**, *29*, 6066.

[149] A. Bhide, J. Hofmann, A. K. Dü, J. Rgen Janek, P. Adelhelm, *Phys. Chem. Chem. Phys* **2014**, *16*, 1987.

[150] A. Ponrouch, E. Marchante, M. Courty, J. M. Tarascon, M. R. Palacín, *Energy Environ. Sci.* **2012**, *5*, 8572.

[151] M. K. Sadan, S. H. Choi, H. H. Kim, C. Kim, G. B. Cho, K. W. Kim, N. S. Reddy, J. H. Ahn, H. J. Ahn, *Ionics (Kiel).* **2018**, *24*, 753.

[152] L. Bodenes, A. Darwiche, L. Monconduit, H. Martinez, *J. Power Sources* **2015**, *273*, 14.

[153] D. Devlin, P. Herley, *React. Solids* **1987**, *3*, 75.

[154] C. Geng, D. Buchholz, G. Kim, D. V. Carvalho, H. Zhang, L. G. Chagas, S. Passerini, *Small Methods* **2019**, *3*, 1800208.

[155] Y. Zhu, X. Luo, H. Zhi, X. Yang, L. Xing, Y. Liao, M. Xu, W. Li, *ACS Appl. Mater. Interfaces* **2017**, *9*, 12021.

[156] J. Chen, Z. Huang, C. Wang, S. Porter, B. Wang, W. Lie, H. K. Liu, *Chem. Commun.* **2015**, *51*, 9809.

[157] A. Plewa-Marczewska, T. Trzeciak, A. Bitner, L. Niedzicki, M. Dranka, G. Z. Zukowska, M. Marcinek, W. Wieczorek, *Chem. Mater.* **2014**, *26*, 4908.

[158] S. Hong, Y. Kim, Y. Park, A. Choi, N. Choi, K. L.- Chem, *Energy Environ. Sci.* **2013**, *6*, 2067.

[159] V Gutmann, *Electrochim. Acta* **1976**, *21*, 661.

[160] K. Fukui, T. Yonezawa, H. Shingu, *J. Chem. Phys.* **1952**, *20*, 722.

[161] Z. Zhou, R. G. Parr, *J. Am. Chem. Soc.* **1990**, *112*, 5720.

[162] R. G. Pearson, *J. Org. Chem.* **1989**, *54*, 1423.

[163] L. Xing, X. Zheng, M. Schroeder, J. Alvarado, A. Von Wald Cresce, K. Xu, Q. Li, W. Li, *Acc. Chem. Res.* **2018**, *51*, 282.

[164] K. Xu, *Chem. Rev.* **2004**, *104*, 4303.

[165] A. Ponrouch, R. Dedryvère, D. Monti, A. E. Demet, J. M. Ateba Mba, L. Croguennec, C. Masquelier, P. Johansson, M. R. Palacín, *Energy Environ. Sci.* **2013**, *6*, 2361.

[166] G. G. Eshetu, G. A. Elia, M. Armand, M. Forsyth, S. Komaba, T. Rojo, S. Passerini, *Adv. Energy Mater.* **2020**, *10*, 2000093.

[167] B. Jache, J. O. Binder, T. Abe, P. Adelhelm, *Phys. Chem. Chem. Phys.* **2016**, *18*, 14299.

[168] J. Zhang, D. W. Wang, W. Lv, S. Zhang, Q. Liang, D. Zheng, F. Kang, Q. H. Yang, *Energy Environ. Sci.* **2017**, *10*, 370.

[169] V. A. Agubra, J. W. Fergus, *J. Power Sources* **2014**, *268*, 153.

[170] J. B. Goodenough, Y. Kim, *Chem. Mater.* **2010**, *22*, 587.

[171] G. Nazri, G. Pistoia, *Lithium Batteries: Science and Technology*, **2008**.

[172] E. Peled, H. Yamin, *Isr. J. Chem.* **1979**, *18*, 131.

[173] V. Etacheri, R. Marom, R. Elazari, G. Salitra, D. Aurbach, *Energy Environ. Sci.* **2011**, *4*, 3243.

[174] L. Shen, S. Shi, S. Roy, X. Yin, W. Liu, Y. Zhao, *Adv. Funct. Mater.* **2021**, *31*, 2006066.

[175] S. Wenzel, T. Hara, J. Janek, P. Adelhelm, *Energy Environ. Sci.* **2011**, *4*, 3342.

[176] H. Zhang, X. Xuan, J. Wang, H. Wang, *Solid State Ionics* **2003**, *164*, 73.

[177] P. Bai, Y. He, P. Xiong, X. Zhao, K. Xu, Y. Xu, *Energy Storage Mater.* **2018**, *13*, 274.

[178] A. Darwiche, C. Marino, M. T. Sougrati, B. Fraisse, L. Stievano, L. Monconduit, *J. Am. Chem. Soc.* **2012**, *134*, 20805.

[179] R. Dugas, A. Ponrouch, G. Gachot, R. David, M. R. Palacin, J. M. Tarascon, *J. Electrochem. Soc.* **2016**, *163*, 2333.

[180] G. Yan, D. Alves-Dalla-Corte, … W. Y.-J. of the, undefined 2018, *iopscience.iop.org* **2018**, *165*, A1222.

[181] M.-M. M. Titirici, *Sustainable Carbon Materials from Hydrothermal Processes*, John Wiley & Sons, Ltd, Oxford, UK, **2013**.

[182] R. J. White, Ed. , *Porous Carbon Materials from Sustainable Precursors*, Royal Society Of Chemistry, Cambridge, **2015**.

[183] A. Marinovic, F. Pileidis, M. Titirici, *Hydrothermal Carbonisation (HTC): History, State-of-the-Art and Chemistry*, **2015**.

[184] M.-M. Titirici, R. J. White, C. Falco, M. Sevilla, *Energy Environ. Sci.* **2012**, *5*, 6796.

[185] M. M.-M. Titirici, M. Antonietti, *Chem. Soc. Rev.* **2010**, *39*, 103.

[186] V. G. Pol, E. Lee, D. Zhou, F. Dogan, J. M. Calderon-Moreno, C. S. Johnson, *Electrochim. Acta* **2014**, *127*, 61.

[187] H. L. Wang, Z. Q. Shi, J. Jin, C. Bin Chong, C. Y. Wang, *J. Electroanal. Chem.* **2015**, *755*, 87.

[188] J. Cui, Z.-L. Xu, S. Yao, J. Huang, J.-Q. Huang, S. Abouali, M. A. Garakani, X. Ning, J.-K. Kim, *J. Mater. Chem. A* **2016**, *4*, 10964.

[189] T. Liu, X. Li, *Mater. Technol.* **2019**, *34*, 232.

[190] P. Zheng, T. Liu, J. Zhang, L. Zhang, Y. Liu, J. Huang, S. Guo, *RSC Adv.* **2015**, *5*, 40737.

[191] P. Zheng, T. Liu, X. Yuan, L. Zhang, Y. Liu, J. Huang, S. Guo, *Sci. Rep.* **2016**, *6*, 1.

[192] B. Hu, K. Wang, L. Wu, S. Yu, M. Antonietti, TI, *Adv. Mater.* **2010**.

[193] F. Xie, Z. Xu, A. C. S. Jensen, F. Ding, H. Au, J. Feng, H. Luo, M. Qiao, Z. Guo, Y. Lu, A. J. Drew, Y. S. Hu, M. M. Titirici, *J. Mater. Chem. A* **2019**, *7*, 27567.

[194] "An Introduction to Electron Microscopy - The Scanning Electron Microscope," can be found under https://www.fei.com/introduction-to-electron-microscopy/sem/, **2018**.

[195] J. I. Goldstein, D. E. Newbury, P. Echlin, D. C. Joy, A. D. Romig, C. E. Lyman, C. Fiori, E. Lifshin, *Scanning Electron Microscopy and X-Ray Microanalysis : A Text for*

Biologists, Materials Scientists, and Geologists, Springer US, **1992**.

[196] B. J. Ford, S. Bradbury, D. . Joy, "Transmission electron microscope," can be found under https://www.britannica.com/technology/transmission-electron-microscope, **2019**.

[197] C. Bommier, D. Mitlin, X. Ji, *Prog. Mater. Sci.* **2018**, *97*, 170.

[198] E. Irisarri, A. Ponrouch, M. R. Palacin, *J. Electrochem. Soc.* **2015**, *162*, A2476.

[199] A. C. Ferrari, J. Robertson, *Phys. Rev. B* **2000**, *61*, 14095.

[200] A. C. Ferrari, D. M. Basko, *Nat. Nanotechnol.* **2013**, *8*, 235.

[201] M. R. Ammar, J.-N. Rouzaud, *J. Raman Spectrosc.* **2012**, *43*, 207.

[202] A. C. Ferrari, *Solid State Commun.* **2007**, *143*, 47.

[203] L. Wu, D. Bresser, D. Buchholz, G. A. Giffin, C. R. Castro, A. Ochel, S. Passerini, *Adv. Energy Mater.* **2015**, *5*, DOI 10.1002/aenm.201401142.

[204] Z. Zhu, F. Cheng, Z. Hu, Z. Niu, J. Chen, *J. Power Sources* **2015**, *293*, 626.

[205] F. A. Stevie, R. Garcia, J. Shallenberger, J. G. Newman, C. L. Donley, *J. Vac. Sci. Technol. A* **2020**, *38*, 063202.

[206] K. A. Cychosz, R. Guillet-Nicolas, J. García-Martínez, M. Thommes, *Chem. Soc. Rev.* **2017**, *46*, 389.

[207] M. Thommes, K. Kaneko, A. V. Neimark, J. P. Olivier, F. Rodriguez-Reinoso, J. Rouquerol, K. S. W. Sing, *Pure Appl. Chem.* **2015**, *87*, 1051.

[208] A. W. Adamson, A. P. Gast, J. Wiley, *Physical Chemistry of Surfaces Sixth Edition*, **1997**.

[209] V. Simone, A. Boulineau, A. de Geyer, D. Rouchon, L. Simonin, S. Martinet, *J. Energy Chem.* **2016**, *25*, 761.

[210] M. Dahbi, M. Kiso, K. Kubota, T. Horiba, T. Chafik, K. Hida, T. Matsuyama, S. Komaba, *J. Mater. Chem. A* **2017**, *5*, 9917.

[211] A. J. Smith, M. J. MacDonald, L. D. Ellis, M. N. Obrovac, J. R. Dahn, *Carbon N. Y.* **2012**, *50*, 3717.

[212] Crouch-Baker S., Deublein G., Tsai H. C., Zhou, L. Z., R. A. Huggins, *Solid State Ionics* **1990**, *42*, 109.

[213] J. Li, A. Jiao, S. Chen, Z. Wu, E. Xu, Z. Jin, *J. Mol. Struct.* **2018**, *1165*, 391.

[214] A. Gibaud, J. S. Xue, J. R. Dahn, *Carbon N. Y.* **1996**, *34*, 499.

[215] M. Schroeder, S. Menne, J. Ségalini, D. Saurel, M. Casas-Cabanas, S. Passerini, M. Winter, A. Balducci, *J. Power Sources* **2014**, *266*, 250.

[216] C. Prehal, D. Weingarth, E. Perre, R. T. Lechner, H. Amenitsch, O. Paris, V. Presser,

Energy Environ. Sci. **2015**, *8*, 1725.

[217] K. Nishikawa, in *Carbon Alloy. Nov. Concepts to Dev. Carbon Sci. Technol.*, Elsevier Ltd., **2003**, pp. 175–188.

[218] P. I. Ravikovitch, A. Vishnyakov, R. Russo, A. V. Neimark, *Langmuir* **2000**, *16*, 2311.

[219] Q. Meng, Y. Lu, F. Ding, Q. Zhang, L. Chen, Y. S. Hu, *ACS Energy Lett.* **2019**, *4*, 2608.

[220] F. Xie, Z. Xu, A. C. S. Jensen, H. Au, Y. Lu, V. Araullo-Peters, A. J. Drew, Y. Hu, M. Titirici, *Adv. Funct. Mater.* **2019**, *1901072*, 1901072.

[221] A. Claye, J. E. Fischer, *Electrochim. Acta* **1999**, *45*, 107.

[222] M. Winter, G. H. Wrodnigg, J. O. Besenhard, W. Biberacher, P. Novák, *J. Electrochem. Soc.* **2000**, *147*, 2427.

[223] M. Goktas, C. Bolli, E. J. Berg, P. Novák, K. Pollok, F. Langenhorst, M. v. Roeder, O. Lenchuk, D. Mollenhauer, P. Adelhelm, *Adv. Energy Mater.* **2018**, *8*, 1702724.

[224] P. Verma, P. Maire, P. Novák, *Electrochim. Acta* **2010**, *55*, 6332.

[225] M. M. Titirici, H. Alptekin, H. Au, A. C. S. Jensen, E. Olsson, M. Goktas, T. F. Headen, P. Adelhelm, Q. Cai, A. J. Drew, *ACS Appl. Energy Mater.* **2020**, *3*, 9918.

[226] L. Y. Beaulieu, K. W. Eberman, R. L. Turner, L. J. Krause, J. R. Dahn, *Electrochem. Solid-State Lett.* **2001**, *4*, A137.

[227] L. Y. Beaulieu, T. D. Hatchard, A. Bonakdarpour, M. D. Fleischauer, J. R. Dahn, *J. Electrochem. Soc.* **2003**, *150*, A1457.

[228] L. Y. Beaulieu, V. K. Cumyn, K. W. Eberman, L. J. Krause, J. R. Dahn, *Rev. Sci. Instrum.* **2001**, *72*, 3313.

[229] R. Weber, C. R. Fell, J. R. Dahn, S. Hy, *J. Electrochem. Soc.* **2017**, *164*, A2992.

[230] *ECD-3 Content. Https://El-Cell.Com/Products/Test-Cells/Electrochemical-Dilatometer/Ecd-3*, **2017**.

[231] J. Wang, *Analytical Electrochemistry*, John Wiley & Sons, Inc., Hoboken, NJ, USA, **2006**.

[232] D. Brownson, C. Banks, **2014**.

[233] Y. Cai, X. Cao, Z. Luo, G. Fang, F. Liu, J. Zhou, A. Pan, S. Liang, *Adv. Sci.* **2018**, *5*, 1800680.

[234] Dove Martin, *STFC ISIS Neutron Muon Source* **2018**, DOI 10.5286/ISIS.E.RB1810728.

[235] A. K. Soper, **2011**.

[236] D. A. Keen, *J. Appl. Crystallogr.* **2001**, *34*, 172.

[237] G. Kresse, J. Furthmüller, *Comput. Mater. Sci.* **1996**, *6*, 15.

[238] G. Kresse, J. Furthmüller, *Phys. Rev. B. Condens. Matter* **1996**, *54*, 11169.

[239] G. Kresse, J. Hafner, *Phys. Rev. B* **1994**, *49*, 14251.

[240] G. Kresse, J. Hafner, *Phys. Rev. B* **1993**, *47*, 558.

[241] E. Olsson, G. Chai, M. Dove, Q. Cai, *Nanoscale* **2019**, *11*, 5274.

[242] P. E. Blöchl, *Phys. Rev. B* **1994**, *50*, 17953.

[243] H. J. Monkhorst, J. D. Pack, *Phys. Rev. B* **1976**, *13*, 5188.

[244] J. Perdew, K. Burke, M. Ernzerhof, *Phys. Rev. Lett.* **1997**, *77*, 1396.

[245] J. Perdew, K. Burke, M. Ernzerhof, *Phys. Rev. Lett.* **1996**, *77*, 3865.

[246] X. Fan, W. T. Zheng, J.-L. L. Kuo, D. J. Singh, *ACS Appl. Mater. Interfaces* **2013**, *5*, 7793.

[247] M. Amft, S. Lebègue, O. Eriksson, N. V. Skorodumova, *J. Phys. Condens. Matter* **2011**, *23*, 395001.

[248] A. D. Becke, E. R. Johnson, *J. Chem. Phys.* **2005**, *123*, 154108.

[249] S. Grimme, S. Ehrlich, L. Goerigk, *J. Comput. Chem.* **2011**, *32*, 1456.

[250] S. Qiu, L. Xiao, M. L. Sushko, K. S. Han, Y. Shao, M. Yan, X. Liang, L. Mai, J. Feng, Y. Cao, X. Ai, H. Yang, J. Liu, *Adv. Energy Mater.* **2017**, *7*, 1700403.

[251] M. Dahbi, N. Yabuuchi, K. Kubota, K. Tokiwa, S. Komaba, *Phys. Chem. Chem. Phys.* **2014**, *16*, 15007.

[252] A. C. Ferrari, John Robertson, *Philos. Trans. R. Soc. London* **2004**, *362.1824*, 2477.

[253] A. C. Ferrari, J. C. Meyer, V. Scardaci, C. Casiraghi, M. Lazzeri, F. Mauri, S. Piscanec, D. Jiang, K. S. Novoselov, S. Roth, A. K. Geim, *Phys. Rev. Lett.* **2006**, *97.18*, 187401.

[254] M.-M. Titirici, M. Antonietti, N. Baccile, *Green Chem.* **2008**, *10*, 1204.

[255] V. Augustyn, P. Simon, B. Dunn, *Energy Environ. Sci.* **2014**, *7*, 1597.

[256] J. Wang, J. Polleux, J. Lim, B. Dunn, *J. Phys. Chem. C* **2007**, *111*, 14925.

[257] C. Bommier, T. W. Surta, M. Dolgos, X. Ji, *Nano Lett.* **2015**, *15*, 5888.

[258] J. L. Gómez-Cámer, C. Bünzli, M. M. Hantel, T. Poux, P. Novák, *Carbon N. Y.* **2016**, *105*, 42.

[259] T. Palaniselvam, M. Goktas, B. Anothumakkool, Y. Sun, R. Schmuch, L. Zhao, B. Han, M. Winter, P. Adelhelm, *Adv. Funct. Mater.* **2019**, *29*, 1900790.

[260] H. Au, N. Rubio Carrero, D. J. Buckley, C. Mattevi, M. Shaffer, *Chem. – A Eur. J.* **2020**, *26.29*, 6545.

[261] P. Tsai, S.-C. Chung, S. Lin, A. Yamada, *J. Mater. Chem. A* **2015**, *3*, 9763.

[262] K. Nakada, A. Ishii, *Solid State Commun.* **2011**, *151*, 13.

[263] K. Momma, F. Izumi, *J. Appl. Crystallogr.* **2011**, 1272.

[264] H. Raebiger, S. Lany, A. Zunger, *Phys. Rev. B* **2007**, *76*, 045209.

[265] S. Zhang, J. Northrup, *Phys. Rev. Lett.* **1991**, *67*, 2339.

[266] J. Wang, C. Xue, Y. Lv, F. Zhang, B. Tu, D. Zhao, *Carbon N. Y.* **2011**, *49*, 4580.

[267] C. Liang, K. Hong, G. A. Guiochon, J. W. Mays, S. Dai, *Angew. Chemie - Int. Ed.* **2004**, *43*, 5785.

[268] Y. Meng, D. Gu, F. Zhang, Y. Shi, H. Yang, Z. Li, C. Yu, B. Tu, D. Zhao, *Angew. Chemie - Int. Ed.* **2005**, *44*, 7053.

[269] S. Tanaka, N. Nishiyama, Y. Egashira, K. Ueyama, *Chem. Commun.* **2005**, *0*, 2125.

[270] Y. Huang, H. Cai, D. Feng, D. Gu, Y. Deng, B. Tu, H. Wang, P. A. Webley, D. Zhao, *Chem. Commun.* **2008**, *0*, 2641.

[271] Y. Fang, D. Gu, Y. Zou, Z. Wu, F. Li, R. Che, Y. Deng, B. Tu, D. Zhao, *Angew. Chemie* **2010**, *122*, 8159.

[272] Y. Meng, D. Gu, F. Zhang, Y. Shi, L. Cheng, D. Feng, Z. Wu, Z. Chen, Y. Wan, A. Stein, D. Zhao, **2006**, DOI 10.1021/cm060921u.

[273] B. Hammouda, *J. Appl. Crystallogr.* **2010**, *43*, 716.

[274] Q. Meng, Y. Lu, F. Ding, Q. Zhang, L. Chen, Y. S. Hu, *ACS Energy Lett.* **2019**, *4*, 2608.

[275] R. Mogensen, D. Brandell, R. Younesi, *ACS Publ.* **2016**, *1*, 1173.

[276] E. Paled, **1979**, *126*, 2047.

[277] V. Etacheri, R. Marom, R. Elazari, G. Salitra, D. Aurbach, *Energy Environ. Sci.* **2011**, *4*, 3243.

[278] X. Zheng, C. Bommier, W. Luo, L. Jiang, Y. Hao, Y. Huang, *Energy Storage Mater.* **2019**, *16*, 6.

[279] G. Bieker, M. Winter, P. Bieker, *Phys. Chem. Chem. Phys.* **2015**, *17*, 8670.

[280] Y. Xu, Q. Wei, C. Xu, Q. Li, Q. An, P. Zhang, J. Sheng, L. Zhou, L. Mai, *Adv. Energy Mater.* **2016**, *6*, 1600389.

[281] R. A. Shakoor, D. H. Seo, H. Kim, Y. U. Park, J. Kim, S. W. Kim, H. Gwon, S. Lee, K. Kang, *J. Mater. Chem.* **2012**, *22*, 20535.

[282] W. Song, X. Cao, Z. Wu, J. Chen, Y. Zhu, H. Hou, Q. Lan, X. Ji, *Langmuir* **2014**, *30*, 12438.

[283] Q. Liu, X. Meng, Z. Wei, D. Wang, Y. Gao, Y. Wei, F. Du, G. Chen, *ACS Appl. Mater. Interfaces* **2016**, *8*, 31709.

[284] C. Zhu, C. Wu, C. C. Chen, P. Kopold, P. A. Van Aken, J. Maier, Y. Yu, *Chem. Mater.*

2017, *29*, 5207.

[285] P. R. Kumar, Y. H. Jung, D. K. Kim, *J. Solid State Electrochem.* **2017**, *21*, 223.

[286] H. Che, S. Chen, Y. Xie, H. Wang, K. Amine, X. Z. Liao, Z. F. Ma, *Energy Environ. Sci.* **2017**, *10*, 1075.

[287] S. Tobishima, H. Morimoto, M. Aoki, Y. Saito, T. Inose, T. Fukumoto, T. Kuryu, *Electrochim. Acta* **2004**, *49*, 979.

[288] L. Zhou, Z. Cao, W. Wahyudi, J. Zhang, J.-Y. Hwang, Y. Cheng, L. Wang, L. Cavallo, T. Anthopoulos, Y.-K. Sun, H. N. Alshareef, J. Ming, *ACS Energy Lett.* **2020**, *5*, 766.

[289] V. Gutmann, *Donor-Acceptor Approach to Molecular Interactions*, Plenum Press, **1978**.

[290] E. R. Logan, E. M. Tonita, K. L. Gering, J. Li, X. Ma, L. Y. Beaulieu, J. R. Dahn, *J. Electrochem. Soc.* **2018**, *165*, A21.

[291] Y. Yamada, M. Yaegashi, T. Abe, A. Yamada, *Chem. Commun.* **2013**, *49*, 11194.

[292] D. Battisti, G. A. Nazri, B. Klassen, R. Aroca, *Vibrational Studies of Lithium Perchlorate in Propylene Carbonate Solutions*, **1993**.

[293] C. Geng, D. Buchholz, G. T. Kim, D. V. Carvalho, H. Zhang, L. G. Chagas, S. Passerini, *Small Methods* **2019**, *3*, 1.

[294] B. Klassen, R. Aroca, M. Nazri, G. A. Nazri, *J. Phys. Chem* **1998**, *102*, 4795.

[295] M. Kakihana, S. Schantz, L. M. Torell, *J. Chem. Phys.* **1990**, *92*, 6271.

[296] Sandner B., Tubke J., Werther A., Sandner R., Wartewig S., Shashkov S., *Electrochim. Acta,* **1998**, *43*, 1563.

[297] M. He, K. C. Lau, X. Ren, N. Xiao, W. D. McCulloch, L. A. Curtiss, Y. Wu, *Angew. Chemie - Int. Ed.* **2016**, *55*, 15310.

[298] D. James, R. Mayes, *Aust. J. Chem.* **1982**, *35*, 1775.

[299] T. Hosaka, T. Matsuyama, K. Kubota, R. Tatara, S. Komaba, *J. Mater. Chem. A* **2020**, *8*, 23766.

[300] D. Aurbach, B. Markovsky, I. Weissman, E. Levi, Y. Ein-Eli, *Electrochim. Acta* **1999**, *45*, 67.

[301] J. Vetter, P. Novák, M. R. Wagner, C. Veit, K. C. Möller, J. O. Besenhard, M. Winter, M. Wohlfahrt-Mehrens, C. Vogler, A. Hammouche, *J. Power Sources* **2005**, *147*, 269.

[302] G. P. López, D. G. Castner, B. D. Ratner, *Surf. Interface Anal.* **1991**, *17*, 267.

[303] R. Dedryvère, S. Laruelle, S. Grugeon, L. Gireaud, J.-M. Tarascon, D. Gonbeau, *J. Electrochem. Soc.* **2005**, *152*, A689.

[304] M. Dahbi, T. Nakano, N. Yabuuchi, T. Ishikawa, K. Kubota, M. Fukunishi, S. Shibahara,

J. Y. Son, Y. T. Cui, H. Oji, S. Komaba, *Electrochem. commun.* **2014**, *44*, 66.

[305] Y. C. Lin, Y. Y. Chen, B. Y. Yu, W. C. Lin, C. H. Kuo, J. J. Shyue, *Analyst* **2009**, *134*, 945.

[306] S. Choudhury, S. Wei, Y. Ozhabes, D. Gunceler, M. J. Zachman, Z. Tu, J. H. Shin, P. Nath, A. Agrawal, L. F. Kourkoutis, T. A. Arias, L. A. Archer, *Nat. Commun.* **2017**, *8*, 898.

[307] X. Fan, X. Ji, F. Han, J. Yue, J. Chen, L. Chen, T. Deng, J. Jiang, C. Wang, *Sci. Adv.* **2018**, *4*, 9245.

[308] M. He, R. Guo, G. M. Hobold, H. Gao, B. M. Gallant, *Proc. Natl. Acad. Sci.* **2020**, *117*, 73.

[309] K. Li, J. Zhang, D. Lin, D. W. Wang, B. Li, W. Lv, S. Sun, Y. B. He, F. Kang, Q. H. Yang, L. Zhou, T. Y. Zhang, *Nat. Commun.* **2019**, *10*, 1.

[310] Z. Xu, X. Lv, J. Chen, L. Jiang, Y. Lai, J. Li, *Carbon N. Y.* **2016**, *107*, 885.

[311] S. Yang, S. Li, S. Tang, W. Dong, W. Sun, D. Shen, M. Wang, *Theor. Chem. Acc.* **2016**, *135*, 1.

[312] L. H. Yao, W. Q. Cao, M. S. Cao, *Curr. Appl. Phys.* **2016**, *16*, 574.

[313] F. Oba, M. Choi, A. Togo, I. Tanaka, *Sci. Technol. Adv. Mater.* **2011**, *12*, 034302.

APPENDIX I

Supplementary figures for Chapter 4.

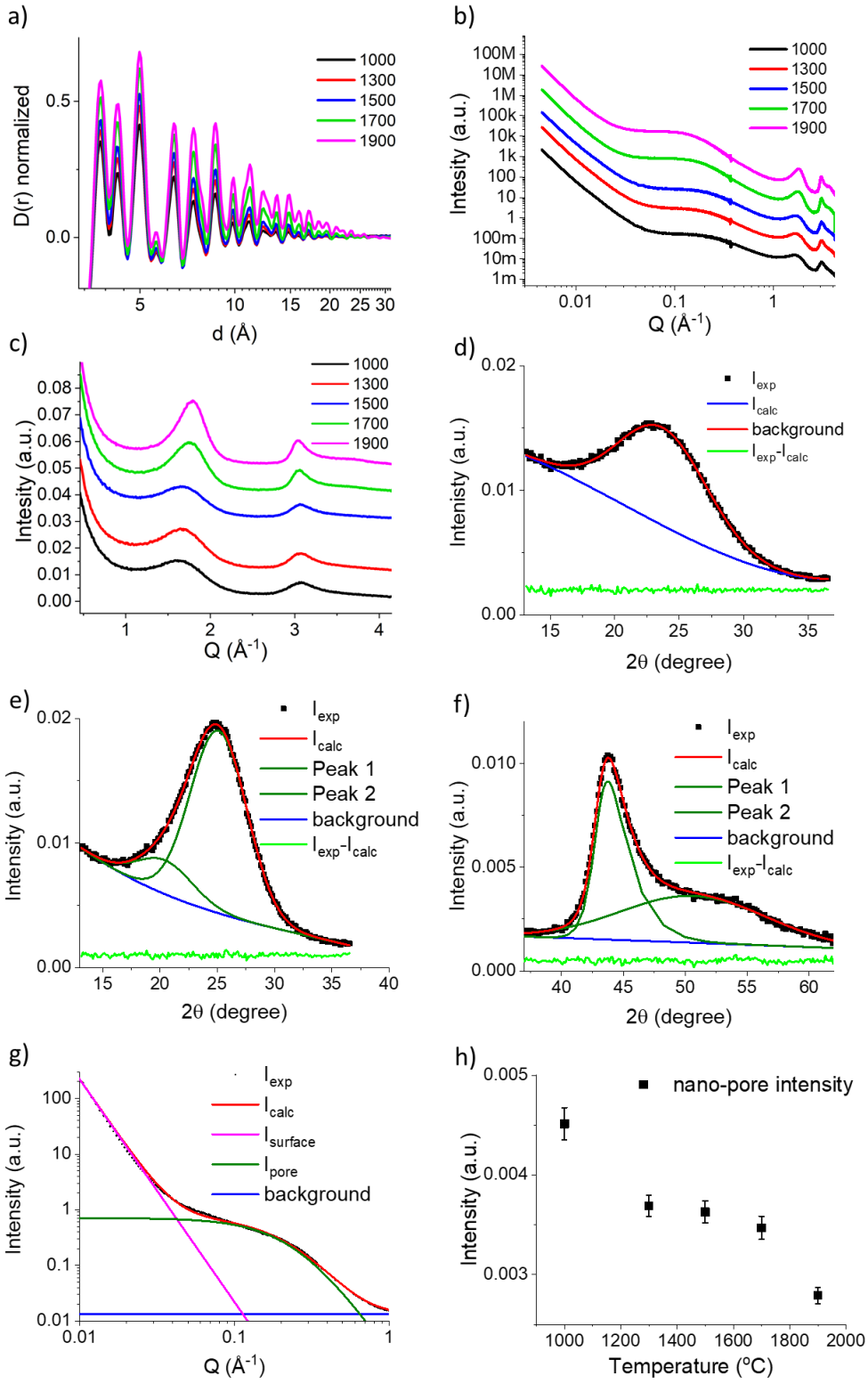


Figure 1. 1 a) Comparison of the PDF for the different hard carbon samples b) SAXS and c) WAXS patterns for the samples with an offset for clarity d) Example of data fits of the 002 peak for the low and e) high temperature samples f) the 100 peak and g) the Guinier-Porod[129] region of the SAXS data h) Intensity of the nanopore feature, proportional to the surface area of the internal pores[129]

$$breathing\ percentage = \frac{increase\ in\ electrode\ thickness\ after\ first\ cycle}{initial\ electrode\ thickness} \times 100 \qquad \text{(equation 1)}$$

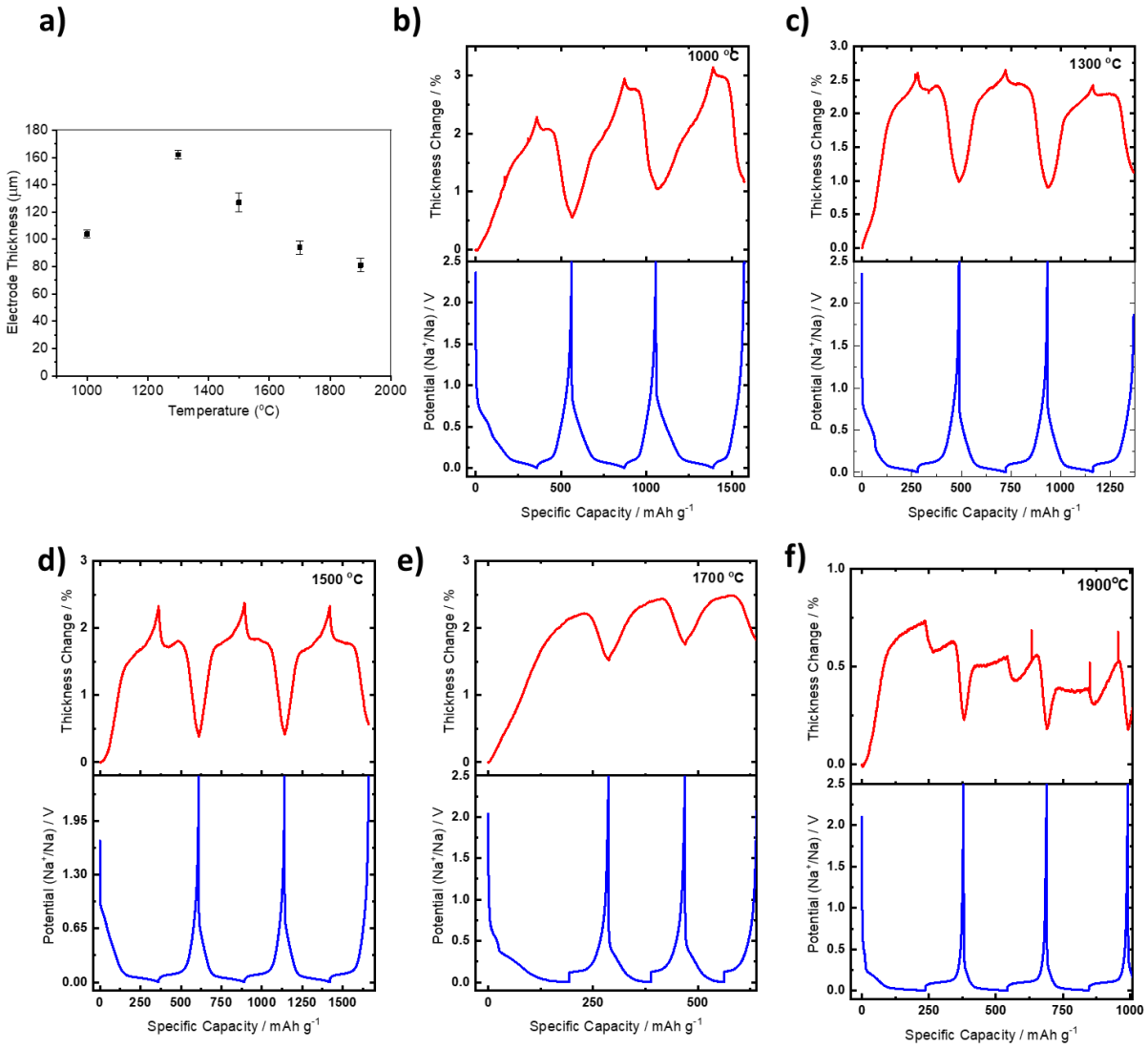


Figure 1. 2 a) Error margins of electrode thickness, In-situ electrochemical dilatometry measurements of the electrode thickness change in the first three cycles for b) GC1000 c) GC1300 d)GC1500 e) GC1700 and f) GC1900

The sodium adsorption or binding energy (E_{ads}^{Na}) was calculated according to eq. 2.[261,262,310,311]

$$E_{ads}^{Na} = E_{Na-C} - \mu_{Na} - E_C \qquad \text{(equation 2)}$$

Here, $E_{Na\text{-}C}$ is the total energy of the system with Na adsorbed on the carbon surfaces, E_C is the total energy of the graphene surface, and μ_{Na} is the chemical potential of an isolated sodium ion in vacuum (vacuum reference state).[262,312]

Table 1. 1 Calculated sodium binding energy (E_{bind}) for one Na in planar graphitic layers with d002 according to Table 1.

	d_{002} (Å)	E_{bind} (eV)
GC1000	3.75	-0.86
GC1300	3.68	-0.69
GC1500	3.66	-0.64
GC1700	3.58	-0.42
GC1900	3.43	0.13

The defects assessed here were constructed based on oxygen substitutional defects (O_C) and carbon vacancies (V_C). E_f^{defect} is commonly used as a measurement of defect concentration at equilibrium conditions (the lower the energy the higher the concentration) and is calculated from equation S2.[264,265,313]

$$E_f^{defect}(j) = E_{defective} + \sum n_j \mu_j - E_{graphene} \quad \text{(equation 3)}$$

$E_{defective}$ is the total energy of the defective graphene sheet, $E_{graphene}$ is the total energy of the graphene sheet, n_j is the number of oxygen or carbon atoms added or removed in relation to pristine graphite, and μ_j is the chemical potential of O, and C, respectively, μ_C is calculated as

the total energy per carbon atom in pristine graphene, whereas μ_O is calculated from its gas phase. The calculated defect and adsorption energies are presented in Table 1.2.

Table 1. 2 Calculated defect formation energies (E_f^{defect}) [264,265]for the defects shown in, together with the sodium adsorption energy (E_{ads}^{Na}) on the different defects. All values are in units of eV. For reference, E_{ads}^{Na} for sodium on pristine graphene is -0.62 eV.[241]

Defect	O_C	O_CV_C	$2O_CV_C$	$3O_C$ [241]	$2O_C$ [241]
E_f^{defect}	2.13	4.83	1.40	8.22	0.12
E_{ads}^{Na}	-0.62	-2.85	-0.70	-1.35	-0.67

APPENDIX II

Supplementary Figures for Chapter 5 & 6.

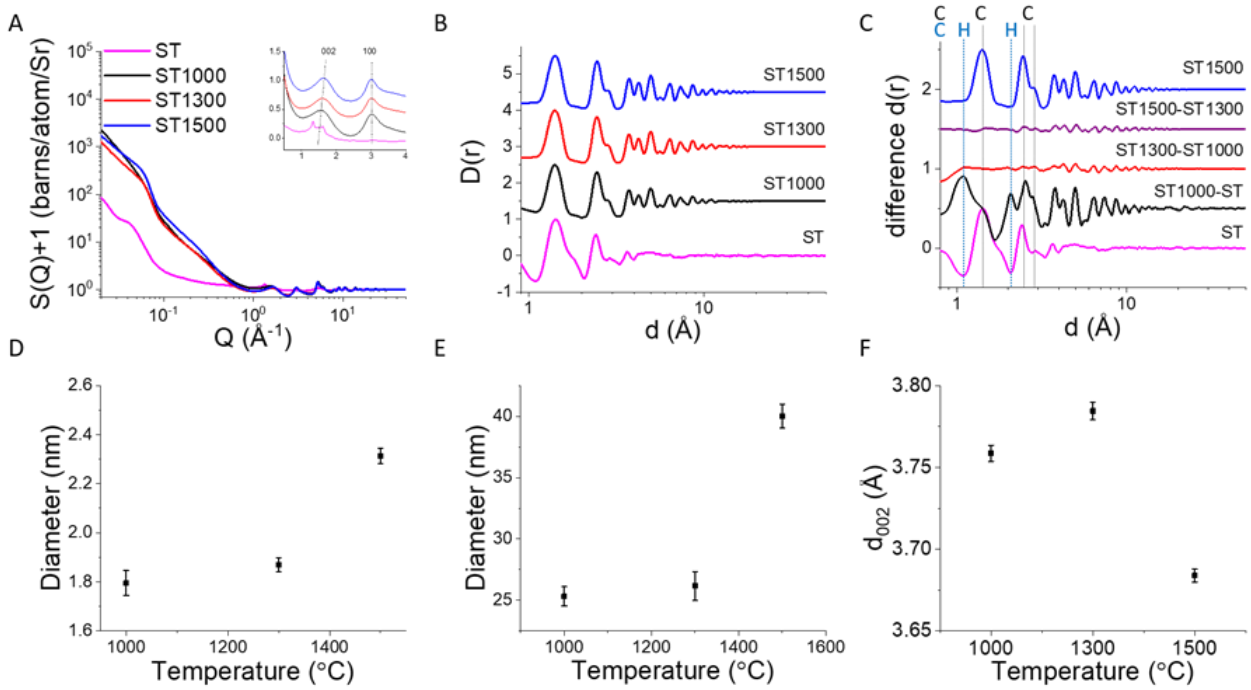


Figure 2. 1 Neutron structure factor, b) PDF and c) difference PDF of the different samples and the precursor prior to high temperature treatment(denoted ST). Insert in A shows the 002 and 100 peaks related to the local graphitic domains. The letters above the difference PDF indicates the atomic pairs for key correlation peaks, due to the negative scattering length of hydrogen the C-H correlation peaks are negative. d) Pore size diameter of the nanopores native to hard carbon. e) Diameter of nanopores formed from the templating polymer. f) Average spacing between the graphitic basal planes determined from the 002 peak.

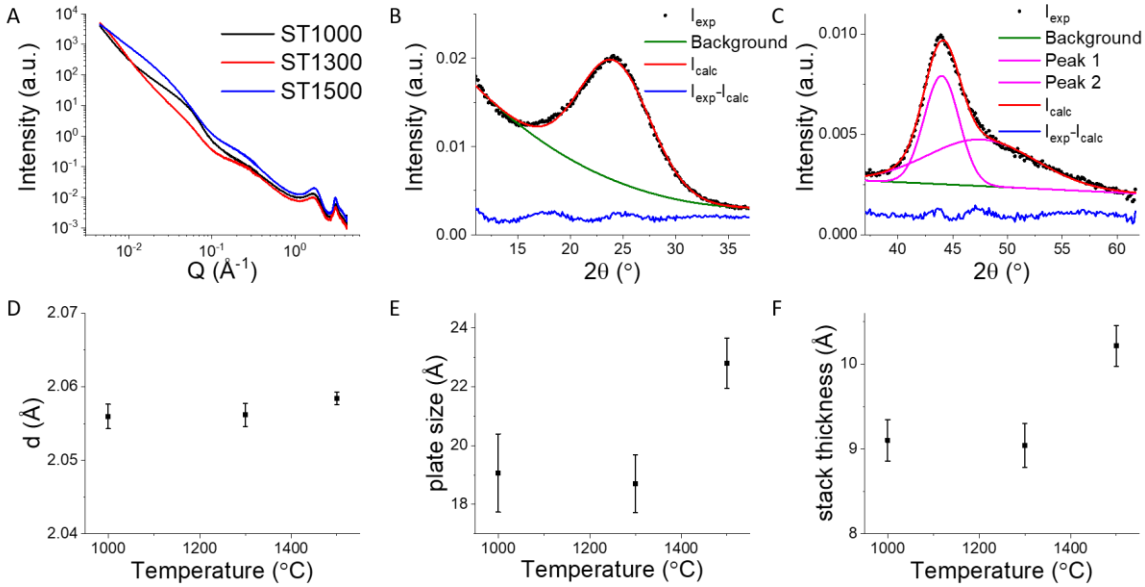


Figure 2. 2 a) SAXS/WAXS patterns. Measured and calculated profiles of the b) 002 and c)100 peaks and d) calculated d_{100} spacing e) Basal plane size f) and thickness of basal plane stacks(F).